

Unsteady Numerical Simulation of the Pressure Distribution in a Ball-on-Disc Tribometer

Instationäre numerische Simulation der Druckverteilung in einem
Kugel-Scheibe Tribometer

Bachelor Thesis - Numerical

Altay Kacan

At the Department of Mechanical Engineering,
Institute of Fluid Mechanics

Advisors: Prof. Dr.-Ing. Bettina Frohnappel
M.Sc. Erik Hansen

Duration: November 2020 – February 2021

I declare that I have developed and written the enclosed thesis completely by myself, and have not used sources or means without declaration in the text.

Karlsruhe, 22. 02. 2021

.....
(Altay Kacan)

Abstract

Lubrication of surfaces in relative motion is essential to avoid unnecessary energy losses due to friction. Surface texturing is a promising way of achieving desirable properties of lubricated contacts such as decreased friction and increased load carrying capacity. The lack of general statements and contradictory findings are the main challenges for widespread use of surface texturing. Ball-on-disc tribometers are used to predict properties of real contacts in a laboratory setting. This thesis builds upon the work of Erik Hansen that simulates such a tribometer in steady conditions to extend it to include transient effects and a micro-texture on the ball surface. The aim of this work is to validate the numerical predictions by comparing them to experimental results. The used equations are derived and explained. The numerical approaches and the working principles of the utilized algorithms are detailed. A good agreement between the simulation results and the experimental data from the literature is found. The overall behaviour of the new solver is also investigated. Simulations with varying spatial grid sizes with proportionally scaled time steps and constant grid sizes with changing time step magnitudes are carried out and analysed. It is found that coarser grids correspond to large deviations from experimental results but the finest grids investigated were associated with long computation times, so a compromise must be made depending on the requirements.

Kurzfassung

Die Schmierung von Oberflächen, welche sich in Relativbewegung befinden, ist sehr wichtig, um unnötige Energieverluste wegen Reibung zu vermeiden. Das gezielte Einbringen von Oberflächentexturen ist die Verringerung des Reibungsverlusts und die Erhöhung der Belastungskapazität. Der Mangel an allgemeingültigen Aussagen und widersprüchlichen Erkenntnissen aus der Literatur sind die Hauptherausforderungen für eine weitverbreitete Nutzung von Oberflächentexturen. Kugel-Scheibe Tribometer werden benutzt, um die Eigenschaften von realen Reibkontakten in einem Labor zu voraussagen. Diese Bachelorarbeit baut auf der Arbeit von Erik Hansen auf, die ein solches Kugel-Scheibe Tribometer in stationären Zuständen simuliert, um es für instationäre Effekte zu erweitern. Bei den Simulationen wird eine Mikrotextrur in die Kugeloberfläche eingesetzt und der Algorithmus entsprechend angepasst. Das Ziel dieser Arbeit ist die Validierung der numerischen Vorhersagen durch den Vergleich mit experimentellen Ergebnissen von Literatur. Die verwendeten Gleichungen werden hergeleitet und erläutert. Die numerischen Ansätze und die Funktionsprinzipien der verwendeten Algorithmen werden detailliert beschrieben. Es wird eine gute Übereinstimmung zwischen den Simulationsergebnissen und experimentellen Daten aus der Literatur gefunden. Das Gesamtverhalten des neuen Solvers wird ebenfalls untersucht. Es werden Simulationen mit unterschiedlichen räumlichen Gittergrößen mit proportional skalierten Zeitschritten und konstanten Gittergrößen mit wechselnden Zeitschrittgrößen durchgeführt und analysiert. Es zeigt sich, dass gröbere Gitter großen Abweichungen von den experimentellen Ergebnissen entsprechen, die untersuchten feinsten Gitter aber mit langen Rechenzeiten und großem Rechenaufwand verbunden waren, so dass je nach Anforderung ein Kompromiss getroffen werden muss.

Acknowledgements

Firstly, I would like to sincerely thank my main supervisor Erik Hansen, as his input has been invaluable during the three months that were spent on this work. He has provided the initial algorithm that this work is based upon and has given excellent support, feedback and guidance. Next, I would want to thank both of my parents for the incredible support and motivation they gave me as I was working on this thesis.

Altay Kacan

Contents

1. Introduction	1
1.1. Motivation	1
1.2. State of the Art	2
1.3. Goals and Outline	3
2. Theoretical Fundamentals	5
2.1. Tribological Basics	5
2.1.1. Types of Contacts	5
2.1.2. Tribometers & Friction	6
2.1.3. Lubrication Regimes and Stribeck Curves	6
2.2. Governing Equations of EHL	7
2.2.1. Preliminary Considerations	8
2.2.2. Film Thickness & Linear Elasticity Equations	10
2.2.3. The Reynolds Equation	14
2.2.4. Load Balance & Shear Stress Equations	21
2.3. Constitutive Equations	22
2.4. Summary	25
3. The Numerical Model & The Algorithm	27
3.1. Discretized Equations	27
3.1.1. Discretized Film Thickness Equation	31
3.1.2. Discretized Reynolds Equation	33
3.2. Overview of the Algorithm	36
4. Model Validation & Analysis	45
4.1. Setup & Overview	45
4.2. Validation of the Model	52
4.3. Studies on the Model	59
4.3.1. Grid Size	59
4.3.2. Temporal Resolution	63
5. Conclusion	69
Symbols and Abbreviations	71
List of Figures	75
List of Tables	77
Bibliography	79
Appendix	83
A. Detailed Flowcharts of the Algorithm	83

1. Introduction

1.1. Motivation

Motion is essential to humanity and its development. From constructing the pyramids in ancient Egypt using sledges to constructing automobiles or planes with cutting-edge technology, mankind has always had to move certain things or to harness the energy of motion. Therefore, friction, the resistance against motion, has been a challenge to be dealt with throughout history. Friction causes unwanted energy losses, requiring more energy to be provided to the system at hand. As reducing the CO₂ emissions and ensuring the sustainability of all processes are amongst the main challenges of modern society, it is essential to study friction. The science that deals with the friction, wear and lubrication involved in moving contacts is called *tribology* [1].

One can understand the relevance and importance of tribology in reducing energy losses and therefore CO₂ emissions by considering existing literature. In 2017, Holmberg and Erdemir estimated that 20% of the global energy consumption was spent on overcoming friction. They claimed that advances in tribology could lead to reductions of 1460 metric tons of CO₂ (MtCO₂) and 3140 MtCO₂ in the short and the long term respectively [2]. The same authors estimated in an earlier paper that in a passenger vehicle (excluding braking friction), 28% of the fuel energy is lost due friction in the drivetrain and the engine, while only 21.5% of it is used for moving the car [3]. Even though electric vehicles would have less friction losses due to the absence of a complex gearbox, minimizing the losses would increase the driving range and is still valuable. The question that remains now, is how one might realize these results.

The highest reduction in friction is observed when the lubricant forms a film between the contacting surfaces and separates them. This phenomenon is called *full film lubrication* and when the pressures inside the lubricant are high enough to cause significant elastic deformation of the solids, it is called *elastohydrodynamic lubrication* (EHL)[4]. Additionally, frictional losses can be further reduced by using improved materials and better lubricants with various additives and by introducing textures in the contact surfaces. These textures can both trap debris and store additional lubricant as well as manipulate the hydrodynamic behaviour in a favourable manner. So far the widespread industrial application of texturing methods is not completely realized. The challenge that researches in this field face is the high dependency of texturing parameters on operating conditions and the type of contact. The lack of general statements about optimal texturing parameters is another challenge for standardized use of surface texturing [5]. Therefore, it is essential to have

accurate theoretical models and numerical results to support ongoing experimental research, especially for lubrication problems characterized by high lubricant pressures, such as contacts found in the EHL regime.

1.2. State of the Art

Even though the usage of lubricants to reduce friction between two surfaces in relative motion is not a new concept, only after the Industrial Revolution with increasing rotational speeds beyond the ones of windmills and cart axles, a better understanding of full film lubrication started to become necessary [1]. This began with Tower's discovery of the existence of an oil film of a journal bearing in 1885 and with Petrov's conclusion that such a film must exist after considering friction measurements from experiments in 1883 [6]. Shortly after these advancements, in 1886, Reynolds analytically derived a second-order differential equation for the pressure in the narrow, converging gap between bearing surfaces, creating the foundation of the following theory on full film lubrication and hydrodynamic bearing design [6]. This equation is called the "*Reynolds equation*" and is discussed in detail in the next chapter. For elastohydrodynamic lubrication, as it requires the simultaneous consideration of three equations, for fluid flow, for the elastic deformation of the solids and for the effects of high pressure on the lubricant properties, no mathematical solution was found until Ertel's work in 1945, and the publication of it by Grubin and Vinogradava in 1949 [7, 8]. In the following decades, significant advancements were made both in numerical considerations of the EHL problem and in experimental techniques. This progress is excellently outlined by Spikes and the interested reader is referred to his review of the history of EHL [7].

As for advancements in surface texturing of tribological contacts, research started getting attention in the late 1960s [5]. Hamilton *et al.* discovered that micro-scale irregularities on the surfaces of rotary-shaft face seals created hydrodynamic pressure and contributed to the load carrying capacity. They also observed cavitation, the local creation of vapour bubbles in the liquid lubricant due to low pressures, at the divergent part of the irregularities they were studying [9]. Research in this field accelerated in the following years after promising results were found by Etsion's group [10, 11]. Despite the promising potential of surface texturing, as Gropper *et al.* mention, finding optimal texturing parameters is very challenging and contrary conclusions exist in literature due to the high dependency of the contact behaviour on operating conditions and the situation at hand [5]. It is also important to consider the developments in the methods used to model cavitation in micro-textured EHL contacts. Two main approaches exist when treating cavitation phenomena, the Reynolds model and the Elrod-Adams (EA) implementation [12] of the Jakobsson, Floberg and Olson (JFO) model [13, 14]. The former is known to be non-mass conserving, which is non-physical, while the latter is shown to be mass conserving. Two papers by Giacomini *et al.* [15] and Bertocchi *et al.* [16] reformulate the cavitation condition to obtain a more favourable system of equations and excellently demonstrate the introduction of the mass-conserving cavitation model into the Reynolds equation. The effects of the chosen cavitation model and the importance of a mass-conserving cavitation model for micro-textured contacts are excellently explained by Ausas *et al.* [17] and the interested reader is referred to their cited work. An extensive review of the state of research in the field of lubrication of textured surfaces is provided by Gropper *et al.* in their 2016 paper [5].

In 2015, Woloszynski *et al.* [18] proposed a new algorithm called the *Fischer-Burmeister-Newton-Schur* (FBNS) algorithm based on the JFO mass-conserving cavitation model and its implementation by EA. They showed that this approach is significantly efficient and the computational cost associated with considering cavitation is comparable to cases when cavitation is ignored. This enables the analysis of transient conditions and complex

geometries, as it makes it computationally feasible [18]. Erik Hansen, the supervisor of this thesis, in the recent years has developed an algorithm in MATLAB based on the FBNS algorithm for solving for the pressure distribution in time-independent (steady) EHL contacts [19]¹. This is the point where the work of this thesis begins.

1.3. Goals and Outline

The goals of this bachelor thesis are listed as follows:

1. extend the existing model and system of equations used for the steady solver developed by Erik Hansen to include transient effects in MATLAB,
2. introduce a micro-texture moving through the contact to obtain unsteady flow conditions,
3. validate the developed model and solver by replicating experimental setups and comparing results with experimental data,
4. investigate the overall dependency of the solver on the quality of space and/or time discretization of the computational domain.

In chapter 2, the theoretical considerations necessary to develop models for the phenomena observed in time dependent (unsteady) EHL are provided. Tribological basics and lubrication regimes are explained. Governing equations of the contact are derived. Constitutive equations, that are needed to correlate theoretical predictions of lubricant properties with measured values, are introduced. In chapter 3, the steps taken to discretize the system of equations and the general structure of the developed solver are discussed. Chapter 4 provides the necessary information to carry out simulations with the proposed model. The comparison of the predicted results with the experimental measurements and the analysis of the behaviour of the algorithm are provided and discussed within the same chapter. Finally, in chapter 5, the work done in the scope in this thesis is summarized and proposals for further research are made.

It is important to emphasize that the already existing steady EHL code was developed and supplied by Erik Hansen. The implementation of the necessary changes in this code to model unsteady phenomena and a moving micro-structure as well as obtaining the data by running the simulations was done by the author, Altay Kaçan, while the associated development of the equations and algorithm, the setting up of the simulations and the interpretation of the results are the outcome of discussions with Erik Hansen and are therefore joint work.

¹At the time of the writing of this thesis, a presentation made by the Erik Hansen is being cited for information related to the supplied steady EHL solver that this thesis has been built upon. This solver is a part of his doctoral work and will be published with his PhD thesis in the future.

2. Theoretical Fundamentals

This chapter focuses on explaining physical phenomena behind elastohydrodynamic lubrication (EHL) and the models used to describe them in this thesis. EHL is a type of fluid film lubrication where the contacting surfaces are completely separated by the fluid and the elastic deformation of the solids is of significant magnitude. The load is carried by the generated pressure within the lubricant film and the friction occurs purely from the shearing of the viscous fluid [6]. This way, the lubricant prevents solid to solid contact, reducing friction and wear. The high pressures elastically deform the solid surfaces and drops in pressure lower than the vapour pressure of the lubricant cause cavitation, as explained in more detail in the corresponding section. Thus, it is necessary to have models that represent these various physical phenomena and couple them in a meaningful way.

In the beginning of this chapter, the fundamental types of contact geometries, relevant concepts such as the friction coefficient and the various lubrication regimes are defined. Stribeck curves are introduced to be able to clearly distinguish between lubrication regimes. Then, the model used to describe the contact geometry and the elastic deformation of the solids is explained. Next, the governing equations for the lubricant film are derived from the conservation of mass and momentum. The mass-conserving cavitation model is introduced into the equations. Expressions for the shear stresses which are essential for describing the friction behaviour are derived. The required constitutive equations that correlate experimental results to theoretical models are listed. And finally, all governing equations and assumptions made to obtain them are summarized.

2.1. Tribological Basics

2.1.1. Types of Contacts

Two types of surface contacts, *conformal* and *non-conformal*, are considered in tribology. As their respective names suggest, conformal surfaces match one another geometrically and thus have a large area to carry the load. Non-conformal surfaces have significant geometrical differences which cause a relatively small area to be carrying the load, generating higher pressures compared to conformal contacts for the same load. Slider or journal bearings are examples for conformal surfaces, while gear teeth contact or roller-element bearings correspond to non-conformal surfaces. Hamrock *et al.* further mention in the first chapter of their book, that the lubrication area is usually smaller by three orders of magnitude for non-conformal surfaces compared to conformal ones [6]. Habchi in his more recent work, illustrates the difference clearly in Fig.2.1 [4].

Furthermore, surface contacts in machine elements are classified into *line contacts* and *point contacts*. It is possible to distinguish them by considering the geometry in an unloaded dry contact. The contact between the inner or outer raceway and the cylindrical or ball roller-elements of the corresponding bearings are clear examples of respectively line and point contacts [4].

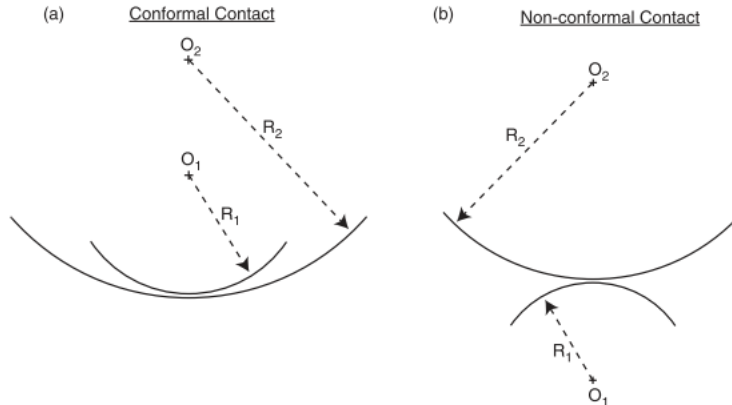


Figure 2.1.: Illustration of surfaces in conformal and non-conformal contacts. Taken from Habchi, 2018 [4].

2.1.2. Tribometers & Friction

Tribometers are measurement devices to replicate less complex than but still representative contacts of the ones found in industry applications. They are used to investigate friction and wear behaviour. There are two standard types of tribometers, ball-on-disc and pin-on-disc tribometers. The contact between either the ball or the pin and the disk is observed while conducting experiments. Ball-on-disc tribometers characterize non-conformal point contacts, therefore they are associated with high hydrodynamic pressures. Since the current work focuses on the numerical simulation of such a device, only the fundamentals required to define the coefficient of friction will be presented here for ball-on-disc tribometers. For more details on the simulated setup please see section 4.1. The friction coefficient, C_f is defined as the absolute value of the ratio of the friction force, F_f and the applied normal load, F_N [20]:

$$C_f = \left| \frac{F_f}{F_N} \right|. \quad (2.1)$$

The friction force is typically calculated by using a torque sensor at the disk to measure the friction moment. The measured moment then is divided by the distance of the contact to the rotation axis of the disk to determine F_f [21].

2.1.3. Lubrication Regimes and Stribeck Curves

Richard Stribeck introduced the concept of plotting the steady state journal bearing friction against the rotational speed at different mean pressures in his 1902 paper, “*Die wesentlichen Eigenschaften der Gleit- und Rollenlager*” [22]. The resulting curves are called *Stribeck curves*. They are useful for determining the friction coefficient and for distinguishing between different lubrication regimes. For a summary of Stribeck’s extensive work, a relatively recent paper by Jacobson is recommended for the interested reader [23].

In modern literature, the dimensionless Hersey number, \mathcal{H} , is plotted against the friction coefficient to additionally capture the effects of mean pressure and lubricant dynamic viscosity. It is defined as:

$$\mathcal{H} = \frac{\mu\Omega}{W}, \quad (2.2)$$

where μ is the dynamic viscosity of the lubricant, W is the mean pressure and Ω is the rotational speed in rotations per second (rps), as adapted from Hamrock *et al* [6] by Codrignani [24]. A contact under low load, with a high viscosity lubricant and high relative velocities between the surfaces corresponds to a high Hersey number and a thicker lubricant film. The vice versa holds for low Hersey numbers [6].

Three main lubrication regimes are distinguished in literature [4, 6] as indicated below the curve in Fig.2.2:

1. *Boundary Lubrication*: At low Hersey numbers a thick enough lubricant film cannot be formed. The load is carried by the solid surfaces. Hence, the friction coefficient is high and the behaviour of the contact is governed by the characteristics of the solid bodies.
2. *Mixed Lubrication*: A steep decrease in the coefficient of friction can be observed as the lubricant film starts to form and its thickness increases. The pressurized lubricant flow assists in carrying the load. Therefore properties of the lubricant as well as the solid surfaces govern this regime.
3. *Full Film Lubrication*: At higher Hersey numbers the lubricant is able to separate the contacting surfaces completely and carries the contact load. The lubricant and flow properties govern the friction coefficient. As it can be seen in Fig.2.2, the plateau where the lowest friction values are reached correspond to the onset of this regime.

The full film lubrication regime can be further distinguished into two sub-regimes: *elasto-hydrodynamic lubrication* (EHL) and *hydrodynamic lubrication* (HL). As mentioned in the introduction of this chapter, the EHL regime is characterized by high pressures that induce the elastic deformation of the contacting solids. The EHL regime is usually observed in non-conformal contacts due to the associated high pressures. Habchi points out, that the magnitude of the elastic deformation is orders magnitude larger than the fluid film thickness, so it is critical to consider its effects. The EHL regime ends as the Hersey number keeps increasing further because the film thickness also starts to increase, reducing the difference of the magnitudes of the film thickness and the elastic deformation [4].

2.2. Governing Equations of EHL

There are multiple interconnected equations that describe the overall behaviour of the solid bodies and the lubricant in EHL. The contact geometry is defined by the film thickness equation which is also influenced by the elastic deformations of the solids. The Reynolds equation governs the flow of lubricant and the hydrodynamic pressure distribution based on contact geometry and flow kinematics. The load balance equation ensures the fulfilment of the force equilibrium between outside loads and the generated pressure within the contact. In the most general case, the energy equation governs the generation of heat due to shear inside the lubricant and its dissipation to the surroundings [4]. For the sake of keeping the presented model simple, the energy equation is not considered by assuming an isothermal flow. These equations are highly dependent on one another, thus provide a challenge in modelling. The pressure distribution depends on the contact geometry and that itself depends on the pressure distribution since it determines the elastic deformation of the solids.

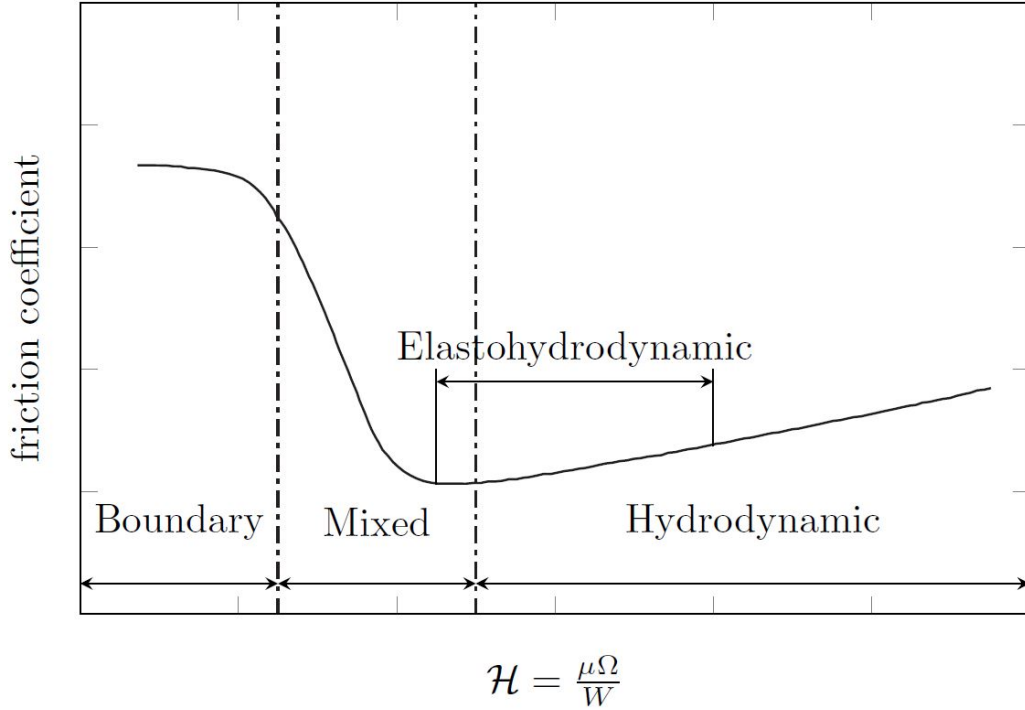


Figure 2.2.: A plot of the Stribeck curve showing the various lubrication regimes. Taken from Codrignani [24] who adapted the figure from Hamrock *et al.* [6].

2.2.1. Preliminary Considerations

Fluid Properties & Conservation Equations

The lubricant is assumed to be a *continuum* to be able to carry out the following derivations, which is the typical approach of modelling fluids. This assumption is justified as long as the considered fluid element volume does not get too small. As mentioned by Durst, in chapter 3.2 of his cited work, orders of magnitude of 10^{-18}m^3 to 10^{-20}m^3 are sufficient for the *continuum hypothesis* to hold [25]. This allows the use the conservation equations of fluid mechanics, namely mass and momentum conservation. The interested reader is referred to Durst and Spurk, as they provide detailed derivations of both equations [25, 26].

Using the index notation for Cartesian tensors, the mass conservation equation (alternatively called, the continuity equation) can be expressed:

$$\frac{D\rho}{Dt} + \rho \frac{\partial u_i}{\partial x_i} = 0, \quad (2.3)$$

where ρ is the density of the fluid, t is time, $\frac{D\rho}{Dt}$ is the material derivative of the density with respect to time and $\frac{\partial u_i}{\partial x_i}$ is the divergence of the field velocity, shown using *Einstein's summation convention*. The material derivative is used for describing temporal changes in material properties in terms of field quantities and is given as [26]:

$$\frac{D}{Dt} = \frac{\partial}{\partial t} + u_i \frac{\partial}{\partial x_i}. \quad (2.4)$$

The other conservation equation is for linear momentum in i -direction, which holds for every continuum, and can be summarized in vector notation:

$$\rho \frac{Du_i}{Dt} = \rho k_i + \frac{\partial \sigma_{ji}}{\partial x_j}, \quad (2.5)$$

where k_i is the component of the mass body forces acting on the fluid in i -direction and σ_{ji} is the stress tensor in index notation. The product ρk_i gives the value of the volume body forces acting in i -direction [26]. The first index of σ gives the direction of the normal vector of the surface the stresses are acting on, and the second gives the direction the stress component is acting in. The stress tensor $[\mathbf{T}]$ is defined as [26]:

$$[\mathbf{T}] = \begin{bmatrix} \sigma_{11} & \sigma_{12} & \sigma_{13} \\ \sigma_{21} & \sigma_{22} & \sigma_{23} \\ \sigma_{31} & \sigma_{32} & \sigma_{33} \end{bmatrix}. \quad (2.6)$$

The diagonal components of the stress tensor are called the *normal stresses* and the non-diagonal ones are named *shearing stresses*. The stress tensor is symmetric, *i.e.* $\sigma_{ij} = \sigma_{ji}$, which can be shown by considering the balance of angular momentum. The stress tensor for an arbitrary state of stress can be written in index notation as:

$$\sigma_{ij} = -p\delta_{ij} + \tau_{ij}, \quad (2.7)$$

where p is the pressure, δ_{ij} is the *Kronecker delta*, which is equal to 1 whenever $i = j$ and equal to 0 otherwise, and τ_{ij} is friction stress tensor [26].

Geometry of the Contact

The following derivations will be considering the point contact of two perfectly smooth surfaces. It is assumed that the lubricant film is thick enough such that the microscopic surface profiles of the surfaces have negligible influence, hence justifying the smooth surface assumption. Typically, the size of the EHL contact is much smaller than the actual geometry of the contacting solids. This allows the approximation of their geometries as elliptic paraboloids as shown in Fig.2.3. The subscript 1 is used for the lower body and 2 for the upper body - or alternatively a and b to avoid confusion in certain cases. The terms R_{x_1} and R_{x_2} are the respective principal radii of curvature with their centers of curvature located at the vertical x_3 -axis. Further simplifications on the contact geometry will be carried out in the following subsections when necessary [4].

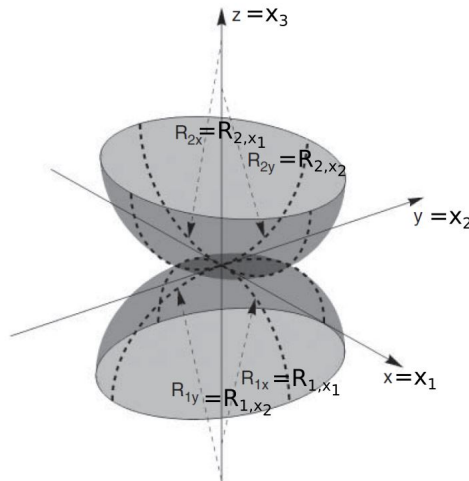


Figure 2.3.: The approximated EHL point contact geometry as two elliptic paraboloids. Adapted from Habchi [4] to include the coordinate notation used in this thesis.

2.2.2. Film Thickness & Linear Elasticity Equations

The Film Thickness Equation

The film thickness equation governs the total gap height, h , at a given point (x_1, x_2) and time t in the contact by incorporating the non-deformed gap height, $h_u(x_1, x_2, t)$, and the total elastic deformation of the solid bodies, $\delta = \delta_1 + \delta_2$. These terms are dealt with when the linear elasticity equations are considered. The starting point of the film thickness equation is [4]:

$$h(x_1, x_2, t) = h_u(x_1, x_2, t) + \delta(x_1, x_2, t). \quad (2.8)$$

The non-deformed gap height term can be further decomposed into the sum of the rigid body displacement term, h_0 , and the non-deformed initial shapes of the solids, h_1 and h_2 [4]:

$$h_u(x_1, x_2, t) = h_0(t) + h_1(x_1, x_2, t) + h_2(x_1, x_2, t). \quad (2.9)$$

h_0 is defined to be the distance of the non-deformed surfaces at the contact center, so on the x_3 -axis in Fig.2.3. The h_1 and h_2 terms can be expressed at a given time t using the equations for elliptic paraboloids [4]:

$$h_1(x_1, x_2, t) = \frac{1}{2R_{1,x_1}(t)}x_1^2 + \frac{1}{2R_{1,x_2}(t)}x_2^2, \quad (2.10)$$

$$h_2(x_1, x_2, t) = \frac{1}{2R_{2,x_1}(t)}x_1^2 + \frac{1}{2R_{2,x_2}(t)}x_2^2. \quad (2.11)$$

In the above equations, the time dependency is typically introduced within the principal radii of curvature terms. In the simulated configurations, the radii of curvature are not time dependent, hence t -dependence will be omitted for h_1 and h_2 . With the definition of an equivalent radius of curvature for both of the bodies the sum of h_1 and h_2 could be further simplified [4]:

$$\frac{1}{R_{x_1}} = \frac{1}{R_{1,x_1}} + \frac{1}{R_{2,x_1}}, \quad (2.12)$$

$$\frac{1}{R_{x_2}} = \frac{1}{R_{1,x_2}} + \frac{1}{R_{2,x_2}}, \quad (2.13)$$

where R_{x_1} and R_{x_2} are the equivalent radii of curvature for the respective directions. Substituting the above equations into to the sum of Eqs.(2.10) and (2.11):

$$h_1(x_1, x_2) + h_2(x_1, x_2) = \frac{x_1^2}{2R_{x_1}} + \frac{x_2^2}{2R_{x_2}}. \quad (2.14)$$

The advantage of this formulation is that the existing problem could be considered as the equivalent contact of an elliptic paraboloid with a flat plane. The elliptic paraboloid would have the equivalent principal radii of curvature since a flat plane is associated infinitely large radii of curvature - its reciprocal value would be zero. This greatly simplifies the formulation of the film thickness equation and the linear elasticity equations as it will be presented in the following [4].

Finally, including the possible effects of surface texturing on the gap height with the terms $S_1(x_1, x_2, t)$ and $S_2(x_1, x_2, t)$, included in $S = S_1 + S_2$, the film thickness equation is obtained [4]:

$$h(x_1, x_2, t) = h_0(t) + \frac{x_1^2}{2R_{x_1}} + \frac{x_2^2}{2R_{x_2}} + \delta(x_1, x_2, t) + S(x_1, x_2, t). \quad (2.15)$$

For more details on how this derivation is carried out, Habchi provides clear and detailed explanations on the matter in chapter 1.2.3 of his often cited work [4] in this thesis. Next, the elastic deformation term in Eq.(2.15) which is governed by the linear elasticity equations of the solids will be discussed.

Elastic Deformation of the Solids

In the model utilized in this current work, the equivalent contact problem of an elastic elliptic paraboloid and rigid plane is considered. This means that after obtaining an equivalent elastic modulus, the analysis of the elastic elliptic paraboloid deforming under pressure load is sufficient to solve for the elastic deformation in the lubrication gap. This is advantageous since the linear elasticity equations have to be solved for only one of the bodies instead of both. This section gives a brief overview of the approach, since the elastic deformation computations were already implemented in the steady MATLAB code that the current work was built upon. The time dependence of the terms involved in the derivation are omitted for visual reasons and it has no influence on the process. Nonetheless, it is introduced at the end of this section.

As usually done in literature, the solid bodies are modelled using the principles of continuum mechanics. The contacting solid bodies are assumed to be *perfectly smooth, homogeneous* and *isotropic*, meaning that no roughness effects are considered and the material properties do not depend on the observed position and spatial direction within the solid [27]. Furthermore, the deformations are considered to be small enough such that the yield stresses of the materials are not exceeded and no plastic deformation takes place. The relatively smaller scale of the contact compared to the curvatures of the surfaces, justify treating them as *elastic half-spaces*, *i.e.* they are completely flat and extend until infinity in all spatial directions except positive x_3 -direction as depicted in Fig.2.4 [4].

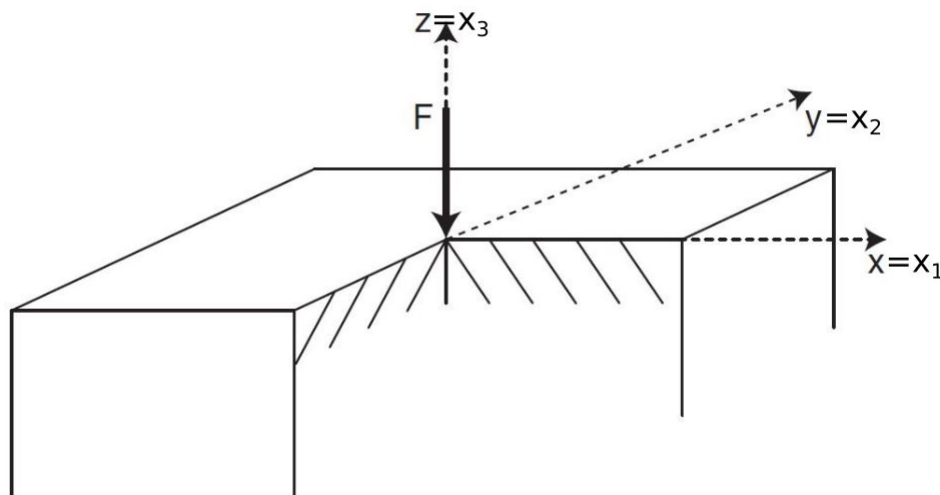


Figure 2.4.: An elastic half-plane loaded by an external concentrated force F . Adapted from Habchi [4] to include the coordinate axes notation.

The starting point for the derivation of the governing equations for the elastic half-space is the consideration of the force balances of the stresses and body forces on a single element of the solid continuum. As shown by Landau [28], the resulting equation that governs the solid body is:

$$\frac{\partial \sigma_{ij}}{\partial x_j} + \rho k_i = 0. \quad (2.16)$$

This equation corresponds to the differential form of the momentum conservation, Eq.(2.5), but with the material derivative of the field velocity terms set equal to zero. Since the momentum conservation holds for any continuum, one might apply the same equation. No inertia effects are observed as long as the solid is moving with an arbitrary but constant velocity, making the left-hand side of the momentum conservation zero. The body forces are neglected, so the second term in the equation above is also set to zero.

Initially an elastic half-space loaded by a normal point force, as in Fig.2.4, is considered. The used sign convention is that positive elastic deformations and contact forces act into the elastic half-space [29]. Substituting into Eq.(2.16) the relationship between stresses and strains, and therefore deformation rates, given by *Hooke's law* for homogeneous, isotropic linear elastic solids, the following expression is obtained for the elastic deformation of an arbitrary point on the half-space in the normal direction to the plane. [4, 28]:

$$\delta(x_1, x_2, x_3) = \frac{F}{4\pi\tilde{\mu}} \frac{x_3^2}{r^3} + \frac{(\tilde{\lambda} + 2\tilde{\mu})F}{4\pi\tilde{\mu}(\tilde{\lambda} + \tilde{\mu})} \frac{1}{r}, \quad (2.17)$$

as given by Habchi [4]. In the above equation $\tilde{\lambda}$ and $\tilde{\mu}$ are the Lamé constants. Furthermore, $r = \sqrt{x_1^2 + x_2^2 + x_3^2}$ is the Euclidean distance between the point of action of the concentrated force (acting on the origin) and the point the elastic deformation, δ , is computed at. The Lamé constants can be expressed in terms of the *Young's modulus*, E , and *Poisson's ratio*, ν , by [4]:

$$\tilde{\lambda} = \frac{E\nu}{(1+\nu)(1-2\nu)}, \quad (2.18)$$

$$\tilde{\mu} = \frac{E}{2(1+\nu)}. \quad (2.19)$$

This is because E and ν are defined by the Lamé constants:

$$E := \frac{\tilde{\mu}(3\tilde{\lambda} + 2\tilde{\mu})}{\tilde{\lambda} + \tilde{\mu}}, \quad \nu := \frac{\tilde{\lambda}}{2(\tilde{\lambda} + \tilde{\mu})}, \quad (2.20)$$

where the second Lamé constant, $\tilde{\mu}$, is often called the *shear modulus* and denoted by G [27]. The model used in this thesis is largely inspired on the formulation of Pohrt and Li [29]. They consider the more general case of the surface elastic deformation with the perpendicular force acting on an arbitrary point (x'_1, x'_2) :

$$\delta(x_1, x_2) = \frac{1-\nu}{2\pi G} \frac{1}{s} F(x'_1, x'_2), \quad (2.21)$$

which is equivalent to Eq.(2.17) computed at the surface, *i.e.* $x_3 = 0$, with $\tilde{\mu}$ substituted as G and generalizing r as s . The equivalence is clear to see when one substitutes $\nu = \frac{\tilde{\lambda}}{2(\tilde{\lambda} + \tilde{\mu})}$ into Eq.(2.21) as briefly outlined next:

$$\frac{1-\nu}{2G} = \frac{1 - \frac{\tilde{\lambda}}{2(\tilde{\lambda} + \tilde{\mu})}}{2\tilde{\mu}} = \frac{\tilde{\lambda} + 2\tilde{\mu}}{4\tilde{\mu}(\tilde{\lambda} + \tilde{\mu})}. \quad (2.22)$$

The Euclidean distance between the point at which the elastic deformation is computed and where the force is applied to is similarly $s = \sqrt{(x_1 - x'_1)^2 + (x_2 - x'_2)^2}$. Pohrt continues by adapting Eq.(2.21) for a pressure distribution, $p(x'_1, x'_2)$, instead of a point load which requires the introduction of an integral [29]:

$$\delta(x_1, x_2) = \frac{1-\nu}{2\pi G} \iint_A \frac{p(x'_1, x'_2)}{s} dx'_1 dx'_2, \quad (2.23)$$

or alternatively written in terms of the Young's modulus, using the previous definitions of the second Lamé constant, $\tilde{\mu} = G$ and the relation between it and E , *i.e.* Eq.(2.19):

$$\delta(x_1, x_2) = \frac{1-\nu^2}{\pi E} \iint_A \frac{p(x'_1, x'_2)}{s} dx'_1 dx'_2. \quad (2.24)$$

This expression is sufficient to compute the elastic deformation of an elastic half-space under a distributed load, which is what the hydrodynamic pressure in the lubricant film is. However, it is valid for only one body and to have a complete solution it must be solved once for each body. The definition of an equivalent Young's modulus, E' , allows the consolidation of the material parameters of both the bodies into one parameter:

$$\frac{2}{E'} := \frac{1-\nu_1^2}{E_1} + \frac{1-\nu_2^2}{E_2}, \quad (2.25)$$

where the subscripts of E and ν denote the body they characterize [30]. Considering that the total elastic deformation is the sum of the individual deformations of each body for a given position (x_1, x_2) , *i.e.* $\delta = \delta_1 + \delta_2$, the following statement can be made:

$$\delta(x_1, x_2) = \underbrace{\frac{1-\nu_1^2}{\pi E_1} \iint_A \frac{p(x'_1, x'_2)}{s} dx'_1 dx'_2}_{\delta_1(x_1, x_2)} + \underbrace{\frac{1-\nu_2^2}{\pi E_2} \iint_A \frac{p(x'_1, x'_2)}{s} dx'_1 dx'_2}_{\delta_2(x_1, x_2)}, \quad (2.26)$$

and since both area the integrals are the same, as they are computed for the same pressure distribution and at the (x_1, x_2) :

$$\delta(x_1, x_2) = \left(\frac{1-\nu_1^2}{\pi E_1} + \frac{1-\nu_2^2}{\pi E_2} \right) \iint_A \frac{p(x'_1, x'_2)}{s} dx'_1 dx'_2, \quad (2.27)$$

which becomes with the substitution of E' as defined in Eq.(2.25) and results in the required form of the linear elasticity equation computed at time t :

$$\delta(x_1, x_2, t) = \frac{2}{\pi E'} \iint_A \frac{p(x'_1, x'_2, t)}{s} dx'_1 dx'_2. \quad (2.28)$$

2.2.3. The Reynolds Equation

In this section, the derivation of the Reynolds equation will be presented and the used mass-conserving cavitation model will be implemented into the equation. The Reynolds equation is the governing equation of the fluid film and the pressure distribution within. The derivation shown here is largely based on the work of Hamrock *et al.* [6]. The starting point of the derivation are the Navier-Stokes Equations (NSE), thus certain assumptions are necessary. For the derivation presented here, the lubricant is assumed to behave as a *Newtonian fluid*, *i.e.* the shear rate is linearly related to the shear stress, and the flow is *laminar* [6].

An important dimensionless number used to characterize whether the flow is laminar or turbulent is the *Reynolds Number*, given by:

$$Re = \frac{\bar{\rho}_0 u_0 l_0}{\bar{\mu}_0} = \frac{\textit{inertia}}{\textit{viscous}}, \quad (2.29)$$

where u_0 is the characteristic velocity, l_0 the characteristic length, $\bar{\rho}_0$ characteristic density and $\bar{\mu}_0$ the characteristic dynamic viscosity¹. It could also be considered as the relative magnitude of the inertial forces compared to the viscous forces. At low Reynolds numbers the flow is usually laminar [6].

The material law for a Newtonian fluid can be expressed in index notation as:

$$\sigma_{ij} = -p\delta_{ij} + \lambda^* e_{kk}\delta_{ij} + 2\mu e_{ij}, \quad (2.30)$$

where the newly introduced term λ^* is a scalar function of thermodynamic state, depending on the material and is named the second viscosity coefficient. δ_{ij} is again the Kronecker delta. The tensor e_{ij} is called the rate of deformation tensor, given by [26]:

$$e_{ij} = \frac{1}{2} \left(\frac{\partial u_i}{\partial x_j} + \frac{\partial u_j}{\partial x_i} \right). \quad (2.31)$$

Furthermore, as shock waves are not of relevance, the *Stokes' hypothesis* is also adopted in the considerations of this thesis:

$$\lambda^* = -\frac{2}{3}\mu, \quad (2.32)$$

which is important to obtain the final form of the Navier-Stokes equations as presented in the following [26].

Navier-Stokes Equations

For an in depth derivation of the NSE and material laws associated with Newtonian fluids, Spurk provides detailed and clear explanations [26]. In the present work, the equations are briefly explained, as the main focus is the Reynolds equation and the used cavitation model. The NSE can be derived by considering the dynamic equilibrium of forces acting on a single fluid element, which are: surface forces, body forces and inertia forces. This is equivalent to inserting the material law for the Newtonian fluid into the momentum conservation equation.

¹The bar is introduced to avoid confusion with parameters that are defined later.

$$\underbrace{\rho \frac{Du_i}{Dt}}_{(I)} = \underbrace{\rho k_i}_{(II)} - \underbrace{\frac{\partial p}{\partial x_i}}_{(III)} - \underbrace{\frac{2}{3} \frac{\partial}{\partial x_i} \left[\mu \frac{\partial u_k}{\partial x_k} \right] + \frac{\partial}{\partial x_j} \left[\mu \left(\frac{\partial u_i}{\partial x_j} + \frac{\partial u_j}{\partial x_i} \right) \right]}_{(IV)}. \quad (2.33)$$

The expression above is the Navier-Stokes equations given in index notation derived by Spurk [26]. The same notation as the previous chapters is adopted, μ is the dynamic or the absolute viscosity of the fluid. The term on the left-hand side is the inertial term, it is the acceleration of a fluid element multiplied by its volume specific mass, term (II) designates body forces, (III) represents the pressure gradient and finally the terms shown by (IV) are the viscous or friction terms. The only body forces acting on the fluid film in EHL is gravity and in some special cases, magnetic forces, both are usually neglected. [6].

Derivation of the Reynolds Equation

The Reynolds Equation can be derived from the Navier-Stokes equations shown in Eq.(2.33) or directly from the conservation of mass, Eq.(2.3), as shown by Hamrock *et al.* In the following, only the first option is presented. Fluid film lubrication problems belong to a class of flow called “slow viscous motion”, meaning that in the NSE, the pressure terms (II) and viscous terms (IV) are much larger in magnitude compared to the other terms. Out of the viscous terms, the ones characterized by the partial derivatives in x_3 -direction and velocities corresponding to the pressure gradient directions, dominate the rest of the viscous terms, and hence, are the ones that are kept. Hamrock *et al.* excellently demonstrate this by conducting an order of magnitude analysis on the various terms of the NSE and then by examining the NSE for flow conditions in real bearings in chapter 7 of their cited work [6].

The results of Hamrock’s order or magnitude analysis on the NSE leads to the first step of the derivation:

$$\frac{\partial p}{\partial x_1} = \frac{\partial}{\partial x_3} \left(\mu \frac{\partial u_1}{\partial x_3} \right), \quad (2.34)$$

$$\frac{\partial p}{\partial x_2} = \frac{\partial}{\partial x_3} \left(\mu \frac{\partial u_2}{\partial x_3} \right), \quad (2.35)$$

$$\frac{\partial p}{\partial x_3} = 0 \longrightarrow p = f(x_1, x_2, t), \quad (2.36)$$

where u_1 and u_2 are the components of the velocity vector corresponding to the coordinate directions [6]. Recalling the flow is assumed to be isothermal, it can be seen that the pressure is a function of only x_1 , x_2 and time. This allows the integration of the first two equations along the gap height direction, x_3 , since the respective pressure terms and therefore their partial derivatives are independent of x_3 . After integrating and rearranging the first two equations to get expressions for velocity gradients, the following is obtained:

$$\frac{\partial u_1}{\partial x_3} = \frac{x_3}{\mu} \frac{\partial p}{\partial x_1} + \frac{c_1}{\mu}, \quad (2.37)$$

$$\frac{\partial u_2}{\partial x_3} = \frac{x_3}{\mu} \frac{\partial p}{\partial x_2} + \frac{c_2}{\mu}, \quad (2.38)$$

where c_1 and c_2 are the integration constants [6]. It is important to mention that the viscosity, μ , is taken to be constant across the gap height, whereas it can change in x_1 - and x_2 -directions. Since temperature is assumed to be constant and pressure does not

vary in x_3 -direction but varies in the other two directions, the assumption of a constant viscosity distribution in the x_3 -direction is justified. If the isothermal flow assumption is dropped, it is possible to consider a mean viscosity across the film that only varies with x_1 and x_2 to be able to follow a similar derivation as presented here [6].

A second integration of Eqs(2.37) and (2.38) in x_3 -direction results in:

$$u_1 = \frac{x_3^2}{2\mu} \frac{\partial p}{\partial x_1} + c_1 \frac{x_3}{\mu} + c_3, \quad (2.39)$$

$$u_2 = \frac{x_3^2}{2\mu} \frac{\partial p}{\partial x_2} + c_2 \frac{x_3}{\mu} + c_4, \quad (2.40)$$

where two new integration constants are obtained [6]. They could be determined by the consideration of boundary conditions at the solid-fluid interfaces. Assuming zero slip between the solid bodies and the lubricant, the following boundary conditions are obtained²:

1. at $x_3 = 0$, $u_1 = u_{1,a}$ and $u_2 = u_{2,a}$,
2. at $x_3 = h$, $u_1 = u_{1,b}$ and $u_2 = u_{2,b}$,

where the velocity components marked with the subscript a and b correspond respectively to the lower and upper solid body surface velocities [6]. It is important to recall that the considered geometry is of the equivalent problem with a flat plate, a , and an elliptical paraboloid, b . After solving for the four integration constants using the boundary conditions given above, the velocities in x_1 - and x_2 -directions alongside their x_3 -gradients can be expressed as:

$$u_1 = -x_3 \left(\frac{h - x_3}{2\mu} \right) \frac{\partial p}{\partial x_1} + u_{1,a} \frac{h - x_3}{h} + u_{1,b} \frac{x_3}{h}, \quad (2.41)$$

$$u_2 = -x_3 \left(\frac{h - x_3}{2\mu} \right) \frac{\partial p}{\partial x_2} + u_{2,a} \frac{h - x_3}{h} + u_{2,b} \frac{x_3}{h}, \quad (2.42)$$

$$\frac{\partial u_1}{\partial x_3} = \left(\frac{2x_3 - h}{2\mu} \right) \frac{\partial p}{\partial x_1} - \frac{u_{1,a} - u_{1,b}}{h}, \quad (2.43)$$

$$\frac{\partial u_2}{\partial x_3} = \left(\frac{2x_3 - h}{2\mu} \right) \frac{\partial p}{\partial x_2} - \frac{u_{2,a} - u_{2,b}}{h}. \quad (2.44)$$

Using these expressions, it is possible to derive equations for the volume flow rates, which are inserted to the continuity equation to derive the Reynolds equation. It is also possible to obtain expressions for shear stresses on the solid-fluid interface, which is presented in section 2.2.4 [6]. The volume flow rates in both directions per unit width are defined in terms of the corresponding velocities as:

$$q'_{x_1} = \int_0^h u_1 dx_3, \quad (2.45)$$

$$q'_{x_2} = \int_0^h u_2 dx_3, \quad (2.46)$$

²The designation of a for the lower body and b for the upper body is the opposite of the notation used by Hamrock *et al.* [6]. This was done to be consistent with Habchi [4] and the rest of this thesis.

which are the velocity profiles integrated along the gap height [6]. For example, multiplying q'_{x_1} by an arbitrary length Δx_2 along the x_2 -axis would result in the volume flow rate in x_1 -direction through the area defined by Δx_2 and h . Since the x_1 - and x_2 -velocities are known from previous derivations, they can be inserted into the above equations:

$$q'_{x_1} = -\frac{h^3}{12\mu} \frac{\partial p}{\partial x_1} + \frac{u_{1,a} + u_{1,b}}{2} h, \quad (2.47)$$

$$q'_{x_2} = -\frac{h^3}{12\mu} \frac{\partial p}{\partial x_2} + \frac{u_{2,a} + u_{2,b}}{2} h. \quad (2.48)$$

These two equations are the superposition of volume flow rates per unit width for two well known cases of fluid flow: *Poiseuille* and *Couette* flow. Thus, the volume flow rate of the lubricant in EHL contacts is the superposition of the volume flow rates associated with them, as illustrated by Fig.2.5. In Poiseuille flow, the pressure gradient causes the fluid to flow between two flat plates. In Couette flow, the flat plates move relatively to each other, which induces shearing of the fluid and causes it to flow [6, 26].

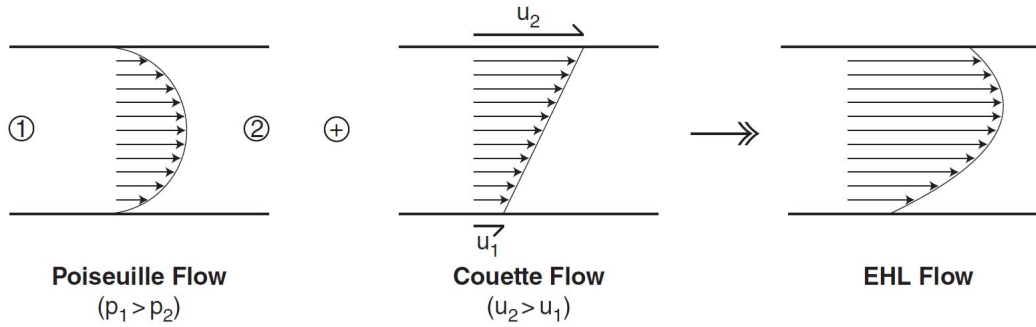


Figure 2.5.: The superposition of the two velocity fields that result in the EHL velocity field, taken from Habchi [4].

It is advantageous to integrate the mass conservation equation, Eq.(2.3), along the gap height since it results in the expressions given in Eqs(2.45) and (2.46) after some mathematical manipulation. The integrated continuity equation after writing out the divergence of the velocity vector, is [6]:

$$\int_0^h \left(\frac{\partial \rho}{\partial t} + \frac{\partial}{\partial x_1}(\rho u_1) + \frac{\partial}{\partial x_2}(\rho u_2) + \frac{\partial}{\partial x_3}(\rho u_3) \right) dx_3 = 0. \quad (2.49)$$

The consideration of a general rule in integration, called *Leibniz integral rule* [6, 31], which is given for the ρu_1 term as:

$$\int_0^h \frac{\partial}{\partial x_1} [f(x_1, x_2, x_3)] dx_3 = -f(x_1, x_2, h) \frac{\partial h}{\partial x_1} + \frac{\partial}{\partial x_1} \left(\int_0^h f(x_1, x_2, x_3) dx_3 \right), \quad (2.50)$$

allows one to rewrite the integrals containing velocities in an advantageous way. If the ρ is assumed to be a mean density, constant across the film height, the u_1 -component in

Eq(2.49) can be calculated:

$$\begin{aligned} \int_0^h \frac{\partial}{\partial x_1}(\rho u_1) dx_3 &= -(\rho u_1)_{x_3=h} \frac{\partial h}{\partial x_1} + \frac{\partial}{\partial x_1} \left(\int_0^h \rho u_1 dx_3 \right) \\ &= -\rho u_{1,b} \frac{\partial h}{\partial x_1} + \frac{\partial}{\partial x_1} \left(\rho \int_0^h u_1 dx_3 \right), \end{aligned} \quad (2.51)$$

where ρ is taken out from the integral since it is assumed not to depend on x_3 . Similarly, the same steps are followed for the u_2 -component:

$$\int_0^h \frac{\partial}{\partial x_2}(\rho u_2) dx_3 = -\rho u_{2,b} \frac{\partial h}{\partial x_2} + \frac{\partial}{\partial x_2} \left(\rho \int_0^h u_2 dx_3 \right), \quad (2.52)$$

and as the u_3 -component has the same integration variable as the partial differentiation variable, x_3 , it can be directly integrated:

$$\int_0^h \frac{\partial}{\partial x_3}(\rho u_3) dx_3 = \rho(u_{3,b} - u_{3,a}), \quad (2.53)$$

where $u_{3,b}$ and $u_{3,a}$ are the x_3 -velocities of the upper and lower surfaces [6].

The integrals in Eqs.(2.51) and (2.52) are precisely the definitions of the volume flow rate per unit width in their respective directions, which were calculated in Eqs.(2.47) and (2.48). Substituting those expressions as well as Eq.(2.53) into the x_3 -integrated continuity equation, given in Eq.(2.49), results in the Reynolds equation [6]:

$$\begin{aligned} 0 &= \frac{\partial}{\partial x_1} \left(-\frac{\rho h^3}{12\mu} \frac{\partial p}{\partial x_1} \right) + \frac{\partial}{\partial x_2} \left(-\frac{\rho h^3}{12\mu} \frac{\partial p}{\partial x_2} \right) + \frac{\partial}{\partial x_1} \left(\frac{\rho h(u_{1,a} + u_{1,b})}{2} \right) \\ &+ \frac{\partial}{\partial x_2} \left(\frac{\rho h(u_{2,a} + u_{2,b})}{2} \right) + \rho(u_{3,b} - u_{3,a}) - \rho u_{1,b} \frac{\partial h}{\partial x_1} - \rho u_{2,b} \frac{\partial h}{\partial x_2} + h \frac{\partial \rho}{\partial t}. \end{aligned} \quad (2.54)$$

The first two terms above are the *Poiseuille terms* and characterize fluid flow rates caused by the pressure gradients. The third and fourth expressions are the *Couette terms*, they describe the fluid flow rates due to the shearing caused by the surface velocities. The last term is called the *local expansion term* and the rest are named *squeeze terms*. Hamrock *et al.* provide detailed explanations of the physical meaning of each term and the interested reader is referred to them [6]. Next, the local expansion term is combined with the squeeze terms. The film thickness, h , is a function of x_1, x_2 and t . Using the definition of the total derivative of the gap height and recalling that $h = f(x_1, x_2, t)$ as Hamrock *et al.* shows:

$$dh = \frac{\partial h}{\partial t} dt + \frac{\partial h}{\partial x_1} dx_1 + \frac{\partial h}{\partial x_2} dx_2, \quad (2.55)$$

which can be rearranged to give:

$$\frac{dh}{dt} = \frac{\partial h}{\partial t} + \frac{\partial h}{\partial x_1} \frac{dx_1}{dt} + \frac{\partial h}{\partial x_2} \frac{dx_2}{dt}, \quad (2.56)$$

where it is important to notice that the total derivative of h with respect to time is equal to the relative vertical velocity by definition, *i.e.* [6]:

$$\frac{dh}{dt} = u_{3,b} - u_{3,a}.$$

Furthermore in Eq.(2.56), the derivatives of x_1 and x_2 on the right-hand side can be expressed as [6]:

$$\frac{dx_1}{dt} = u_{1,b} \quad \text{and} \quad \frac{dx_2}{dt} = u_{2,b}.$$

This is the case, since in the considered equivalent geometry, the lower body (body a) is completely flat and upper body an elliptical paraboloid. Therefore, the lower body cannot induce any change in the gap height by its surface velocity, only the upper body (body b) is capable of that. This is illustrated in Fig.2.6 [6].

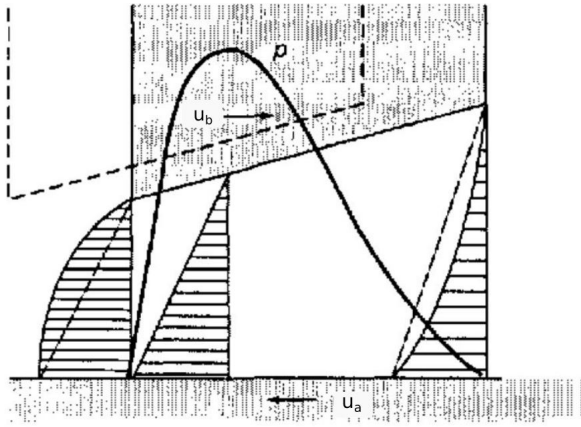


Figure 2.6.: A figure illustrating how the gap height changes as the non-flat upper body (body b) moves from the dashed position to the one drawn as a full line in either direction x_1 or x_2 . Adapted from Hamrock *et al.* to have consistent notation [6].

Substituting the previously obtained expressions, rearranging and multiplying Eq.(2.56) by ρ to get the same expressions as the squeeze terms of Eq.(2.54) on the right-hand side results in [6]:

$$\rho \frac{\partial h}{\partial t} = \underbrace{\rho \left(u_{3,b} - u_{3,a} - u_{1,b} \frac{\partial h}{\partial x_1} - u_{2,b} \frac{\partial h}{\partial x_2} \right)}_{\text{Squeeze terms in the Reynolds equation}}, \quad (2.57)$$

thus, the right-hand side can be substituted into the Reynolds Eq.(2.54) directly as $\rho \frac{\partial h}{\partial t}$ and be combined with the expansion term using the product rule of differentiation as: $\frac{\partial(\rho h)}{\partial t}$. This reduces Eq.(2.54) further and allows a concise formulation using vector notation:

$$\nabla \cdot \left(-\frac{h^3 \rho}{12\mu} \nabla p + \begin{pmatrix} U_1 \\ U_2 \end{pmatrix} \rho h \right) + \frac{\partial(\rho h)}{\partial t} = 0, \quad (2.58)$$

where U_1 and U_2 are the respective mean velocities of the solid bodies in the directions given by their index:

$$U_1 = \frac{u_{1,a} + u_{1,b}}{2}, \quad (2.59)$$

$$U_2 = \frac{u_{2,a} + u_{2,b}}{2}, \quad (2.60)$$

and the two dimensional ∇ operator, $\nabla = \left(\begin{array}{c} \frac{\partial}{\partial x_1} \\ \frac{\partial}{\partial x_2} \end{array} \right)$, denoting the gradient operator with ∇ and the divergence operator with $\nabla \cdot$ for a vector quantity [6, 32].

Cavitation

Cavitation is a phenomenon that occurs in liquids whenever the pressure drops below the vapour pressure of the fluid. It is the formation and the collapse of regions of vapour bubbles within the liquid, as the liquid locally boils, since the boiling point of the liquid drops with decreasing pressure [26]. In textured contacts, cavitation is observed and since it creates a region of vapour, has a significant impact on the pressure distribution, and thus, the load carrying capacity [5]. The occurrence of cavitation prevents the predicted pressures from attaining negative values, which would be non-physical otherwise. The pressure is bounded from below by the vapour pressure which is assumed to be the cavitation pressure, p_{cav} . Since the hydrodynamic pressures in EHL contacts reach comparatively high values, the vapour pressure can be neglected and the pressure can be assumed to not drop lower than ambient pressure [30]. Many cavitation models have been proposed in literature but as Ausas *et al.* show, whether the model conserves mass or not, is critical in determining the load carrying capacity [17]. In this section, the used mass-conserving cavitation model based on the Jakobsson, Floberg and Olson (JFO) [13, 14] model and its implementation by Elrod and Adams (EA) [12] is presented and introduced into the Reynolds equation. The goal is to have a similar form of the Reynolds equation as the one used by Woloszynski *et al.* [18] as they use the same cavitation model as a starting point for their proposed algorithm.

Introducing the quantity θ as *cavity fraction*:

$$\theta = 1 - \frac{\rho}{\rho_l}, \quad (2.61)$$

where ρ is the average density of the lubricant within the film, which may vary since the cavitated fluid is a mixture of liquid and vapour, and ρ_l is the density of the non-cavitated fluid [18]. The film region where cavitation is observed is called the *non-active region*, and the region without cavitation is called the *active region* or *full film region*. The cavity fraction can only take values between 0 and 1. It is assumed when the lubricant fully cavitates at a given region, it has a density of zero, *i.e.* $\theta = 1$. And when there is no cavitation, the average density of the lubricant film is equal to the density of the liquid as there is only liquid lubricant, $\rho_l = \rho$, so $\theta = 0$ holds. The pressure within the non-active region is assumed to be equal to p_{cav} , while in the active region, it is assumed to be equal to or greater than the cavitation pressure [15]. This formulation can be expressed in terms of *linear complementary* and introduced into the Reynolds equation, Eq.(2.58), as shown by Giacomini *et al.* [15] and Bertocchi *et al.* [16] with $\bar{p} = p - p_{cav}$:

$$\nabla \cdot \left(-\frac{h^3 \rho_l}{12\mu} \nabla \bar{p} + \begin{pmatrix} U_1 \\ U_2 \end{pmatrix} \rho_l h (1 - \theta) \right) + \frac{\partial}{\partial t} (\rho_l h (1 - \theta)) = 0, \quad (2.62)$$

$$\bar{p} \geq 0, \quad \theta \geq 0 \quad \text{and} \quad \bar{p} \cdot \theta = 0, \quad (2.63)$$

as used by Woloszynski *et al.* [18]. This is possible since the cavitation pressure is constant and its influence would be cancelled out in the pressure gradient. The condition $\bar{p} \cdot \theta = 0$ ensures, when there is cavitation, so when $\theta \neq 0$ holds, the pressure has to be equal to the cavitation pressure, *i.e.* $\bar{p} = p - p_{cav} = 0$. Eq.(2.62) is the Reynolds equation with the mass-conserving cavitation model introduced and the relations in Eq.(2.63) are called the cavitation conditions.

In this work, the procedure of obtaining the above equation is briefly outlined. The Reynolds equation is mathematically manipulated by rewriting $\rho = \rho + \rho_l - \rho_l$ and rearranged in a way to include θ . During the derivation, the consideration of the product: $\theta \cdot \nabla \bar{p}$ and the fact that it is zero in both the active region and the non-active region allows some terms in the equation to be neglected. The product is unknown at the boundaries between the regions, so it is assumed be zero for simplicity. The interested reader is encouraged to read the aforementioned papers for further information Giacopini *et al.* [15] and Bertocchi *et al.* [16] as the derivation in this thesis is analogous.

2.2.4. Load Balance & Shear Stress Equations

The Load Balance Equation

The load balance equation, as its name suggests, describes the equilibrium of forces over the contact. By definition, the solid surfaces are not in contact, thus, the external load is completely supported by the pressure generated within the lubricant film. Denoting the domain of the contact with Ω_c , the force balance in x_3 -direction results in:

$$\int_{\Omega_c} p(x_1, x_2, t) - p_0 dx_1 dx_2 = F_3(t) (= F_3), \quad (2.64)$$

where the external force in x_3 -direction is designated with $F_3(t)$ and the ambient pressure with p_0 . Recall that the pressure is independent of x_3 and its resultant force is much larger than the inertia and body forces, allowing them to be neglected [4]. In the simulated setup the force is not time dependent but it is stated as so in this section for considering the most general case.

The Shear Stress Equations

The shear stress distribution on the solid-fluid interfaces are of importance, because their integrals are defined as the friction force felt on the contact. The solids do not contact one another, and this results in the friction force being generated only by the shearing of the fluid between them. As mentioned during the derivation of the Reynolds equation, the obtained velocity gradients in x_1 - and x_2 -direction allow for the calculation of the shear stress distribution. Recalling the velocity gradients from Eqs.(2.43) and (2.44):

$$\frac{\partial u_1}{\partial x_3} = \left(\frac{2x_3 - h}{2\mu} \right) \frac{\partial p}{\partial x_1} - \frac{u_{1,a} - u_{1,b}}{h},$$

$$\frac{\partial u_2}{\partial x_3} = \left(\frac{2x_3 - h}{2\mu} \right) \frac{\partial p}{\partial x_2} - \frac{u_{2,a} - u_{2,b}}{h},$$

which are also present in the definition of the viscous shear stresses:

$$\tau_{31} = \tau_{13} = \mu \left(\frac{\partial u_3}{\partial x_1} + \frac{\partial u_1}{\partial x_3} \right), \quad (2.65)$$

$$\tau_{32} = \tau_{23} = \mu \left(\frac{\partial u_3}{\partial x_2} + \frac{\partial u_2}{\partial x_3} \right), \quad (2.66)$$

it is possible to obtain an expression for shear stresses by a simple substitution of the known velocity gradients. The unknown velocity gradients $\frac{\partial u_3}{\partial x_2}$ and $\frac{\partial u_3}{\partial x_1}$ are shown to be negligible by Hamrock *et al.* after an order of magnitude analysis [6]. This results in:

$$\tau_{31} = \tau_{13} = \mu \frac{\partial u_1}{\partial x_3}, \quad (2.67)$$

$$\tau_{32} = \tau_{23} = \mu \frac{\partial u_2}{\partial x_3}. \quad (2.68)$$

Substituting the respective velocity gradients given in Eqs.(2.43) and (2.44) into the equations for the shear stresses. Given in vector notation:

$$\begin{pmatrix} \tau_{31} \\ \tau_{32} \end{pmatrix} = \frac{2x_3 - h}{2} \nabla p - \frac{\mu}{h} \begin{pmatrix} u_{1,a} - u_{1,b} \\ u_{2,a} - u_{2,b} \end{pmatrix}. \quad (2.69)$$

Only the shear stresses at the solid surfaces are of interest, thus they are computed at $x_3 = 0$ for the lower surface and $x_3 = h$ for the upper surface, resulting in four expressions, two for each body:

$$(\tau_{31})_{x_3=0} = \left(\mu \frac{\partial u_1}{\partial x_3} \right)_{x_3=0} = -\frac{h}{2} \frac{\partial p}{\partial x_1} - \frac{\mu(u_{1,a} - u_{1,b})}{h}, \quad (2.70)$$

$$(-\tau_{31})_{x_3=h} = -\left(\mu \frac{\partial u_1}{\partial x_3} \right)_{x_3=h} = -\frac{h}{2} \frac{\partial p}{\partial x_1} + \frac{\mu(u_{1,a} - u_{1,b})}{h}, \quad (2.71)$$

$$(\tau_{32})_{x_3=0} = \left(\mu \frac{\partial u_2}{\partial x_3} \right)_{x_3=0} = -\frac{h}{2} \frac{\partial p}{\partial x_2} - \frac{\mu(u_{2,a} - u_{2,b})}{h}, \quad (2.72)$$

$$(-\tau_{32})_{x_3=h} = -\left(\mu \frac{\partial u_2}{\partial x_3} \right)_{x_3=h} = -\frac{h}{2} \frac{\partial p}{\partial x_2} + \frac{\mu(u_{2,a} - u_{2,b})}{h}, \quad (2.73)$$

where the shear stresses corresponding to the opposite surfaces have opposite signs [6] and μ is assumed to not depend on the previously defined cavity fraction, θ .

2.3. Constitutive Equations

The knowledge of accurate models to describe the measured lubricant behaviour and properties is essential for solving the EHL problem [4]. The model used in this thesis considers a *compressible, piezoviscous* lubricant, which means that the density and the dynamic viscosity, respectively, change with pressure. The temperature dependency of lubricant properties is not relevant as temperature changes are neglected. Constitutive equations are usually obtained by fitting models to experimental data [4].

Additionally, the lubricant begins to show *non-Newtonian behaviour* as shear stresses reach high values, meaning that the viscosity has a shear dependency. Even though during the derivation of the Reynolds equation (section 2.2.3) a Newtonian fluid was assumed, it is an idealized model and in reality a *Newtonian limit* for the shear stress exists [4]. Thus, it is necessary to model the shear dependency of the viscosity and adjust it in the Reynolds equation.

In this section, the equations used to describe the pressure dependency of the lubricant density and pressure-shear dependency of lubricant viscosity are presented. As mentioned

in section 2.2.4, the presence of cavitation is assumed not to influence the dynamic viscosity of the lubricant, *i.e.* $\mu = \mu_l$. Nonetheless, μ_l is used in the following to keep in mind that the constitutive equations are meant to be for the liquid lubricant. In the following, the required material parameters are given as provided by Mourier *et al.* [21] as the simulations done to validate the model are based on their experiments. More details on the specifics are provided in chapter 4.1. The explanations as to how to couple the constitutive equations to the previously derived equations are shown in chapter 3.

Density - Compressibility

Typically, equations linking the pressure, density and temperature of materials are called *equations of state (EoS)* [4]. Venner and Bos have shown that the central film thickness within the EHL contact is reduced proportionally to the compression of the lubricant, demonstrating the importance of including compressibility effects in the model [33]. In the current work, the *Dowson-Higginson model* is used:

$$\rho_l = \rho_0 \frac{C_1 + C_2 \frac{p}{\text{Pa}}}{C_1 + \frac{p}{\text{Pa}}}, \quad (2.74)$$

where ρ_l is the density of the lubricant at pressure p and ρ_0 its density at atmospheric pressure. C_1 and C_2 being constants depending on the lubricant. As proposed by Dowson-Higginson the constants are assumed to be $C_1 = 5.9 \cdot 10^8$ and $C_2 = 1.34$ [34]. The pressures are divided by their unit Pa for consistency.

Viscosity - Piezoviscosity

The piezoviscosity of the fluid refers to the pressure dependence of the viscosity. The viscosity usually increases as pressure increases [16] and the chosen model to describe the relationship between them is the *Roelands model* based on experimental results:

$$\mu_l = \mu_0 e^a, \quad (2.75)$$

where μ_l is the dynamic viscosity of the liquid lubricant at the given pressure, μ_0 its viscosity at atmospheric pressure and a being:

$$a := \left(\ln \left(\frac{\mu_0}{\text{Pa} \cdot \text{s}} \right) + 9.67 \right) \left(-1 + \left(1 + \frac{p}{\tilde{p}_0} \right)^Z \right), \quad (2.76)$$

as proposed by Roelands in his PhD work [35]. The exponent Z is defined as:

$$Z = \frac{\alpha \tilde{p}_0}{\ln \left(\frac{\mu_0}{\text{Pa} \cdot \text{s}} \right) + 9.67}, \quad (2.77)$$

where α is the pressure viscosity index and \tilde{p}_0 is the pressure coefficient defined for the Roelands relation according to Mourier *et al.* [21]. The viscosity and the pressure are divided by their respective units to have consistent notation. The values of these coefficients are provided in chapter 4.1, when the parameters for the carried out simulations are discussed.

Viscosity - Shear Dependence

Under very high shear stresses, the Newtonian limit of the fluid is exceeded and the fluid starts to show non-Newtonian behaviour - the viscosity depends on the shear stresses. There are many variants of non-Newtonian behaviour and not all are in the scope of this work. Some fluids show a *shear-thickening effect*, the viscosity increases with increasing shear, and some show a *shear-thinning effect*, increasing shear causes the viscosity to decrease. Most mineral oil based lubricants exhibit shear thinning behaviour. The shear stresses and shear rates in x_1 - and x_2 -directions are combined respectively as: $\tau = \sqrt{\sigma_{31}^2 + \sigma_{32}^2}$ and $\dot{\gamma} = \sqrt{\dot{\gamma}_{31}^2 + \dot{\gamma}_{32}^2}$ [4]. Fig.2.7 illustrates the various lubricant behaviours mentioned so far.

The shear thinning model used in this thesis assumes a limiting shear stress value specific for the lubricant, τ_{max} . The shear stress that would occur in pure Couette flow, as outlined in section 2.2.3 and in Eq.(2.5), is calculated with the current lubricant viscosity, μ_l and is taken as an average value that is compared to the limiting shear stress. The Couette flow is characterized by a linear velocity profile and a zero pressure gradient [26], hence the velocity gradients in Eqs.(2.65) and (2.66) can be simply calculated as the relative velocity between the bodies divided by the gap height. For a generalized shear stress, τ_{avg} , this results in:

$$\tau_{avg} = \mu_l \frac{u_r}{h}, \quad (2.78)$$

where $u_r = u_b - u_a$ is the relative velocity between the bodies, h the gap height and μ_l the lubricant dynamic viscosity.

The lubricant viscosity is adjusted to be the viscosity corresponding to τ_{max} whenever $\tau_{avg} > \tau_{max}$. The adjusted viscosity is calculated as:

$$\mu_l = \frac{\tau_{max} h}{u_r}, \quad (2.79)$$

in which h is the gap height corresponding to locations where the average shear stress exceeds the predefined maximum shear stress. Recall that the Couette shear stresses are used as average values in this model, which allows the relatively simple formulation. The adjusted μ_l is substituted to the Reynolds equation, this procedure is not done simultaneously and its explanation will be detailed in chapter 3. This continuous adjustment corresponds to limiting the average shear stress within the lubricant film to never be able to exceed the maximum shear stress as illustrated in Fig.2.7 (c). Even though the Reynolds equation in the previous section was derived under the assumption of a Newtonian fluid, it can still be used with the introduced shear thinning model. The shear stresses are modelled as the product of an *effective viscosity* and the corresponding velocity gradient, similar to a Newtonian fluid, thus, allowing the derived Reynolds equation to be used. All non-Newtonian effects are considered through a change of the effective viscosity, which corresponds to the adjusted viscosity presented in this section.

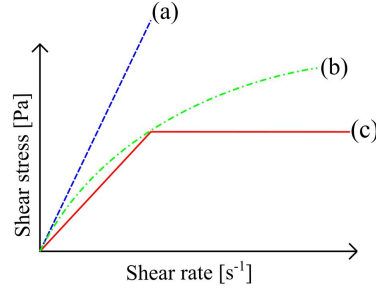


Figure 2.7.: Shear stress against shear rate of different types of fluids: (a) Newtonian (b) Shear-thinning (c) Assumed behaviour in this thesis. Inspired by Durst [25].

2.4. Summary

Now that the required equations have been obtained to model the EHL problem, a concise summary of the equations and the assumptions to derive them are presented before moving on to the numerical model and the solver algorithm. Summarizing the found governing equations of EHL:

$$\nabla \cdot \left(-\frac{h^3 \rho_l}{12\mu} \nabla \bar{p} + \begin{pmatrix} U_1 \\ U_2 \end{pmatrix} \rho_l h(1 - \theta) \right) + \frac{\partial}{\partial t} (\rho_l h(1 - \theta)) = 0, \quad (2.62 \text{ revisited})$$

$$\bar{p} \cdot \theta = 0 \quad \text{with } \bar{p}, \theta \geq 0 \quad \text{and } \bar{p} = p - p_{cav}, \quad (2.63 \text{ revisited})$$

$$\begin{pmatrix} \tau_{31} \\ \tau_{32} \end{pmatrix} = \frac{2x_3 - h}{2} \nabla p - \frac{\mu}{h} \begin{pmatrix} u_{1,a} - u_{1,b} \\ u_{2,a} - u_{2,b} \end{pmatrix}, \quad (2.69 \text{ revisited})$$

$$h(x_1, x_2, t) = h_0(t) + \frac{x_1^2}{2R_{x_1}} + \frac{x_2^2}{2R_{x_2}} + \delta(x_1, x_2, t) + S(x_1, x_2, t), \quad (2.15 \text{ revisited})$$

$$\delta(x_1, x_2, t) = \frac{2}{\pi E'} \iint_A \frac{p(x'_1, x'_2, t)}{s} dx'_1 dx'_2, \quad (2.28 \text{ revisited})$$

$$\text{with the definition } \frac{2}{E'} := \frac{1 - \nu_1^2}{E_1} + \frac{1 - \nu_2^2}{E_2},$$

$$\int_{\Omega_c} p(x_1, x_2, t) - p_0 dx_1 dx_2 = F_3. \quad (2.64 \text{ revisited})$$

The first equation is the Reynolds equation including the cavity fraction that governs the pressure distribution within the fluid for given geometries, lubricant properties and operating conditions, the second equation describes shear stresses across the film, the third is the film thickness equation which governs the geometry of the contact, and fourth the linear elasticity equation that consolidates the elastic deformation of both solid bodies in one equation. The last equation is the load balance equation which ensures that the generated pressure within the lubricant balances the outside load in the vertical direction. The lubricant properties are governed by the constitutive equations outlined in section 2.3.

The assumptions that were made to obtain these equations are:

- the operating conditions are always within the EHL regime,
- the lubricant and the solid bodies are modelled using continuum mechanics,
- the equivalent geometry of a rigid elliptic paraboloid contacting an elastic flat surface is considered,
- solids are perfectly smooth, isotropic, homogeneous and show linear elastic behaviour,
- no plastic deformation takes place,
- the gap height (h) is small compared to the curvatures of the surfaces, justifying the use of elastic half-plane theory,
- the lubricant flow is laminar and isothermal and the Stokes' hypothesis holds,
- body forces and inertial forces are negligible in the NSE, as the pressure and viscous terms dominate,
- hydrodynamic pressure, p , liquid lubricant density, ρ_l , and lubricant viscosity, $\mu = \mu_l$ are constant throughout the film thickness, *i.e.* in x_3 -direction,
- there is no slip at the solid-fluid interface,
- u_3 -velocity gradients in x_1 - and x_2 -direction are negligibly small, *i.e.* $\frac{\partial u_3}{\partial x_1} = \frac{\partial u_3}{\partial x_2} = 0$.

The equations listed above combined with the constitutive equations that describe relationships between the material properties and the operating conditions form the basis of the equation system to be solved. Since no analytical solutions exist, to solve the system, numerical methods have to be used.

3. The Numerical Model & The Algorithm

The Reynolds equation, similarly to other equations in fluid mechanics, such as the fundamental equations of mass and momentum conservation or the Navier-Stokes equations, is only analytically solvable for a limited number of flows and under strict assumptions [4, 36]. Furthermore, the high interdependency between the Reynolds equation and the other governing equations that were presented, make the problem highly non-linear. The use of numerical methods is thus essential.

Firstly, the basics of the used numerical methods are briefly described, as the main focus is the discretization of the equations and the overall solution strategy. Then, the previously obtained system of equations are discretized and coupled with one another. After outlining the discretization of the film thickness equation and the Reynolds equation, the algorithms used to solve them are described. The implemented algorithm for solving the Reynolds equation, namely the *Fischer-Burmeister-Newton-Schur* (FBNS) algorithm, is largely inspired by the work of Woloszynski *et al.* [18]. For solving the linear elasticity equation, the fast Fourier transform (FFT) based boundary element formulation, introduced by Pohrt and Li [29] is used. Then, the structure of the developed solver is presented alongside the used boundary conditions and the chosen methods of overcoming non-linearities without compromising accuracy. For detailed information on computational fluid mechanics, the interested reader is referred to Ferziger [36] and for in depth explanations of the respective algorithms to Woloszynski *et al.* [18] and to Pohrt and Li [29].

The provided algorithm for the steady EHL case was developed by Erik Hansen, the supervisor of this thesis, and is the foundation of this work. The supplied steady solver, which is based on the previously mentioned FBNS algorithm and the boundary element formulation of Pohrt and Li, is extended to include the combined squeeze and expansion terms in the Reynolds equation. The new terms are discretized and the system the FBNS algorithm solves is adapted to include them. A micro-texture is introduced and moved through the contact by the means of a time loop that marches through time. Both the algorithm that this thesis builds upon and the newly added features are explained in detail in the rest of this chapter.

3.1. Discretized Equations

Discretization methods are used to obtain numerical approximations around small regions of space and/or time. Each of these small regions are discrete points and are called

computational nodes for spatial discretization. Discretizing a differential equation around a small region allows for reasonable approximations of the equation around that region by a system of algebraic equations, which are then solved by a computer. This approach is particularly useful for approximating solutions for partial differential equations, which also include the Reynolds equation [4, 36].

The solid bodies are discretized using the *boundary element method*, which is explained in more detail in the following sections. The constitutive equations are calculated directly for each computational node depending on the pressure of that grid point, this is a straightforward procedure and hence is not detailed in this section. In the following, the chosen discretization and approximation methods used for the lubricant are presented. The spatial discretization of the domain and the film thickness equation is adopted without any changes from the supplied steady EHL solver. The discretization of the time derivative term in the Reynolds equation, Eq.(2.62), is one of the tasks of this thesis and therefore is explained in detail.

Spatial Discretization

The lubricant is discretized using a *finite volume* (FV) approach, which actually corresponds to a *finite area* (FA) method as the equation of interest, the Reynolds equation, is two dimensional. Finite volume methods are based on the principle of sub-dividing the domain into a finite number of small control volumes (CVs) and calculating the integral forms of the equations to be solved for each CV. The values of the integrals are approximated at CV surfaces by using interpolation methods [36].

The grid used is a Cartesian, N -by- N , regular, square grid¹. The computational nodes are defined by specifying the x_1 - and x_2 -coordinates of the boundary nodes of the domain and the total amount of nodes in each direction. The required spacing between each node is then calculated. A regular grid of CVs is constructed by defining a CV around each computational node as it can be observed in Fig.3.1. The indices i , in x_1 -direction, and j , in x_2 -direction, are used to label the nodes. The center node (i, j) is labeled as “C”. The surrounding nodes are named in a similar manner with capital letters corresponding to the four compass directions: north, west, south and east. The surfaces are denoted with lower case letters corresponding to their direction relative to the center node and are characterized by *outward-pointing normal vectors* [36]. An illustration of the grid and the space discretization can be seen in Fig.3.1.

Interpolation Methods

Each variable and also the gradients of those variables that were present in the theoretical considerations of chapter 2 are calculated for each computational node. In order to be able to calculate the values of the integrals computed at CV boundaries, *interpolation methods* are necessary, as only the values at the CV centers are known. Using a generalized variable, ϕ , the utilized interpolation methods are presented next based on Fig.3.1 and the work of Ferziger [36].

Upwind interpolation or the *upwind-differencing scheme* (UDS) is a method of approximating the values of ϕ at the boundaries as the value of the next node upstream of the surface, hence the name. If \vec{u} is taken to be the flow velocity pointing in positive x_1 -direction, and the east boundary is considered, this approach would correspond to assigning the value at the node that is reached when the velocity vector is “traced back” as the value at the CV surface.

¹The implementation of the code allows for N_{x_1} -by- N_{x_2} regular grids as well.

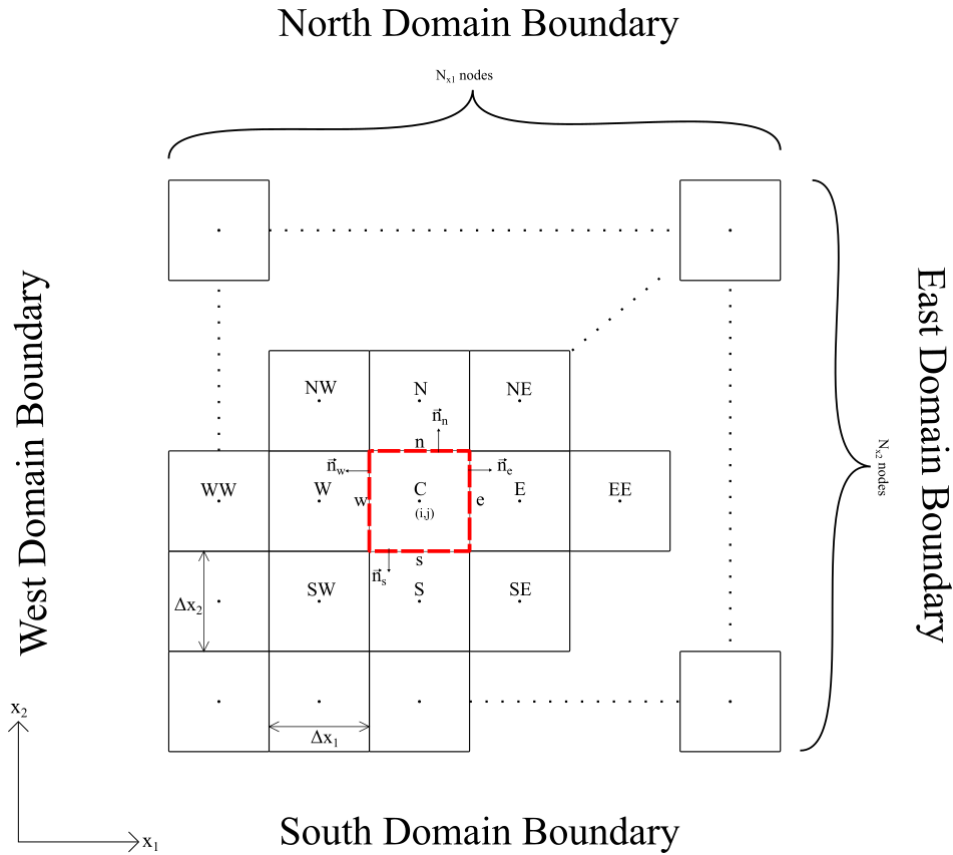


Figure 3.1.: An illustration of the used 2D grid in the algorithm where the dashed red square (also bold) is the $(i, j)^{th}$ control volume of interest. The symbols \vec{n} correspond to outward-pointing normal vectors of the surfaces. For the developed algorithm $N_{x_1} = N_{x_2}$ holds. Design inspired by Ferziger [36].

The UDS can be expressed mathematically:

$$\phi_e = \begin{cases} \phi_C & \text{if } (\vec{u} \cdot \vec{n})_e > 0; \\ \phi_E & \text{if } (\vec{u} \cdot \vec{n})_e < 0. \end{cases} \quad (3.1)$$

where ϕ_e is the value at the east boundary, ϕ_E and ϕ_C the values at the east and the center nodes and “ \cdot ” the scalar product between two vectors. The result of $(\vec{u} \cdot \vec{n})_e$ is positive only when the projection of the velocity vector on the east surface normal is in the same direction as the normal. The discretization error of this scheme is of first-order, as mentioned by Ferziger [36].

Linear interpolation or the *central difference scheme* (CDS) is similar to UDS but instead of assigning the value of one of the neighbouring nodes, it considers both neighbours. Based on the same example provided for UDS, a linear interpolation would be:

$$\phi_e = \phi_E \lambda_e + \phi_C (1 - \lambda_e), \quad (3.2)$$

where λ_e is the linear interpolation factor for the east boundary, defined based on the grid spacings as:

$$\lambda_e = \frac{x_{1,e} - x_{1,C}}{x_{1,E} - x_{1,C}}, \quad (3.3)$$

where the terms on the right-hand side denote the x_1 -coordinates of the corresponding nodes. This scheme is a second-order scheme as it can be seen from the Taylor series expansion [36]. Since the grid used in the solver is equally spaced in all directions, the linear interpolation factors are equal for all boundaries and Eq.(3.2) reduces to:

$$\phi_e = \frac{\phi_E + \phi_C}{2}, \quad (3.4)$$

As CDS assumes a linear profile between neighbouring nodes, the derivatives at the CV surfaces can be calculated for the approximated profile and correspond to the slope of a straight line. Continuing with the simple example outlined above:

$$\left(\frac{\partial \phi}{\partial x_1} \right)_e \approx \frac{\phi_E - \phi_C}{x_{1,E} - x_{1,C}} = \frac{\phi_E - \phi_C}{\Delta x_1} \quad (3.5)$$

where Δx_1 was introduced for shorthand notation and indicates the distance between two nodes in the grid in x_1 -direction [36].

Temporal Discretization

Time also has to be discretized to be able to use numerical methods and computers for transient problems. The time discretization is one of the main tasks of this thesis as the supplied steady solver only considers time independent EHL configurations. The *Euler implicit method* is used, as it typically provides stable results. Time is separated into discrete intervals, Δt , which are referred to as *time steps* and the discrete points in time are called *time points*. As in nature, for unsteady problems, an initial condition is given and all other following solutions are calculated step-by-step, essentially “marching” through time. The fundamental approaches to time discretization are presented in the following. For ease of explanation, a one dimensional initial value problem in the form of:

$$\frac{d\phi(t)}{dt} = f(t, \phi(t)) ; \quad \phi(t_0) = \phi^0, \quad (3.6)$$

where ϕ is the time dependent variable of interest, $f(t, \phi(t))$ an arbitrary function of time and ϕ, t_0 the initial time and ϕ^0 the known value of the variable at time t_0 , is considered. The approach is to find the value of ϕ for the next time point Δt after t_0 , *i.e.* finding ϕ^1 for $t_1 = t_0 + \Delta t$. Then, using the obtained solution for t_1 as an initial condition for solving the same problem for $t_2 = t_1 + \Delta t$, the value of ϕ for t_2 , denoted by ϕ^2 , can be solved for. This scheme can be continued arbitrarily. The adopted notation is to index time with the corresponding subscripts and ϕ with superscripts to avoid confusion with indices used in spatial discretization [36]. The explicit and implicit Euler methods can be constructed for the n^{th} time point, $t_{n+1} = t_n + \Delta t$ after integrating Eq.(3.6) from t_n to t_{n+1} :

$$\int_{t_n}^{t_{n+1}} \frac{d\phi(t)}{dt} dt = \phi^{n+1} - \phi^n = \int_{t_n}^{t_{n+1}} f(t, \phi(t)) dt. \quad (3.7)$$

Due to the time derivative in Eq.(3.6), the left-hand side can be easily integrated and the result is exact, *i.e.* there is no error $\phi^n = \phi(n)$ and $\phi^{n+1} = \phi(n+1)$. However, numerical approximation for the integral of $f(t, \phi(t))$ is necessary. As it can be seen in Fig.3.2, the difference between the explicit and implicit Euler methods lies in the method for approximating this time integral [36].

The *explicit* or the *forward Euler method* approximates the integral on the right-hand side of Eq.(3.7) by taking the known value of $f(t, \phi(t))$ at time t_n and assuming it to be

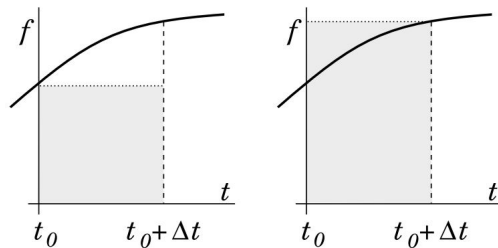


Figure 3.2.: The illustration of *explicit* (left) and *implicit* (right) Euler methods to approximate the time integral in Eq.(3.7). Taken from Ferziger [36]

constant until the next time point, t_{n+1} . This allows the simple calculation of the integral, considering ϕ^{n+1} is the unknown, results in:

$$\phi^{n+1} = \phi^n + f(t_n, \phi^n) \Delta t. \quad (3.8)$$

The *implicit* or the *backward Euler method* uses a similar approach to approximate the time integral but instead of using the first point in the interval, it uses the last point [36]:

$$\phi^{n+1} = \phi^n + f(t_{n+1}, \phi^{n+1}) \Delta t. \quad (3.9)$$

Since the second method requires the knowledge of $\phi(t)$ at an unknown point in time, the integral cannot be calculated directly. Hence the name implicit [36]. Reformulating Eq.(3.9) allows it to be understood intuitively as an approximation of the time derivative of ϕ for a short interval of time, Δt :

$$\frac{\phi^{n+1} - \phi^n}{\Delta t} = f(t_{n+1}, \phi^{n+1}). \quad (3.10)$$

According to Ferziger, the implicit Euler method is *unconditionally stable*, it produces bounded outputs for bounded inputs for any time point, provided that $\frac{\partial f(t, \phi)}{\partial \phi} < 0$ holds. It thus behaves well, even in highly non-linear problems, such as the EHL problem at hand [36]. These properties of the implicit Euler method make it a suitable choice for the discretization of the Reynolds equation.

3.1.1. Discretized Film Thickness Equation

Using the grid introduced in Fig.3.1 it is possible to discretize the film thickness equation, the equation that governs the gap height of the contact. Recalling the previously presented film thickness equation:

$$h(x_1, x_2, t) = h_0(t) + \frac{x_1^2}{2R_{x_1}} + \frac{x_2^2}{2R_{x_2}} + \delta(x_1, x_2, t) + S(x_1, x_2, t). \quad (2.15 \text{ revisited})$$

The terms on the right-hand side except the elastic deformation are calculated individually for each node in the finite volume grid. The micro-texture influence term, $S(x_1, x_2, t)$, is given and thus can be calculated at a specified time point and discrete coordinates for the whole domain. A detailed explanation of the function is to be found in section 4.1. For a discrete point in time, t_n , and for the coordinates of the considered center node, X_1 and X_2 , this would result in²:

²The grid point coordinates are shown with capital letters here for shorthand notation since in these considerations only the center nodes are of interest, *i.e.* $X_1 = x_{1,C}$ and $X_2 = x_{2,C}$.

$$h(X_1, X_2, t_n) = h_0(t_n) + \frac{X_1^2}{2R_{x_1}} + \frac{X_2^2}{2R_{x_2}} + \delta(X_1, X_2, t_n) + S(X_1, X_2, t_n), \quad (3.11)$$

where all the terms except $\delta(X_1, X_2, t_n)$ can be conveniently calculated from the position of the node of interest and the given functions describing the contact geometry. The method for calculating the rigid body displacement term, $h_0(t_n)$, is briefly presented in section 3.2. For the calculation of the elastic deformation term, a different approach has to be taken to discretize the contacting solids.

The surface of the solid domain, approximated as an elastic half-space, is discretized using the boundary element formulation of Pohrt and Li [29] and the same grid introduced in Fig.3.1 is used. As it can be seen in Fig.3.3, it is divided into identical rectangles of size $h_x = \Delta x_1$ and $h_y = \Delta x_2$, which should not be confused with the gap height terms. The elastic deformation for such a configuration before discretization is shown in chapter 2 to be [4, 27, 29]:

$$\delta(x_1, x_2, t) = \frac{2}{\pi E'} \iint_A \frac{p(x'_1, x'_2, t)}{s} dx'_1 dx'_2. \quad (2.28 \text{ revisited})$$

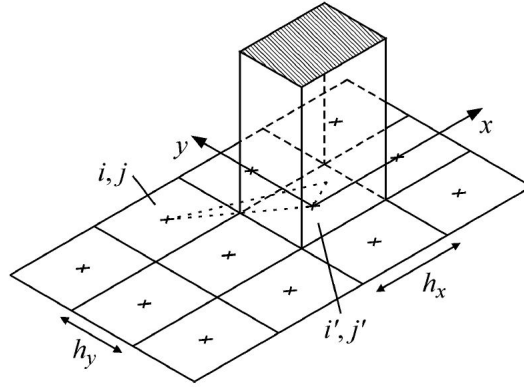


Figure 3.3.: Discretized elastic half-space with constant distributed load within each discrete element. x , y , h_x and h_y are equivalent to x_1 , x_2 , Δx_1 and Δx_2 respectively. Taken from Pohrt and Li [29].

The distributed normal load, which corresponds to the hydrodynamic pressure of the lubricant film, is taken to be constant within each rectangle, allowing the equation above to be discretized more conveniently. The discrete rectangles for which the elastic deformations are calculated are identified by the indices i and j respectively in x_1 - and x_2 -direction. The rectangle on which the considered constant distributed load is acting is denoted by the indices i' and j' . As shown by Pohrt and Li the discretization of the linear elasticity equation results in:

$$\delta^{ij} = \delta(X_1, X_2, t_n) = \sum_{i'} \sum_{j'} K^{ij i' j'} p^{i' j'}(t_n), \quad (3.12)$$

where the notation used in this thesis has been slightly adjusted to better fit the formulation of the cited paper [29]. The term $p^{i' j'}(t_n)$ denotes the assumed constant pressure for the rectangle (i', j') at time t_n . And δ^{ij} is used instead of $\delta(X_1, X_2, t_n)$ for shorthand notation for the elastic deformation in normal direction at the grid point (i, j) , with the positive

direction defined as deformation in to the plane. $K^{iji'j'}$ is the influence coefficient that determines the relative impact of the load at rectangle (i', j') on the elastic deformation at (i, j) and from the linear elasticity equation, Eq.(2.28), it is found to be:

$$K^{iji'j'} = \frac{2}{\pi E'} \int_{X_2 - \Delta x_2/2}^{X_2 + \Delta x_2/2} \int_{X_1 - \Delta x_1/2}^{X_1 + \Delta x_1/2} \frac{d\hat{X}_1 d\hat{X}_2}{\sqrt{(X_1 - \hat{X}_1)^2 + (X_2 - \hat{X}_2)^2}}, \quad (3.13)$$

where X_1' and X_2' correspond to the coordinates of the center of the element with pressure acting on it, and the variables with “ $\hat{\cdot}$ ” are introduced for correct integral notation [29]. The double summation signs in Eq.(3.12) correspond to superimposing the influences of all grid elements on the elastic deformation at the grid location indexed by (i, j) or located at the coordinates (X_1, X_2) . Eq.(3.13) on the other hand, corresponds to integrating $1/s$ found in non-discretized form of the linear elasticity equation along the area of the rectangle for which the influence factor is being calculated. The coefficients in front of the integral in the linear elasticity equation, Eq.(2.28), are included in the $K^{iji'j'}$ terms. Typically Eq.(3.13) can be expressed as a function of parameters: $K^{iji'j'} = K^{iji'j'}(i - i', j - j', \Delta x_1, \Delta x_2)$ [29]. Substituting the newly obtained expression for the discretization of the elastic deformation into Eq.(3.11) leads to the final form of the discretized film thickness equation:

$$h(X_1, X_2, t_n) = h_0(t_n) + \frac{X_1^2}{2R_{x_1}} + \frac{X_2^2}{2R_{x_2}} + \sum_{i'} \sum_{j'} K^{iji'j'} p^{i'j'}(t_n) + S(X_1, X_2, t_n). \quad (3.14)$$

As shown by Pohrt and Li [29], one advantage of this formulation is that Eq.(3.12) can be interpreted as a *two dimensional convolution* which corresponds to element-wise multiplication in Fourier space. The elements of the kernel, the matrix that is formed by considering Eq.(3.13) for each (i, j) in the grid, can be calculated as described by Pohrt and Li [29]. The usage of *fast Fourier transform* (FFT) and its inverse (FFT⁻¹) allows convenient and efficient calculation of the elastic deformation. In the provided steady EHL, it is ensured that a *linear convolution* is obtained. The exact procedure and the implementation is not within the scope of this thesis, therefore, the interested reader is referred to literature [29, 37] and the implementation of this procedure in the accompanying MATLAB scripts.

3.1.2. Discretized Reynolds Equation

The Reynolds equation with the implemented cavitation model, Eq.(2.62), is the equation to be discretized in this section. The Poiseuille, the Couette and the combined expansion and squeeze term are discretized using CDS, UDS and the Euler implicit method respectively. In the simulated configurations, only velocities in x_1 -direction are considered, causing only one Couette term to remain in the scalar equation. The discretization of the Poiseuille and Couette terms are based on the previous version of the solver which was implemented for steady operating conditions [19]. Reformulating the Reynolds equation and the cavitation conditions, Eqs.(2.62) and (2.63), for the chosen configurations:

$$\nabla \cdot \left(-\xi_p \nabla \bar{p} + \begin{pmatrix} \xi_u \\ 0 \end{pmatrix} (1 - \theta) \right) + \frac{\partial}{\partial t} (\xi_t (1 - \theta)) = 0, \quad (3.15)$$

$$\bar{p} \cdot \theta = 0 \quad \text{with} \quad \bar{p}, \theta \geq 0 \quad \text{and} \quad \bar{p} = p - p_{cav}. \quad (3.16)$$

where three new coefficients are introduced for shorthand notation in which $U_1 = \frac{u_{1,a} + u_{1,b}}{2}$ is the mean surface velocity of the two solid bodies in x_1 -direction:

$$\xi_p = \frac{h^3 \rho_l}{12\mu}, \quad (3.17)$$

$$\xi_u = U_1 \rho_l h, \quad (3.18)$$

$$\xi_t = \rho_l h. \quad (3.19)$$

For the implementation of the finite volume method, or rather the finite area method, Eq.(3.15) has to be integrated along the area of the control volume:

$$\iint_A \nabla \cdot \left(-\xi_p \nabla \bar{p} + \begin{pmatrix} \xi_u \\ 0 \end{pmatrix} (1 - \theta) \right) dx_1 dx_2 + \iint_A \frac{\partial}{\partial t} (\xi_t (1 - \theta)) dx_1 dx_2 = 0. \quad (3.20)$$

Using the *divergence theorem of Gauß* [38] the first area integral can be written as a line integral around the control volume boundary with the divergence operator omitted:

$$\iint_A \nabla \cdot \left(-\xi_p \nabla \bar{p} + \begin{pmatrix} \xi_u \\ 0 \end{pmatrix} (1 - \theta) \right) dx_1 dx_2 = \oint_{\partial A} \left(-\xi_p \nabla \bar{p} + \begin{pmatrix} \xi_u \\ 0 \end{pmatrix} (1 - \theta) \right) \cdot \vec{n} dL, \quad (3.21)$$

where ∂A denotes the control volume boundary composed of four lines, each corresponding to one main compass direction. “ $\cdot \vec{n}$ ” indicates the scalar product of the term in the brackets with the outward pointing normal vectors of respective surface boundaries. Thus, the equation becomes:

$$\oint_{\partial A} \underbrace{\left(-\xi_p \nabla \bar{p} + \begin{pmatrix} \xi_u \\ 0 \end{pmatrix} (1 - \theta) \right) \cdot \vec{n} dL}_{\text{CDS}} + \underbrace{\iint_A \frac{\partial}{\partial t} (\xi_t (1 - \theta)) dx_1 dx_2}_{\text{UDS, Euler implicit, constant over A}} = 0, \quad (3.22)$$

To approximate the resulting integrals in Eq.(3.22), the integrands are taken to be constant on the respective boundaries, the time dependent term is assumed to be constant across the whole area of the control volume and have the value as at the center node, allowing them to be taken out of the integrals. Expressed in scalar form this results in:

$$\begin{aligned} - \left(-\xi_p \frac{\partial \bar{p}}{\partial x_1} + \xi_u (1 - \theta) \right)_w \Delta x_2 + \left(-\xi_p \frac{\partial \bar{p}}{\partial x_1} + \xi_u (1 - \theta) \right)_e \Delta x_2 - \left(-\xi_p \frac{\partial \bar{p}}{\partial x_2} \right)_s \Delta x_1 \\ + \left(-\xi_p \frac{\partial \bar{p}}{\partial x_2} \right)_n \Delta x_1 + \left(\frac{\partial (\xi_t (1 - \theta))}{\partial t} \right)_C \Delta x_1 \Delta x_2 = 0, \quad (3.23) \end{aligned}$$

where the subscripts under the parentheses refer to the values calculated at the corresponding boundaries illustrated in Fig.3.1. The Couette terms in the north and south boundaries do not exist as the mean velocity in x_2 -direction is zero. Since the integrands within the line integrals are constant, the integrals correspond to the length of the boundary with the respective signs. The signs in front of the parentheses are determined by the orientation of the normal vectors of the surfaces, if the normal vector points in the positive coordinate direction the integral gets a positive sign, and vice versa. As the values of

these specific parameters and their gradients are known only at the computational nodes, interpolation is necessary. Based on the introduced interpolation methods in section 3.1 and assuming a positive mean velocity in x_1 -direction, the Poiseuille and Couette terms and their coefficients can be expressed in terms of node values as:

$$\xi_{u,w} = \xi_{u,W}, \quad \theta_w = \theta_W, \quad (\text{UDS}) \quad (3.24)$$

$$\xi_{u,e} = \xi_{u,C}, \quad \theta_e = \theta_C, \quad (\text{UDS}) \quad (3.25)$$

$$\xi_{p,w} = \frac{\xi_{p,C} + \xi_{p,W}}{2}, \quad \left(\frac{\partial \bar{p}}{\partial x_1} \right)_w = \frac{\bar{p}_C - \bar{p}_W}{\Delta x_1}, \quad (\text{CDS}) \quad (3.26)$$

$$\xi_{p,e} = \frac{\xi_{p,E} + \xi_{p,C}}{2}, \quad \left(\frac{\partial \bar{p}}{\partial x_1} \right)_e = \frac{\bar{p}_E - \bar{p}_C}{\Delta x_1}, \quad (\text{CDS}) \quad (3.27)$$

$$\xi_{p,s} = \frac{\xi_{p,C} + \xi_{p,S}}{2}, \quad \left(\frac{\partial \bar{p}}{\partial x_2} \right)_s = \frac{\bar{p}_C - \bar{p}_S}{\Delta x_2}, \quad (\text{CDS}) \quad (3.28)$$

$$\xi_{p,n} = \frac{\xi_{p,N} + \xi_{p,C}}{2}, \quad \left(\frac{\partial \bar{p}}{\partial x_2} \right)_n = \frac{\bar{p}_N - \bar{p}_C}{\Delta x_2}, \quad (\text{CDS}) \quad (3.29)$$

where it is important to recall that capital letters refer to the computational nodes while the lower-case letters indicate CV surfaces and all directions are relative to the current center node. The considerations of the Poiseuille terms and the Couette terms are adopted from the supplied steady EHL solver without alterations [19]. For the implementation of the Euler implicit method, one of the tasks of this thesis, the time point at which each of the values are computed must be specified and the equation must be reorganized to fit the form in Eq.(3.9). The first step in doing so is to substitute the pressure and the cavity fraction interpolations from Eqs.(3.24) to (3.29) into the discretized and integrated Reynolds equation, Eq.(3.23). Solving for the combined squeeze-expansion term after the substitution yields:

$$\begin{aligned} \left(\frac{\partial(\xi_t(1-\theta))}{\partial t} \right)_C \Delta x_1 \Delta x_2 = & -\xi_{p,w} \frac{\Delta x_2}{\Delta x_1} (\bar{p}_C - \bar{p}_W) + \xi_{u,w} \Delta x_2 (1 - \theta_W) \\ & + \xi_{p,e} \frac{\Delta x_2}{\Delta x_1} (\bar{p}_E - \bar{p}_C) - \xi_{u,e} \Delta x_2 (1 - \theta_C) \\ & - \xi_{p,s} \frac{\Delta x_1}{\Delta x_2} (\bar{p}_C - \bar{p}_S) + \xi_{p,u} \frac{\Delta x_1}{\Delta x_2} (\bar{p}_N - \bar{p}_C), \quad (3.30) \end{aligned}$$

where the right-hand side corresponds to $f(t, \phi(t))$ in Eq.(3.6), which the Euler implicit methodology requires it to be calculated at the next time point. Introducing the time point the variables are calculated at as superscripts, the following step is taken to transform the above equation into an equivalent expression of Eq.(3.9):

$$\begin{aligned} \frac{\xi_{t,C}^{n+1}(1-\theta_C^{n+1}) - \xi_{t,C}^n(1-\theta_C^n)}{\Delta t} = & \frac{1}{\Delta x_1 \Delta x_2} \left[-\xi_{p,w}^{n+1} \frac{\Delta x_2}{\Delta x_1} (\bar{p}_C^{n+1} - \bar{p}_W^{n+1}) + \xi_{u,w}^{n+1} \Delta x_2 (1 - \theta_W^{n+1}) \right. \\ & + \xi_{p,e}^{n+1} \frac{\Delta x_2}{\Delta x_1} (\bar{p}_E^{n+1} - \bar{p}_C^{n+1}) - \xi_{u,e}^{n+1} \Delta x_2 (1 - \theta_C^{n+1}) \\ & \left. - \xi_{p,s}^{n+1} \frac{\Delta x_1}{\Delta x_2} (\bar{p}_C^{n+1} - \bar{p}_S^{n+1}) + \xi_{p,n}^{n+1} \frac{\Delta x_1}{\Delta x_2} (\bar{p}_N^{n+1} - \bar{p}_C^{n+1}) \right], \quad (3.31) \end{aligned}$$

where now the right-hand side is $f(t_{n+1}, \phi^{n+1})$. The adopted notation is to show the point in space the variable is calculated at with subscripts. The superscripts indicate the point in time the variables are calculated at, which are not to be confused with exponents. For example, $\xi_{t,C}^{n+1}$ is the coefficient of the combined expansion-squeeze term, ξ_t , calculated at the center node C at time t_{n+1} . Reformulating the above equation to be written in terms of the relative pressures and the cavity fractions at the corresponding nodes results in:

$$\begin{aligned} & \left(\xi_{p,s} \frac{\Delta x_1}{\Delta x_2} \right) \bar{p}_S^{n+1} + \left(\xi_{p,w} \frac{\Delta x_2}{\Delta x_1} \right) \bar{p}_W^{n+1} - \left(\xi_{p,s} \frac{\Delta x_1}{\Delta x_2} + \xi_{p,w} \frac{\Delta x_2}{\Delta x_1} + \xi_{p,e} \frac{\Delta x_2}{\Delta x_1} + \xi_{p,n} \frac{\Delta x_1}{\Delta x_2} \right) \bar{p}_C^{n+1} \\ & \quad + \left(\xi_{p,e} \frac{\Delta x_2}{\Delta x_1} \right) \bar{p}_E^{n+1} + \left(\xi_{p,n} \frac{\Delta x_1}{\Delta x_2} \right) \bar{p}_N^{n+1} - (\xi_{u,w} \Delta x_2) \theta_W^{n+1} \\ & \quad + \left(\xi_{u,e} \Delta x_2 + \xi_{t,C} \frac{\Delta x_1 \Delta x_2}{\Delta t} \right) \theta_C^{n+1} + \xi_{u,w} \Delta x_2 - \xi_{u,e} \Delta x_2 - \xi_{t,C} \frac{\Delta x_1 \Delta x_2}{\Delta t} \\ & \quad + (\xi_{t,C}^n - \xi_{t,C}^n \theta_C^n) \frac{\Delta x_1 \Delta x_2}{\Delta t} = 0, \quad (3.32) \end{aligned}$$

where the superscript $n + 1$ has been omitted from the coefficients of the relative pressure and cavity fraction terms to avoid overcrowding. Eq.(3.32) forms the basis of the discretized form of the Reynolds equation which is to be solved by the algorithm presented in the next section. This equation is written for all of the nodes not lying on the domain boundaries and combined with the boundary conditions to form a system of algebraic equations consisting of N^2 equations called \vec{G} . All of the coefficients except the ones with the superscript n are unknown and should be calculated alongside \bar{p} and θ for the next, unknown time point, t_{n+1} .

3.2. Overview of the Algorithm

In this section, the methodology of solving the discretized equations presented previously is outlined. Firstly, the algorithm to solve the Reynolds equation coupled with the complementarity constraints is explained and then the overall structure of the solver is described. For seeing the exact implementation of the algorithm, the interested reader is encouraged to examine the detailed flowcharts in Appendix A and the corresponding MATLAB scripts.

Fischer-Burmeister-Newton-Schur (FBNS) Algorithm

Before considering the overall solution strategy, the FBNS algorithm used to solve the system of equations created by the discretized Reynolds equation is presented. This algorithm to solve the complementarity based formulation of the cavitation phenomena is developed by Woloszynski *et al.* and is shown to be significantly more efficient than other approaches [18].

When Eq.(3.32) is computed for each non-boundary node within the domain and combined with the boundary conditions, it results in a system of N^2 algebraic equations for the N -by- N grid at hand³. This system of equations can be expressed as: $\vec{G} = \vec{G}(\vec{p}, \vec{\theta}) = \vec{0}$ where \vec{p} and $\vec{\theta}$ are N^2 -element column vectors, each row corresponding to the relative pressure, $\bar{p} = p - p_{cav}$, and the cavity fraction of one node respectively at time t_{n+1} . The superscripts for the time point that is being solved for, $n + 1$, is omitted in the following for shorthand notation. Thus, each element of \vec{G} is either Eq.(3.32) computed at one inner node or an

³Woloszynski *et al.* [18] use N as the total amount of grid points. Different notation is used in this thesis to stay consistent with the rest of the document.

expression equivalent to the specified boundary conditions for a boundary (or outer node) [18]. Reformulated in vector notation, this results in:

$$\vec{G}(\vec{p}, \vec{\theta}) = \mathbf{A}_p \vec{p} + \mathbf{B} \vec{\theta} + \vec{c}_G = \vec{0}, \quad (3.33)$$

where \mathbf{A}_p and \mathbf{B} are the corresponding N^2 -by- N^2 coefficient matrices for the pressure and cavity fraction terms in Eq.(3.32). The vector \vec{c}_G contains all of the known values for the current node and the current time point, t_n , as well as the \bar{p} and θ independent terms. For one row of \vec{c}_G , these are the last four terms on the left-hand side of Eq.(3.32). Furthermore, the complementarity constraints can be expressed in vectorial form for this system of equations as: $\vec{p}^T \vec{\theta} = 0$ and $\vec{p}, \vec{\theta} \geq 0$ [18, 15].

Woloszynski *et al.* propose a two-step approach. The first step is to replace the complementarity constraints by an equivalent system of equations the same size as \vec{G} defined as $\vec{F} = \vec{F}(\vec{p}, \vec{\theta}) = \vec{0}$. This newly defined system of equations consist of N^2 *Fischer-Burmeister* equations (FB) given by:

$$F_j = F_j(\bar{p}_j, \theta_j) = \bar{p}_j + \theta_j - \sqrt{\bar{p}_j^2 + \theta_j^2} = 0 \quad \text{with } j = 1, \dots, N^2, \quad (3.34)$$

where \bar{p}_j and θ_j correspond to the j^{th} element of the respective relative pressure and cavity fraction vectors. Woloszynski *et al.* show in detail the equivalence of the two formulations of the complementarity constraint. The resulting system from combining \vec{F} and \vec{G} is now unconstrained and has $2N^2$ equations in total [18].

The second step in the FBNS algorithm is to solve the obtained unconstrained system of equations. Woloszynski *et al.* argue that the resulting system is continuously differentiable at except $\bar{p}_j = \theta_j = 0$ so the Newton method can be followed to iteratively solve it. The authors of the cited paper recommend to set \bar{p}_j or θ_j as a small positive number, such as the machine epsilon $\approx 2.22 \cdot 10^{-16}$, to avoid the method breaking down without compromising accuracy if they are found to be zero. The iterative scheme proposed by the Newton-Raphson method would be:

$$\vec{p}^{(k+1)} = \vec{p}^{(k)} + \tilde{\alpha} \cdot \delta \vec{p}^{(k)} \quad \text{and} \quad \vec{\theta}^{(k+1)} = \vec{\theta}^{(k)} + \tilde{\alpha} \cdot \delta \vec{\theta}^{(k)}, \quad (3.35)$$

where the superscripts above the vectors indicate the current step in the iteration process and the terms with δ are the solution updates for the respective variables and $\tilde{\alpha} < 1$ is the under-relaxation factor [18]. Details on this method can be found in Ferziger [36] as it is only briefly explained in the current work. It is important to realize that all the terms in the above equation are calculated for time t_{n+1} and the superscript $n+1$ is being omitted for this section.

The solution updates would be typically calculated by using the *Jacobian* matrices of the corresponding systems and solving the following:

$$\mathbf{J} \begin{bmatrix} \delta \vec{p}^{(k)} \\ \delta \vec{\theta}^{(k)} \end{bmatrix} = \begin{bmatrix} \mathbf{J}_{F,p} & \mathbf{J}_{F,\theta} \\ \mathbf{J}_{G,p} & \mathbf{J}_{G,\theta} \end{bmatrix} \begin{bmatrix} \delta \vec{p}^{(k)} \\ \delta \vec{\theta}^{(k)} \end{bmatrix} = - \begin{bmatrix} \vec{F} \\ \vec{G} \end{bmatrix} \quad \text{at } (\vec{p}^{(k)}, \vec{\theta}^{(k)}), \quad (3.36)$$

where \mathbf{J} is the Jacobian matrix of the whole system and its sub-matrices are denoted by $\mathbf{J}_{F,p} = \partial \vec{F} / \partial \vec{p}$, $\mathbf{J}_{F,\theta} = \partial \vec{F} / \partial \vec{\theta}$, $\mathbf{J}_{G,p} = \partial \vec{G} / \partial \vec{p}$ and so on. The terms written in bold indicate matrices [18]. The used notation for the derivative of a vector with respect to vector is illustrated with an example:

$$\mathbf{J}_{G,p} = \frac{\partial \vec{G}}{\partial \vec{p}} = \begin{pmatrix} \frac{\partial G_1}{\partial p_1} & \frac{\partial G_1}{\partial p_2} & \cdots & \frac{\partial G_1}{\partial p_{N^2}} \\ \frac{\partial G_2}{\partial p_1} & \frac{\partial G_2}{\partial p_2} & \cdots & \frac{\partial G_2}{\partial p_{N^2}} \\ \vdots & \vdots & \ddots & \vdots \\ \frac{\partial G_{N^2}}{\partial p_1} & \frac{\partial G_{N^2}}{\partial p_2} & \cdots & \frac{\partial G_{N^2}}{\partial p_{N^2}} \end{pmatrix}. \quad (3.37)$$

Woloszynski *et al.* propose to rearrange the columns of the Jacobian, \mathbf{J} , to obtain a more preferable system to solve for the updates and then reverse reorder the result to obtain the solution for the updates required for the original system. They show clearly that this approach is faster and the system matrix to solve is better conditioned, *i.e.* a small change in the input results in a small change in the output, making the correct solution easier to find. For a complete explanation of this procedure and for the demonstration of the efficiency of this algorithm, the interested reader is referred to the 2015 paper by Woloszynski *et al.* [18].

Solution Strategy

Now, the overall scheme of the developed solver, the boundary conditions and the method for overcoming additional non-linearities are presented. The solver consists of four nested loops. The outermost loop goes through operating conditions which are distinguished from one another by varying upper and lower solid body velocities. The second loop is responsible for marching through time, and is hence called the time loop. The next loop is the secant algorithm loop to solve the load balance equation. It attempts to validate the resultant pressure generated within the contact by comparing it to the external imposed normal load and by iteratively adjusting h_0 , the rigid body displacement. For more information about the secant algorithm, the interested reader is referred to literature [39]. The last and the innermost loop is the iterative FBNS solver discussed in the previous section. Within this loop, the Reynolds equation is solved and the guess of the pressure field is passed on to the secant algorithm loop for validation. Once the load balance equation is solved with sufficient accuracy⁴ for the current time point, the time loop moves on to the next point in time. This process is illustrated in Fig.3.4, where the operating condition loop, the time loop, the secant algorithm loop for the load balance and the FBNS loop is denoted by **(I)**, **(II)**, **(III)** and **(IV)** respectively. For a more detailed flow chart of the solver please see the Appendix A and the implementation of the MATLAB scripts.

In the first iteration of the time loop, *i.e.* in the first time point, the micro-texture is not introduced into the contact so the problem is identical to the steady case. This means that the algorithm can be used for both steady and unsteady configurations. For the steady case, the time loop would be exited after the first iteration. The steady solution is based on the algorithm developed by Hansen as this thesis focuses on extending his implementation and is supervised by him [19]. The micro-texture is introduced in the immediately following next time point at a prescribed x_1 -coordinate and is moved accordingly as time progresses. The first guess for the cavity fraction across the whole domain is assumed to be 0, meaning that there is no cavitation initially. In the first time point, the first guess of the pressure field passed on to the FBNS algorithm is the solution of the dry contact problem of the considered solid bodies, calculated by the algorithm published by Hansen⁵. For the following time points, the cavity fraction and the pressure fields from the immediately preceding time point are taken as first guesses.

⁴The thresholds are provided in the setup and thus discussed in chapter 4.1

⁵Which can be found in: "https://github.com/ErikHansenGit/Contact_elastic_half-space"

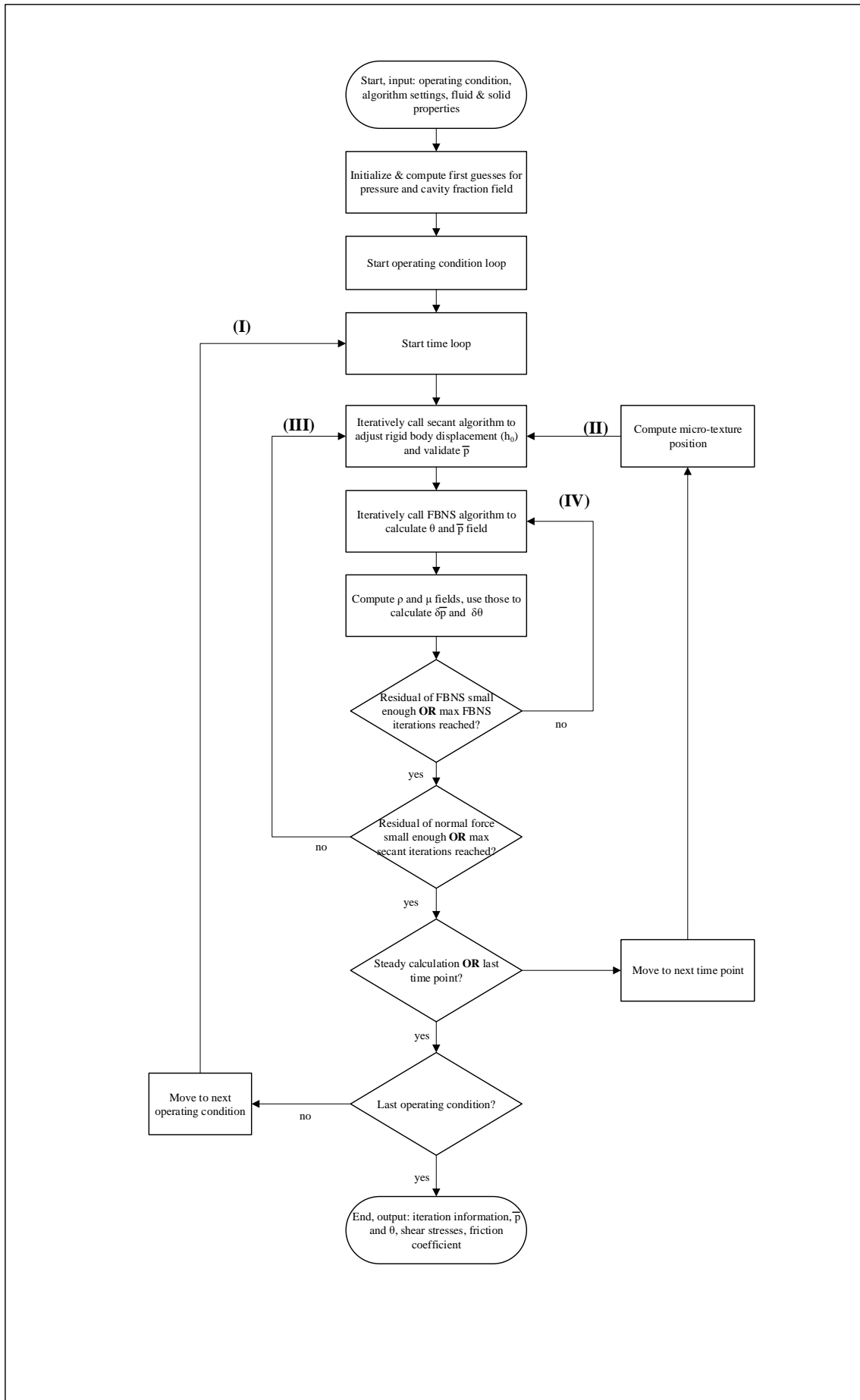


Figure 3.4.: Simplified flow chart of the developed solver, the loops are denoted via Roman numerals.

Boundary conditions for the cavity fraction and the relative pressure, $\vec{\theta}$ and \vec{p} , are implemented into the corresponding coefficient matrices and parts of the Jacobian. Typically, two types of boundary conditions are used in literature, *Dirichlet type* or *Neumann type*, which mean that respectively either the variable is set to a certain value or the gradient of the variable is predetermined at the domain boundaries [36]. For the cavity fraction, the boundary condition is of Dirichlet type and for every node lying on the west boundary the cavity fraction is set to be zero, *i.e.* $\theta_j = 0$ holds, where j is the linear index of west boundary elements. For the remaining boundaries, Neumann type boundary conditions are used and the gradient of the cavity fraction is set to zero for the boundary nodes. As for the relative pressure, all boundary conditions are of Dirichlet type and it is set equal to zero as well, meaning that for the domain boundaries, $\bar{p} = p - p_{cav} \approx p - p_0 = 0$ holds⁶.

The coefficients in Eq.(3.32) include the density and the viscosity of the lubricant as well as the gap height, h , all of which are dependent on pressure and are supposed to be calculated at t_{n+1} . If one substitutes the pressure dependencies of these coefficients and simultaneously attempts to solve them, the system would be highly non-linear. To avoid this, two measures are taken. Firstly, as illustrated in Fig.3.4, the lubricant properties ρ_l and μ are calculated from the relative pressure guess at the current iteration step of the FBNS algorithm using the known constitutive relations. This eliminates the non-linearities that would be introduced if the density and viscosity of the lubricant were simultaneously solved for alongside the Reynolds equation. The second measure to avoid additional non-linearities requires more in depth explanation and is better understood after investigation of the Jacobian matrix.

If one considers the lower half of the Jacobian in Eq.(3.36) multiplied with the update vector, *i.e.* the equation:

$$[\mathbf{J}_{G,p} \quad \mathbf{J}_{G,\theta}] \begin{bmatrix} \delta \vec{p}^{(k)} \\ \delta \vec{\theta}^{(k)} \end{bmatrix} = -\vec{G}(\vec{p}^{(k)}, \vec{\theta}^{(k)}), \quad (3.38)$$

where the right-hand side is known in vectorial form from Eq.(3.33) and in element-wise form from Eq.(3.32) as it is calculated for the iteration step (k). It is important to remark that the multiplication on the left-hand side is the matrix multiplication of a N^2 -by- $2N^2$ matrix and a $2N^2$ -by-1 vector, so the dimensions are consistent. If one row of the expression on the left-hand side is considered in a similar scalar formulation to Eq.(3.32), the following expression is obtained for an arbitrary inner node:

$$\begin{aligned} & \left(\xi_{p,s} \frac{\Delta x_1}{\Delta x_2} \right) \delta \bar{p}_S^{n+1} + \left(\xi_{p,w} \frac{\Delta x_2}{\Delta x_1} \right) \delta \bar{p}_W^{n+1} - \left(\xi_{p,s} \frac{\Delta x_1}{\Delta x_2} + \xi_{p,w} \frac{\Delta x_2}{\Delta x_1} + \xi_{p,e} \frac{\Delta x_2}{\Delta x_1} + \xi_{p,n} \frac{\Delta x_1}{\Delta x_2} \right) \delta \bar{p}_C^{n+1} \\ & + \left(\xi_{p,e} \frac{\Delta x_2}{\Delta x_1} \right) \delta \bar{p}_E^{n+1} + \left(\xi_{p,n} \frac{\Delta x_1}{\Delta x_2} \right) \delta \bar{p}_N^{n+1} - (\xi_{u,w} \Delta x_2) \delta \theta_W^{n+1} \\ & + \left(\xi_{u,e} \Delta x_2 + \xi_{t,C} \frac{\Delta x_1 \Delta x_2}{\Delta t} \right) \delta \theta_C^{n+1} + \underbrace{\xi'_{u,w} \Delta x_2 - \xi'_{u,e} \Delta x_2 - \xi'_{t,C} \frac{\Delta x_1 \Delta x_2}{\Delta t}}_{(\star), \text{ introduce } p \text{ dependence of } h} = -G, \quad (3.39) \end{aligned}$$

where in the left-hand side the terms from the previous time point indicated by the superscript n have vanished because of the differentiation operations in the Jacobian, as they are constant for t_{n+1} , and the right-hand side is the negative of Eq.(3.32) calculated for the relative pressure and cavity fraction of the iteration step (k) and is called the residual.

⁶As mentioned previously, the pressure when the liquid cavitates, p_{cav} , as well as the ambient pressure, p_0 , are small compared to the hydrodynamic pressure, p , allowing the approximation $p_{cav} = p_0$ [33]

The superscript (k) has been omitted from the update terms on the left-hand side as well as the residual on the right-hand side for concise notation. The approach suggested by Hansen [19] is to introduce the pressure dependence of the gap height terms due to the elastic deformation into the Jacobian and then simplify the problem to make it computationally feasible. The new coefficients $\xi'_{u,e}$, $\xi'_{u,w}$ and $\xi'_{t,C}$ in Eq.(3.39) marked by (\star) are introduced for this purpose. During the calculation of $\mathbf{J}_{G,p}$, only the coefficients multiplied by elements of \vec{p} are non-zero, because the partial derivatives of all other terms with respect to \bar{p} are zero. Recalling the definitions of the relevant coefficients:

$$\xi_u = U_1 \rho_l h, \quad (3.18 \text{ revisited})$$

$$\xi_t = \rho_l h, \quad (3.19 \text{ revisited})$$

where the h is to be replaced by the expression that was obtained for the discretized film thickness equation, Eq.(3.14). As only the elastic deformation term within that equation has pressure terms, it is the only non-zero term in the expression for $\mathbf{J}_{G,p}$. Simply inserting the equation for the elastic deformation and using the influence factors (the kernel entries) from Eq.(3.12) is not computationally viable because the influence factors are calculated for all of the grid points. This means that for a chosen center node C , the pressure at every other node in the domain has to be considered, resulting in a non-sparse system matrix, *i.e.* the system matrix is mostly filled with non-zero values and computationally expensive to solve. For the steady case, Hansen suggests to separate $\mathbf{J}_{G,p}$ into two parts \mathbf{A}_p and \mathbf{A}_h , where the former is the same as in Eq.(3.33) and the latter includes the pressure coefficients that arise from the substitution of h . The methodology implemented by Hansen is to only consider the *five main diagonals* of \mathbf{A}_h to reduce computational effort without compromising accuracy. This approach corresponds to only taking into account the elastic deformation caused by the pressures at the nodes: C , N , E , S and W when substituting h into the Reynolds equation to calculate the Jacobian [19]. This approach has been extended in this thesis to include the coefficient of the expansion-squeeze term by separating the corresponding part of the Jacobian further into \mathbf{A}_{time} . Expressed in equations:

$$\mathbf{J}_{G,p} = \mathbf{A}_p + \mathbf{A}_h + \mathbf{A}_{time}. \quad (3.40)$$

Next, the terms marked by (\star) in Eq.(3.39) with the elastic deformation term substituted with only the five main diagonals of both \mathbf{A}_h and \mathbf{A}_{time} are rewritten in scalar form to fit the notation in Eq.(3.39). With the additional definition of two coefficients as:

$$\xi_{u,h} = U_1 \rho_l, \quad (3.41)$$

$$\xi_{t,h} = \rho_l, \quad (3.42)$$

to denote the coefficients of h after it has been substituted in the (\star) terms⁷ in Eq.(3.39), the results can be expressed in terms of the kernel entries as:

⁷Special attention should be paid to remark that the h is a subscript in these two new definitions.

$$\xi'_{u,w} \Delta x_2 = (\xi_{u,h} \cdot h)_w \Delta x_2 = (\xi_{u,h})_w \Delta x_2 (K_{NW} \delta \bar{p}_S^{n+1} + K_C \delta \bar{p}_W^{n+1} + K_W \delta \bar{p}_C^{n+1} + K_{WW} \delta \bar{p}_E^{n+1} + K_{SW} \delta \bar{p}_N^{n+1}), \quad (3.43)$$

$$-\xi'_{u,e} \Delta x_2 = -(\xi_{u,h} \cdot h)_e \Delta x_2 = -(\xi_{u,h})_e \Delta x_2 (K_N \delta \bar{p}_S^{n+1} + K_E \delta \bar{p}_W^{n+1} + K_C \delta \bar{p}_C^{n+1} + K_W \delta \bar{p}_E^{n+1} + K_S \delta \bar{p}_N^{n+1}), \quad (3.44)$$

$$-\xi'_{t,C} \frac{\Delta x_1 \Delta x_2}{\Delta t} = -(\xi_{t,h} \cdot h)_C \frac{\Delta x_1 \Delta x_2}{\Delta t} = -(\xi_{t,h})_C \frac{\Delta x_1 \Delta x_2}{\Delta t} (K_N \delta \bar{p}_S^{n+1} + K_E \delta \bar{p}_W^{n+1} + K_C \delta \bar{p}_C^{n+1} + K_W \delta \bar{p}_E^{n+1} + K_S \delta \bar{p}_N^{n+1}), \quad (3.45)$$

where the K terms with their subscripts refer to the corresponding kernel entries and the interpolation methods used for the coefficients $\xi_{u,h}$ and $\xi_{t,h}$ are identical to their respective counterparts, *i.e.* $(\xi_{u,h})_w = (\xi_{u,h})_W$ and $(\xi_{u,h})_e = (\xi_{u,h})_C$. This means that the terms in the parentheses on the right-hand sides of Eqs.(3.43) to (3.45) correspond to approximations of the elastic deformations on the W , C and C cells, respectively. The kernel entries can be calculated by Eq.(3.13).

If one considers the kernel similar to grid overlapping the computational node grid presented in Fig.3.1, the result of the convolution can be thought of visually. The matching of the kernel entries to the nodes on the FV grid are obtained by placing the center of the kernel, K_C , where the elastic deformation is being calculated at, given by the subscript of h . Then the kernel entries are mirrored, as by definition of convolution, and then the overlapping kernel entries are multiplied with the relative pressure values at the corresponding nodes. This procedure is visualized in Fig.3.5 for calculating $h_w = h_W$ in Eq.(3.43), where only the relative pressures at the four compass directions and the center cell in the FV grid are of relevance for the Jacobian.

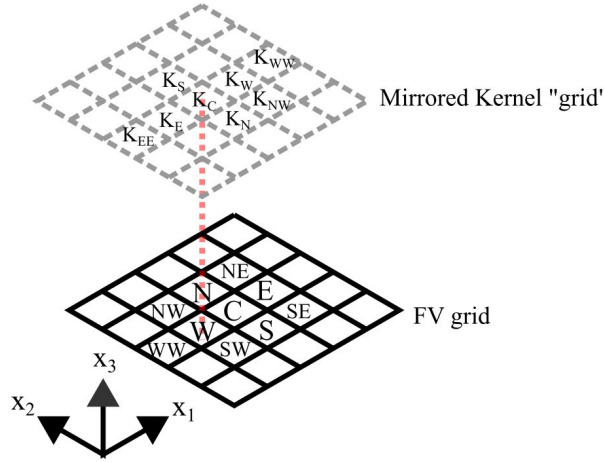


Figure 3.5.: An illustration for calculating h_w , the central kernel entry, K_C , is aligned with the west cell of the FV grid. The kernel is mirrored due to the convolution. The relative pressures at C and directly neighbouring cells in the FV grid are of interest.

As the cavity fraction has no influence on any of its coefficients, $\mathbf{J}_{G,\theta} = \mathbf{B}$ holds. The substitution of Eqs.(3.43) to (3.45) into Eq.(3.39) would give one row of the equations of the whole system the developed algorithm solves to obtain the update terms:

$$J_{G,p,S}\delta\bar{p}_S^{n+1} + J_{G,p,W}\delta\bar{p}_W^{n+1} + J_{G,p,C}\delta\bar{p}_C^{n+1} + J_{G,p,E}\delta\bar{p}_E^{n+1} \\ + J_{G,p,N}\delta\bar{p}_N^{n+1} + J_{G,\theta,W}\delta\theta_W^{n+1} + J_{G,\theta,C}\delta\theta_C^{n+1} = -G, \quad (3.46)$$

where the entries of the Jacobians are the corresponding coefficients of the update terms, $\delta\bar{p}^{(k)}$ and $\delta\theta^{(k)}$, for the respective cells. The right-hand side is the same as Eq.(3.39). This equation is in fact one row of the system of equations introduced in Eq.(3.38). The expressions for the pressure update coefficients in the above equation are as follows:

$$J_{G,p,S} = \xi_{p,s} \frac{\Delta x_1}{\Delta x_2} + (\xi_{u,h})_w \Delta x_2 K_{NW} - (\xi_{u,h})_e \Delta x_2 K_N - (\xi_{t,h})_C \frac{\Delta x_1 \Delta x_2}{\Delta t} K_N, \quad (3.47)$$

$$J_{G,p,W} = \xi_{p,w} \frac{\Delta x_2}{\Delta x_1} + (\xi_{u,h})_w \Delta x_2 K_C - (\xi_{u,h})_e \Delta x_2 K_E - (\xi_{t,h})_C \frac{\Delta x_1 \Delta x_2}{\Delta t} K_E, \quad (3.48)$$

$$J_{G,p,C} = - \left(\xi_{p,s} \frac{\Delta x_1}{\Delta x_2} + \xi_{p,w} \frac{\Delta x_2}{\Delta x_1} + \xi_{p,e} \frac{\Delta x_2}{\Delta x_1} + \xi_{p,n} \frac{\Delta x_1}{\Delta x_2} \right) + (\xi_{u,h})_w \Delta x_2 K_W \\ - (\xi_{u,h})_e \Delta x_2 K_C - (\xi_{t,h})_C \frac{\Delta x_1 \Delta x_2}{\Delta t} K_C, \quad (3.49)$$

$$J_{G,p,E} = \xi_{p,e} \frac{\Delta x_2}{\Delta x_1} + (\xi_{u,h})_w \Delta x_2 K_{WW} - (\xi_{u,h})_e \Delta x_2 K_W - (\xi_{t,h})_C \frac{\Delta x_1 \Delta x_2}{\Delta t} K_W, \quad (3.50)$$

$$J_{G,p,N} = \underbrace{\xi_{p,n} \frac{\Delta x_1}{\Delta x_2}}_{\text{terms of } \mathbf{A}_p} + \underbrace{(\xi_{u,h})_w \Delta x_2 K_{SW} - (\xi_{u,h})_e \Delta x_2 K_S}_{\text{terms of } \mathbf{A}_h} - \underbrace{(\xi_{t,h})_C \frac{\Delta x_1 \Delta x_2}{\Delta t} K_S}_{\text{terms of } \mathbf{A}_{\text{time}}}, \quad (3.51)$$

where on the right-hand side, the first terms⁸ correspond to entries of \mathbf{A}_p , the second and third terms are the entries of \mathbf{A}_h and the last terms are the corresponding elements of \mathbf{A}_{time} , as illustrated in the last equation. The coefficients of the cavity fraction updates for the (k^{th}) iteration do not change due to the substitution of the pressure dependency of h :

$$J_{G,\theta,W} = -\xi_{u,w} \Delta x_2, \quad (3.52)$$

$$J_{G,\theta,C} = \xi_{u,e} \Delta x_2 + \xi_{t,C} \frac{\Delta x_1 \Delta x_2}{\Delta t}. \quad (3.53)$$

The precise implementation of this concept for the system of equations in matrix form can be seen in the accompanying MATLAB script and is carried out by calculating the diagonals of the corresponding matrices as they are sparse.

This chapter and the previous one provide a complete overview of the used model to describe the EHL problem at hand, the methodology used to discretize equations and the implemented algorithms to solve them. What remains now is to validate the solver with experimental data from literature and investigate its dependency on grid and time resolution.

⁸For Eq.(3.49) the expressions in the parentheses in the right-hand side are considered a single term.

4. Model Validation & Analysis

This chapter focuses on presenting the results of the carried out simulations to validate the model and the parameters used to run them. Results of further simulations to analyse the behaviour of the solver are also shown and discussed.

Firstly, the replicated experimental setup of Mourier *et al.* [21] is detailed and the used micro-texture profile is explained. The required solid parameters, lubricant parameters and operating conditions are specified. Then, the input parameters for the algorithm are indicated and further explained. For validation, the calculated gap height distributions are compared to the measured values of Mourier *et al.* [21] for two configurations and at five different points in time. The two configurations differ from one another in the geometry parameters of the micro-texture and they have different values for the *slide-to-roll ratio* (SSR) defined by:

$$\Sigma = \frac{u_a - u_b}{u_a + u_b} \quad (4.1)$$

where similarly to previous chapters, the subscript a is used for the lower body (the steel ball) and b corresponds to the upper body (disc). As the ball and the disc are assumed to have velocities in only x_1 -direction a second subscript is not necessary. The two different configurations are described in detail in the following [21]. The three carried out studies are detailed and an overview of all investigated simulations is presented. Then, the results of the grid refinement and temporal resolution refinement studies are considered. Finally an overall evaluation of the developed model and the investigations on it is made.

4.1. Setup & Overview

This section provides an overview of the simulated tribometer used by Mourier *et al.*, the various parameters for the algorithm and the carried out simulations alongside the studies they belong to.

Replicated Experimental Setup

The ball-on-disc tribometer used by Mourier *et al.* in their 2006 paper is described in Fig.4.1. The normal load is imposed on the ball and the stepping motors control the velocities of the disk as well as the ball. The torque sensor under the disk is used to measure

the friction torque to calculate the friction force. The heating system in combination with the pyrometer, a device to measure temperature without contact, enable the contact temperature to be measured and moderated [21].

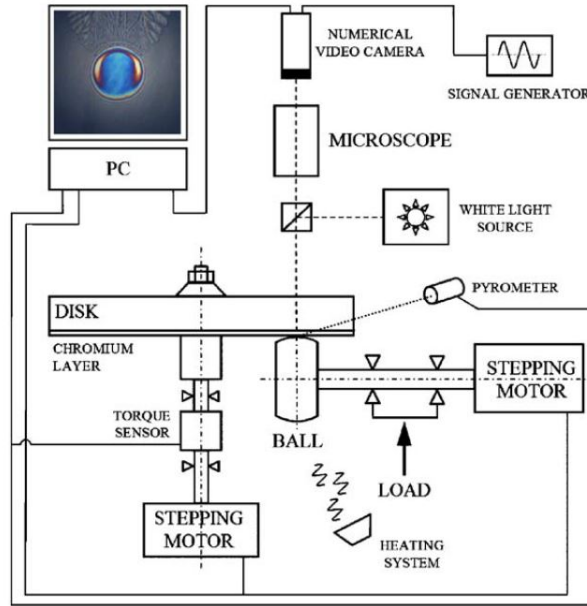


Figure 4.1.: The EHL tribometer used by Mourier *et al.* with their measurement setup. Taken from [21].

The EHL contact is realized between a silica disk coated with a chromium layer for optical measurement purposes and a 52 100 steel ball¹. As the considered geometry is assumed to be a spherical ball, $R = R_{x_1} = R_{x_2}$ holds in Eq.(2.15) [21]. It is important to realize that the gap height distribution created by the ball profile is actually the negative of the profile. If the ball profile rises, the distance between the ball and the disc decreases, meaning that the gap height also decreases.

The micro-texture is obtained using *laser surface texturing* (LST) and is placed on the ball surface. The micro-texture influence on the gap height is modelled in the simulations using the function [21]:

$$S(x_1, x_2, t) = d \cdot \cos\left(\frac{\pi}{2} \frac{s'}{1.2r}\right) \cdot \exp\left(-2 \left(\frac{s'}{1.2r}\right)^2\right), \quad (4.2)$$

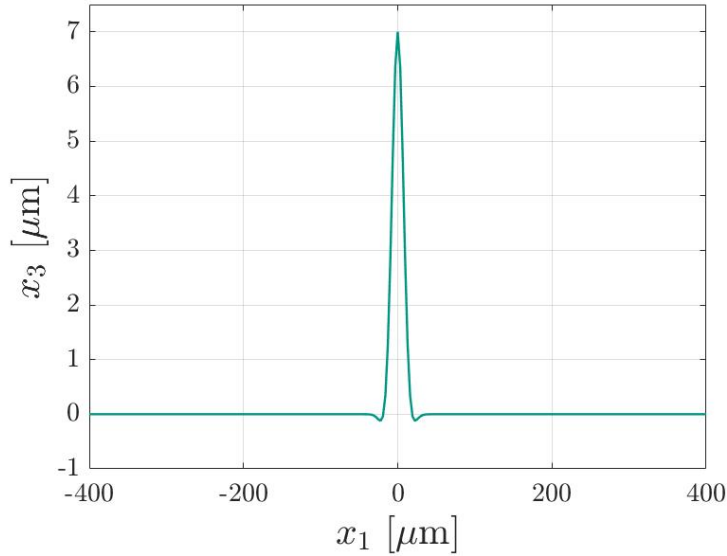
where d is the micro-texture depth, r is the micro-texture radius and s' denotes the distance of the micro-texture center, (\bar{x}_1, \bar{x}_2) , at a given time to the considered point in the simulation domain, written in mathematical terms: $s' = \sqrt{(x_1 - \bar{x}_1)^2 + (x_2 - \bar{x}_2)^2}$. The illustration of the micro-texture can be seen in Fig.4.2. The center coordinates of the micro-texture depend on the surface velocity of the ball and its starting position:

$$\begin{pmatrix} \bar{x}_1 \\ \bar{x}_2 \end{pmatrix} = \begin{pmatrix} \bar{x}_{1,0} \\ \bar{x}_{2,0} \end{pmatrix} + \begin{pmatrix} u_{1,a} \\ 0 \end{pmatrix} \cdot t, \quad (4.3)$$

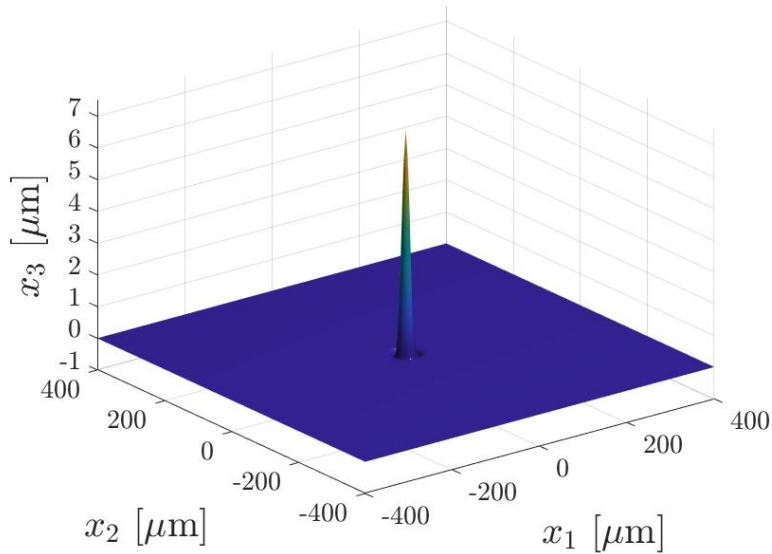
where t is the time and the coordinates with the additional subscript 0 specify the initial coordinates of the micro-texture center. This is how the time dependence of $S(x_1, x_2, t)$ is

¹This grade of steel is comparable to 100Cr6 in ISO standards, ISO 683-17:1999 [40]

introduced. Another important remark is the fact that the micro-texture profile is simply the negative of the illustrated surface, which is the gap height influence of the micro-texture shown as $S(x_1, x_2, t)$, similar to the ball profile and the gap height distribution due to it. The micro-texture is a cavity on the surface of the ball and as it passes through the contact, it locally increases the distance between the solid bodies, *i.e.* the gap height [21].



(a) Along a line in x_1 -direction with $x_2 = 0$



(b) In the x_1 - x_2 plane

Figure 4.2.: The micro-texture influence on the gap height for the given parametrization for configuration 1, shown as a profile on a line along constant $x_2 = 0$ and along the whole plane, both when $(\bar{x}_1, \bar{x}_2) = (0, 0)$.

Mourier *et al.* provide their results of two experimental configurations, which differ in the SSR and in the micro-texture depth and radius but have the same mean velocity, $U_1 = 0.09 \text{ ms}^{-1}$. The two configurations are illustrated in Table 4.1. A slide-to-roll ratio

of 0 corresponds to pure rolling as $u_a = u_b$ and a negative value for the SSR means that the lower body, the ball in this case, moves slower than the disc [21].

To be able to carry out the simulations, the geometry parameters, solid and lubricant properties and operating conditions have to be further specified. An overview of the values used by Mourier *et al.* is presented in Table 4.2. The first two parameters are already known from previous considerations. The Hertzian contact radius is denoted by a and used as a reference length for non-dimensionalization of the parameters provided in the aforementioned paper. The lubricant is a 400 *Neutral Solvent* base oil for which the cavitation pressure and the values to be used in the constitutive equations have to be indicated. p_{cav} is the cavitation pressure and is taken to be of the same magnitude as the ambient pressure. ρ_0 is the density of the liquid lubricant at ambient pressure, which is used in the Dowson-Higginson relation, Eq.(2.74). The value for this parameter is not provided by Mourier *et al.* so it is taken to be 850 kg/m^3 . The following three parameters are the coefficients used for the viscosity-pressure relation, given in Eqs(2.75), (2.76) and (2.77): μ_0 is the dynamic viscosity of the lubricant at ambient pressure, \tilde{p}_0 is the pressure coefficient and α is the pressure viscosity index [21]. The limiting shear stress denoted by τ_{max} , is the value used to limit the average Couette stress in the contact, as explained in the shear thinning model in section 2.3. The minimum macroscopic gap height, h_{min} , needs to be defined to avoid non-physical solutions for the EHL problem at hand. If the calculated gap height falls below this value at certain locations, the gap height at those nodes are set to this predefined value, meaning that solid bodies never contact one another. As for the operating conditions, p_0 is the ambient pressure and F_3 is the imposed vertical load [19].

Simulated configurations	SSR[-]	d [μm]	r [μm]	U_1 [ms^{-1}]	u_a [ms^{-1}]	u_b [ms^{-1}]
Configuration 1	0	7	15.5	0.09	0.09	0.09
Configuration 2	-0.5	1.3	21.5	0.09	0.045	0.135

Table 4.1.: Overview of configuration 1 and 2 as given by Mourier *et al.* The geometry parameter d is the micro-texture depth and r is the corresponding micro-texture radius. The lower and upper bodies velocities, respectively u_a and u_b , are calculated from the SSR and U_1 [21].

Geometry and solid parameters		
R	12.5	mm
E'	110	GPa
a	136.5	μm
Lubricant parameters		
p_{cav}	≈ 101325	Pa
ρ_0	850	kg/m^3
μ_0	0.25	Pa·s
\tilde{p}_0	$1.96 \cdot 10^8$	Pa
α	22	GPa^{-1}
τ_{max}	10	MPa
h_{min}	1	nm
Operating conditions		
F_3	15	N
p_0	101325	Pa

Table 4.2.: Table of geometry parameters, solid and lubricant properties and operating conditions as given by Mourier *et al.* [21].

Algorithm Settings

The lubrication gap is discretized using the finite volume grid introduced in chapter 3 using varying spatial resolutions. Mourier *et al.* use 257×257 grids for their own simulations, so for the validation of the model, the same resolution is used in this thesis [21]. The spatial grid resolution used for the further studies are summarized later as necessary. The domain is defined as a $819 \mu\text{m} \times 819 \mu\text{m}$ square with the origin placed in the middle [19]. The micro-texture moves along a line in x_1 -direction as the surfaces only have velocities in this direction. The starting coordinates of the micro-texture are set to $(\bar{x}_1, \bar{x}_2) = (-250 \mu\text{m}, 0 \mu\text{m})$ and it is introduced to the domain after the first time point, the steady case, is solved for. To know when to stop the time loop, (II) in Fig.3.4, a final x_1 -coordinate for the micro-texture center has to be specified additionally, this value is defined as $250 \mu\text{m}$.

Defining the values of the relative tolerances and the allowed maximum number of iterations for the secant and FBNS loops are also of importance to know when to exit the respective loops. For the initial guess of the pressure distribution the dry contact pressure algorithm² is used. The values of the required parameters for these three algorithms are presented in Table 4.3. The meaning of each parameter is described shortly in the following. A common relative tolerance is used throughout the algorithm, denoted by Δ_{gen} . For each of the calculated residuals, namely, for the normal force, relative pressure, cavity fraction and for the error in the contact pressure algorithm relative errors are calculated and compared to Δ_{gen} . To calculate relative errors, reference values are also specified, which are discussed in the following when necessary.

The maximum number of permitted iterations for the secant algorithm is determined with $i_{sec,max}$. As the algorithm needs two initial guesses for calculating the next guess, $h_{0,n-2}$ and $h_{0,n-1}$ are used, which are respectively the first and the second guesses for the rigid body displacement. Upper and lower limits for h_0 are defined as $h_{0,max}$ and $h_{0,min}$. Whenever the calculated value reaches the limits the secant algorithm is reset and the initial two guesses are adjusted accordingly. And h_δ is the value that separates the newly adjusted two initial guesses. Δ_p is the relative residual of the FBNS algorithm that has to be reached to evaluate the load balance equation³. The relative error for the secant algorithm is calculated using the ratio of the difference between the calculated and the imposed normal load to the imposed normal load.

As for the FBNS algorithm, similarly, the maximum number of iterations permitted before exiting the loop is indicated with $i_{p,max}$. For calculating the relative errors, the residuals for both \bar{p} and θ are calculated and divided by appropriate reference values. The former is divided by $p_{ref,p}$, which is the average pressure on the contact, *i.e.* the normal load divided by the area of the FV grid. The latter however, can only take values between 0 and 1, so a reference value is not needed to calculate the relative error associated with it, the residual itself is sufficient. The greater of these values is chosen as the FBNS relative error which is then compared to Δ_{gen} to decide if the secant algorithm should keep iterating. The relative error for the pressure guess from the FBNS algorithm is compared to Δ_p to decide whether a new guess for the rigid body displacement should be made by the secant algorithm. The under-relaxation factor, for Eq.(3.35), is determined empirically for different spatial resolutions and found to be sufficiently appropriate as 0.05 for lower spatial resolutions and 0.04 for higher grid resolutions. Exact specifications can be found at the end of this section.

²As mentioned before, this algorithm is taken from the repository by Hansen: "https://github.com/ErikHansenGit/Contact_elastic_half-space"

³The subscript p is used for shorthand notation and is associated with the FBNS algorithm as it calculates the pressure distribution.

For the contact pressure algorithm to calculate the initial pressure distribution guess, two input parameters are presented here without further explanation as it is not within the scope of this work. This segment of the solver has been developed by Hansen and the interested reader is referred to the previously mentioned repository for more information [19, 32]. Moreover, the time step size has to be specified to be able to proceed with transient computations. For this parameter, the values used for each simulation differ from one another. Thus, are presented as the corresponding simulations are discussed.

General		
Δ_{gen}	10^{-5}	[-]
Secant algorithm		
$i_{sec,max}$	30	[-]
$h_{0,n-2}$	-1	μm
$h_{0,n-1}$	-0.5	μm
$h_{0,max}$	0	μm
$h_{0,min}$	-2.5	μm
h_{δ}	0.1	μm
Δ_p	0.1	[-]
FBNS algorithm		
$i_{p,max}$	20	[-]
$p_{ref,p}$	$\frac{F_3}{A} = 21.02$	MPa
$\tilde{\alpha}$	{0.05, 0.04}	[-]
Dry contact pressure		
$i_{con,max}$	100	[-]
$h_{ref,con}$	0.01	μm

Table 4.3.: Summary of required parameters for the various algorithms and the values used. See text for explanations.

Overview of Simulations

In total, 11 simulations were investigated in detail under the scope of the validation of the model by comparison to experimental results and the two studies on the developed solver. All simulations were run on the computer “istmlynx2” of the Institut für Strömungsmechanik (ISTM) of Karlsruher Institut für Technologie (KIT). The relevant information of the computer can be read from Table 4.4.

The simulations are divided into three categories distinguished by letters:

- A: validation by experimental results from Mourier *et al.* [21],
- B: spatial resolution analysis,
- C: temporal resolution analysis for a spatial grid of 129×129 resolution.

Table 4.5 summarizes all simulations and relevant parameters. Computational times are presented alongside the simulations but are discussed in section 4.3. One important parameter is the ratio of the dimensionless time step size, ΔT to the dimensionless grid spacing, ΔX . The non-dimensionalization is carried out using the Hertzian contact radius a and the mean velocity of the surfaces U_1 . The same procedure as Mourier *et al.* is followed [21]:

$$\Delta X = \frac{\Delta x_1}{a} = \frac{\Delta x_2}{a}, \quad (4.4)$$

$$\Delta T = \frac{\Delta t \cdot U_1}{a}. \quad (4.5)$$

Information on the computer	
Computer name	istmlynx2
CPU model name	AMD Opteron(tm) Processor 6376
Total RAM	131995800 kB

Table 4.4.: Specifications of the computer used to run all simulations.

Sim. ID	Grid	$\frac{\Delta T}{\Delta X}$	Con.	$\tilde{\alpha}$	n_t	t_{tot} [h]	t_{max} [s]	t_{avg} [s]	ct_{max}
A.1	3 257-by-257	1	1	0.04	157	16.83	1460.6	388.45	16
A.2	9 257-by-257	1	2	0.04	313	22.88	1374.3	264	16
B.1	1 65-by-65	1	1	0.05	40	0.27	237	24.86	8
B.2	2 129-by-129	1	1	0.05	79	1.57	165	71.89	8
B.3	3 257-by-257	1	1	0.04	157	16.83	1460.6	388.45	16
B.4	11 65-by-65	1	2	0.05	79	0.30	47.12	13.59	8
B.5	8 129-by-129	1	2	0.04	157	2.81	205.37	64.64	8
B.6	9 257-by-257	1	2	0.04	313	22.88	1374.3	264	16
C.1	32 129-by-129	0.25	2	0.04	626	8.57	208.66	49.28	8
C.2	34 129-by-129	0.5	2	0.04	313	5.02	204.91	57.69	8
C.3	36 129-by-129	0.75	2	0.04	209	3.67	209.21	63.3	8
C.4	8 129-by-129	1	2	0.04	157	2.81	205.47	64.64	8
C.5	39 129-by-129	1.5	2	0.04	105	2.23	211.92	76.58	8

Table 4.5.: Overview of all carried out simulations and elapsed times for each simulation. “Sim.” stands for simulation and indicates the study the simulations belong to and their number. “ID” denotes the internally used identification number when simulations were being carried out. ΔT and ΔX are the dimensionless time step size and grid spacing respectively. “Con.” is the number of the configuration, corresponding to 1 for SSR=0 and 2 for SSR=-0.5. $\tilde{\alpha}$ is the under-relaxation factor used in the FBNS algorithm, n_t is the number of computed time points, t_{tot} is the total elapsed time for the simulation in hours, t_{max} is the elapsed time for the time point that took longest to compute in seconds, t_{avg} is the average computational time per time point in seconds. ct_{max} is the number of maximum computational threads allowed for the simulation.

Mourier *et al.* mention that for their simulations $\Delta T = \Delta X$ holds, meaning that as the spatial resolution is refined the temporal resolution is also refined accordingly, and vice versa [21]. In this thesis, the studies A and B follow the same approach. For study C, the ratio of the two dimensionless parameters is investigated, so $\Delta T = \Delta X$ is not necessarily true. The values of the dimensionless grid spacing corresponding to the different grid sizes used is presented in Table 4.6. As the main goal of this work is to develop and validate a model for simulating the pressure distribution in a ball-on-disc tribometer, the mentioned additional studies are briefly discussed to better understand the behaviour of the solver. The simulation ID's presented in Table 4.5 are used to identify specific simulations independent of the study they belong to and were internally used during the working procedure of this thesis. From now on, the simulations will be referred to with respect to their study identifiers.

	257×257	129×129	65×65
ΔX	0.0234375	0.0468750	0.0937500

Table 4.6.: Dimensionless grid spacings, ΔX , for different spatial resolutions.

4.2. Validation of the Model

To validate the model, the two previously discussed configurations are simulated, each corresponding to one experiment Mourier *et al.* have provided [21]. The gap height distribution of five different time points are compared with the experimental measurements. Firstly, the results of the simulations and the experiments are presented together. Additionally, the theoretical pressure distributions are shown. Then, the validity of the model is discussed.

Results & Comparison to Experiments

For the case with pure rolling, *i.e.* zero slide-to-roll ratio, the gap height distributions for each time point corresponding to five x_1 -coordinates of the micro-texture center are illustrated in Fig.4.3. The x_1 -coordinates are approximate values and do not exactly match for the simulation and the measurements due to measurement inaccuracies. The calculated hydrodynamic pressure distributions are displayed along a line $x_2 = 0$ in Fig.4.3 (top) and across the whole domain in Fig.4.5. No experimental data was found to compare the pressure values. Nonetheless, knowledge of the pressure distribution, especially the pressure peaks observed around the micro-texture provide interesting insights.

As for the second configuration, where the slide-to-roll ratio is given to be -0.5 and the micro-texture is wider and shallower as indicated by Mourier *et al.*, the calculated results using the introduced EHL solver and the measured values of the gap height distribution are displayed in Fig.4.4. The pressure distributions along $x_2 = 0$ are also shown in Fig.4.4 (top). Fig.4.6 illustrates the pressure distribution along the whole domain as a surface.

Discussion

If one compares the top and bottom graphs for configuration 1 in Fig.4.3, a high degree of similarity between them can be observed. The biggest differences occur when the micro-texture is entering and leaving the contact, in (b) and (e). The predicted gap height decreases right in front and right after the micro-texture and are more severe compared to the measured values. These locations are also associated with extreme pressure spikes, up to 1.2 GPa, as depicted in Fig.4.3 (top). Additionally, the maximum hydrodynamic pressures across the whole field for both configurations is plotted against time in Fig.4.7.

Stahl and Jacobson show that the Dowson-Higginson relation, the used compressibility model in this work, is in good agreement with experimental results up to 400 MPa [16, 41]. As the maximum pressures in the contact reach above 1.2 GPa for configuration 1, it is hypothesized that this might be a reason behind the discrepancies between the simulations carried out here and the experimental measurements of Mourier *et al.* [21].

As for configuration 2, the passing of the micro-texture creates less extreme pressure spikes. Interestingly, the largest differences between predictions and measurements are when the micro-texture is in the middle of the contact, (c) and (d) in Fig.4.4, the opposite of the observations for configuration 1. For configuration 2, the maximum hydrodynamic pressure across the whole contact approximately reach half of the values observed for configuration 1, as illustrated in Fig.4.7.

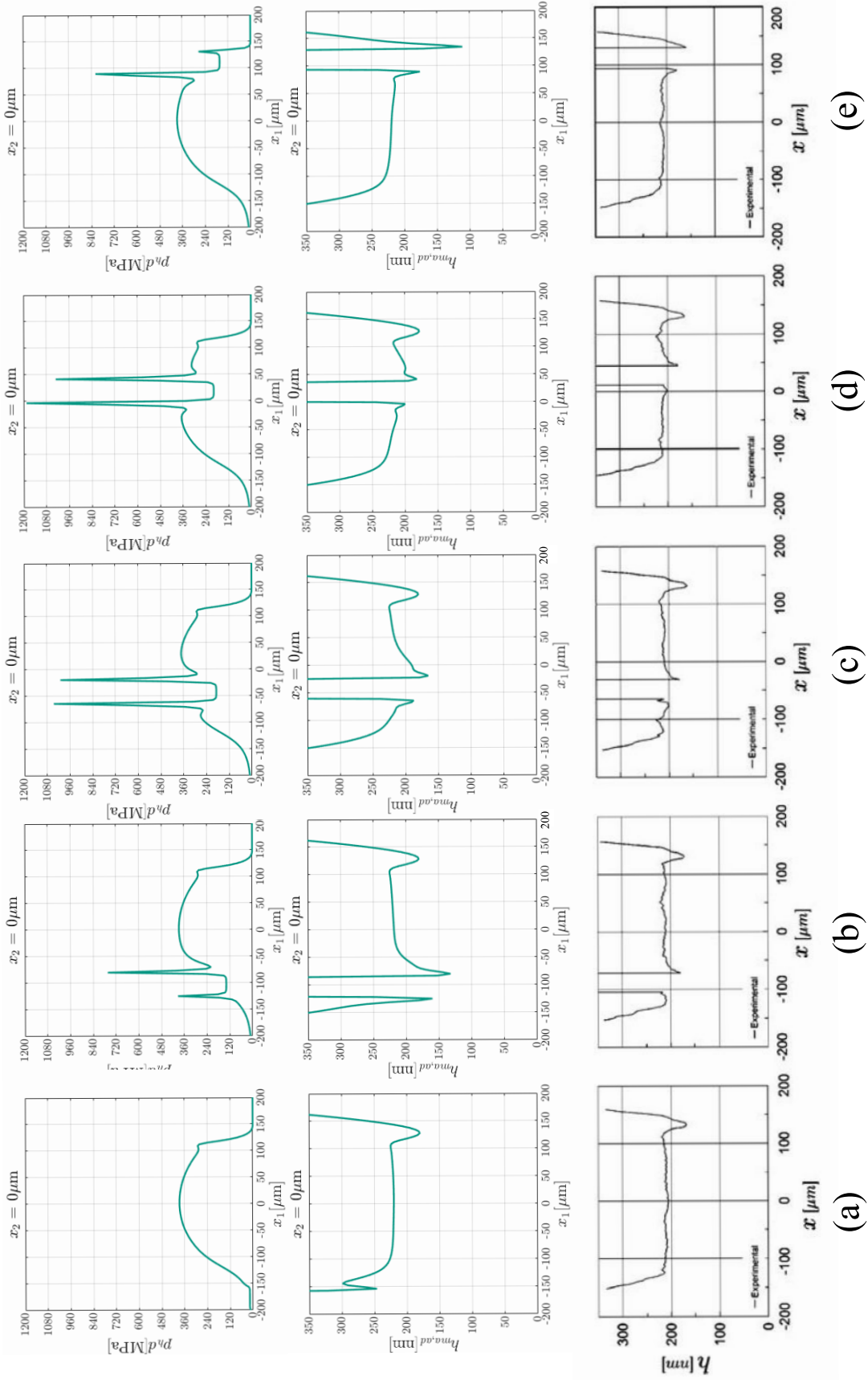


Figure 4.3.: The theoretical pressure (top) and gap height (middle) distributions with the experimental measurements (bottom) for five time points in configuration 1 (SSR=0). Micro-texture center locations approximately corresponding to (a) $\bar{x}_1 = -176 \mu\text{m}$, (b) $\bar{x}_1 = -99 \mu\text{m}$, (c) $\bar{x}_1 = -41 \mu\text{m}$, (d) $\bar{x}_1 = 21.8 \mu\text{m}$, (e) $\bar{x}_1 = 112 \mu\text{m}$. Experimental results provided by Mourier *et al.* [21]. Results of simulation A.1.

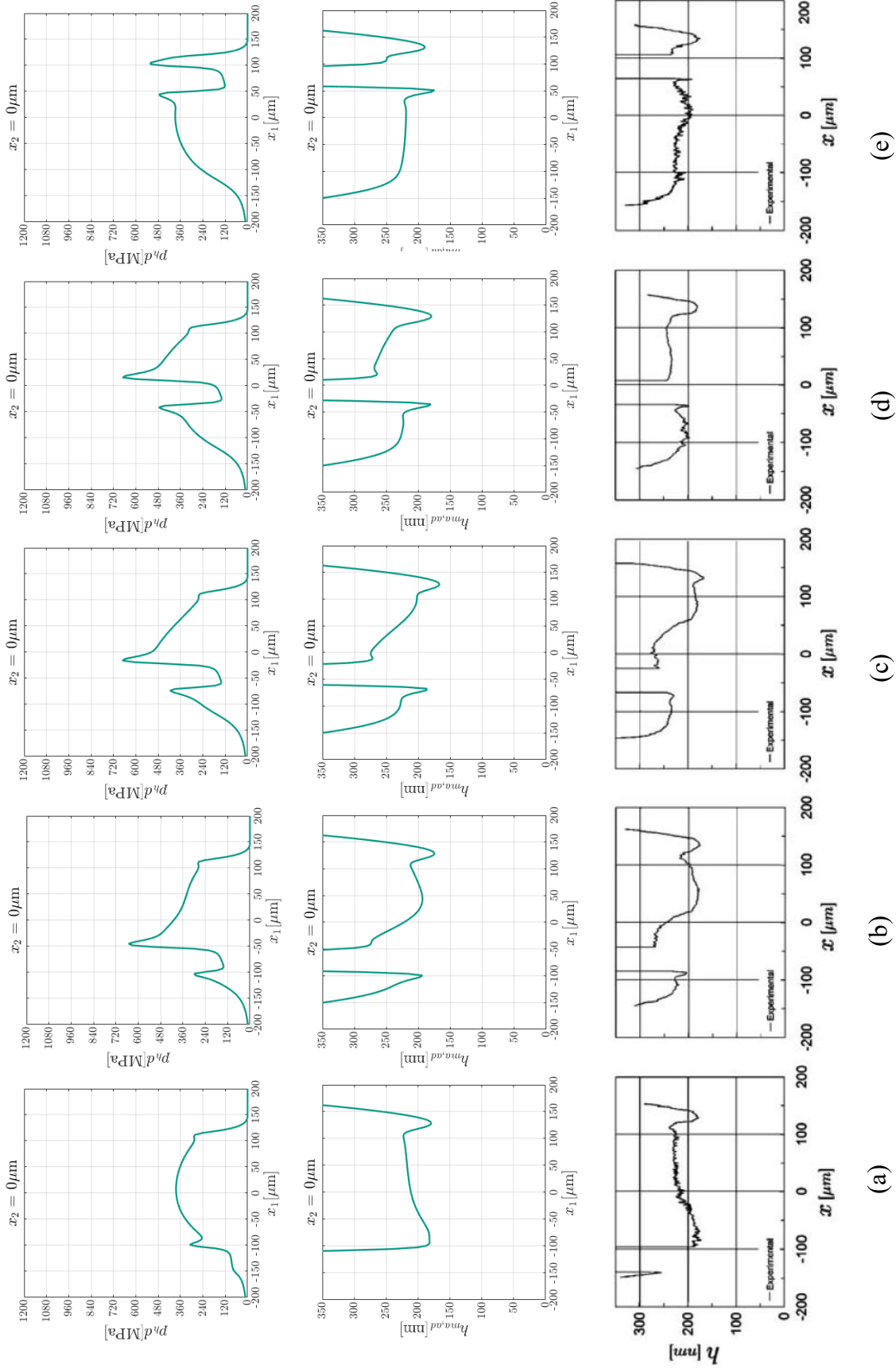


Figure 4.4.: The theoretical pressure (top) and gap height (middle) distributions with the experimental measurements (bottom) for five time points in configuration 2 (SSR=0.5). Micro-texture center locations approximately corresponding to (a) $\bar{x}_1 = -70.1 \mu\text{m}$, (b) $\bar{x}_1 = -41 \mu\text{m}$, (c) $\bar{x}_1 = -9.5 \mu\text{m}$, (d) $\bar{x}_1 = 77 \mu\text{m}$, (e) $\bar{x}_1 = 127 \mu\text{m}$. Experimental results provided by Mourier *et al.* [21]. Results of simulation A.2.

For both configurations, cavitation occurs towards the end of the contact and is observed to not be significantly influenced by the passing of the micro-texture. As the micro-texture moves through, there is a slight increase in the cavity fraction because the lubricant at the center of the micro-texture experiences sudden drops in pressure. The precise changes to the cavity fraction and their explanation are not in the scope of this thesis, so they are only briefly mentioned.

The number of total FBNS and secant algorithm iterations required to move to the next time point are plotted against time for both configurations in Fig.4.8. It can be observed that the first time point usually requires the most amount of iterations, which is expected as the initial guess of the pressure distribution is far from the actual one. Then, both algorithms start to require less iterations for the next few time points. This is because of the relatively small change compared to the value of the gap height the micro-texture introduces as it moves from time point to time point when it is far from the inlet. The gap height as seen in Figs.4.3 and 4.4 is considerably larger as one considers more and more negative x_1 -coordinates. Quickly after, the curves shown in Fig.4.8 rise as the micro-texture now introduces a significant amount of change in the gap height with each passing time point. As expected, when the micro-texture leaves the central area of the contact, since its relative influence decreases, the number of iterations go down as well. Furthermore, in Fig.4.8 (a) more iterations are required for both algorithms per time point overall. This can be explained by considering the differences in ball velocity between the two configurations. For configuration 1, the ball moves faster due to the increased slide-to-roll ratio. This means for configuration 1 with each time step, recalling that the micro-texture is placed on the ball, the relative change introduced by the movement of the micro-texture is larger compared to configuration 2, causing more iterations to be made to as the first guess is further away from the solution. It is also significant to remark that the time step sizes are of the same magnitude for both configurations. This is because the non-dimensional grid spacings, the mean velocity in x_1 -direction (U_1) and the Hertzian contact radii (a) are the same for both.

To sum up, it can be said that, the predictions agree to a better extent with the experimental results for configuration 2, compared to the first one. Nonetheless, even the results for the first configuration are sufficiently similar to the experimental measurements. Thus, the model for predicting the pressure distribution for the ball-on-disc tribometer with a micro-texture on the ball is considered to be validated to a sufficient degree. This is done by confirming the accuracy of the gap height distribution predictions with experimental results. Further studies on the developed solver are presented after the figures in the following pages.

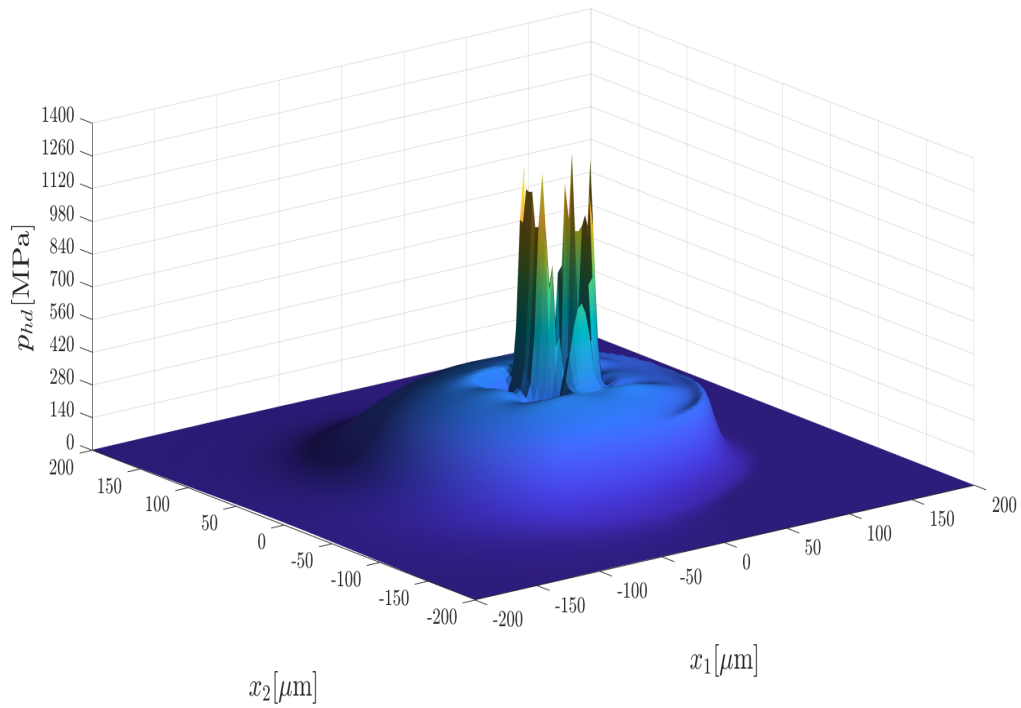


Figure 4.5.: The pressure distribution across the contact as a surface plot, when $\bar{x}_1 = 21.8 \mu\text{m}$ for configuration 1. Result of simulation A.1.

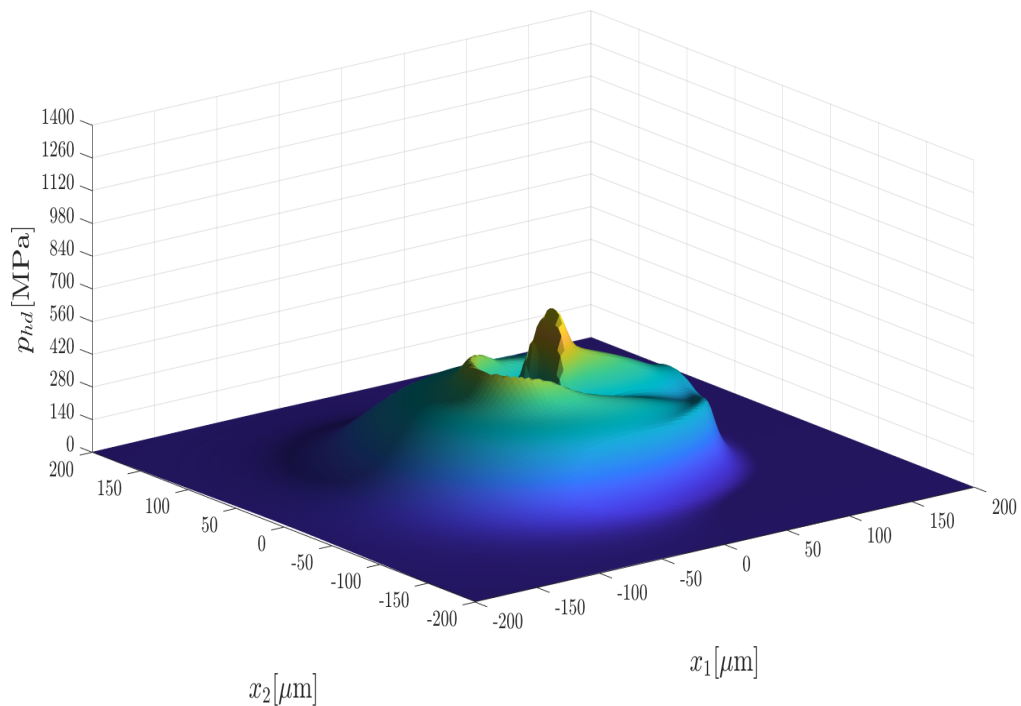
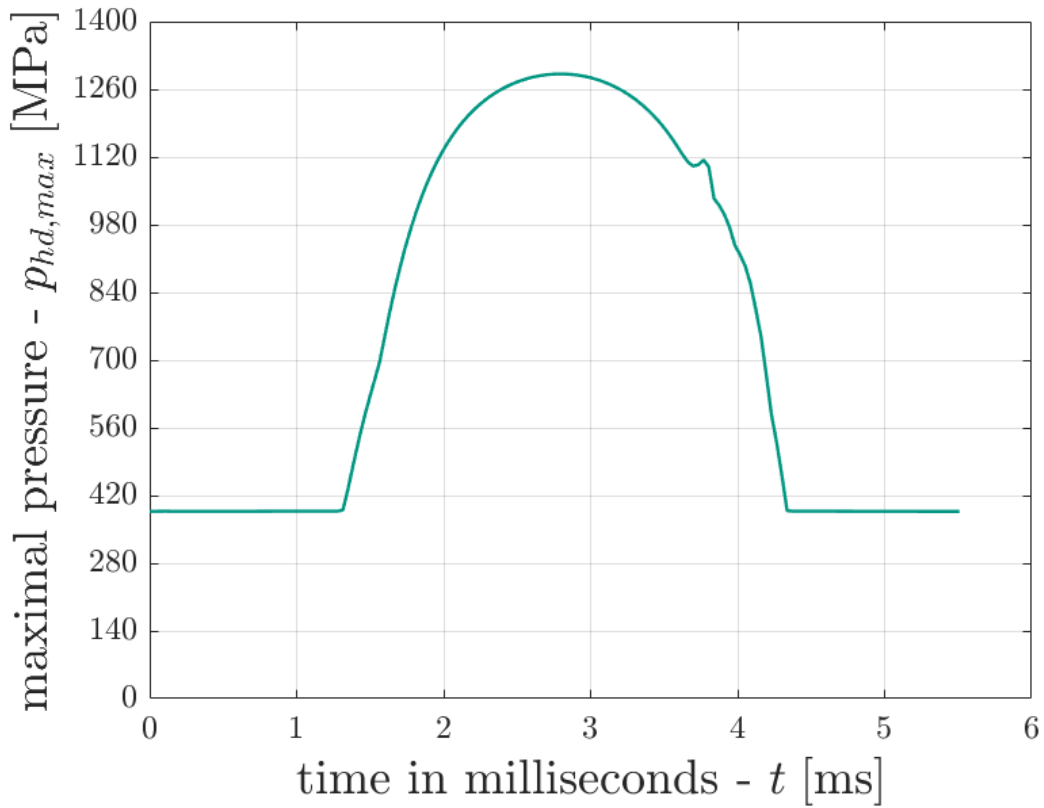
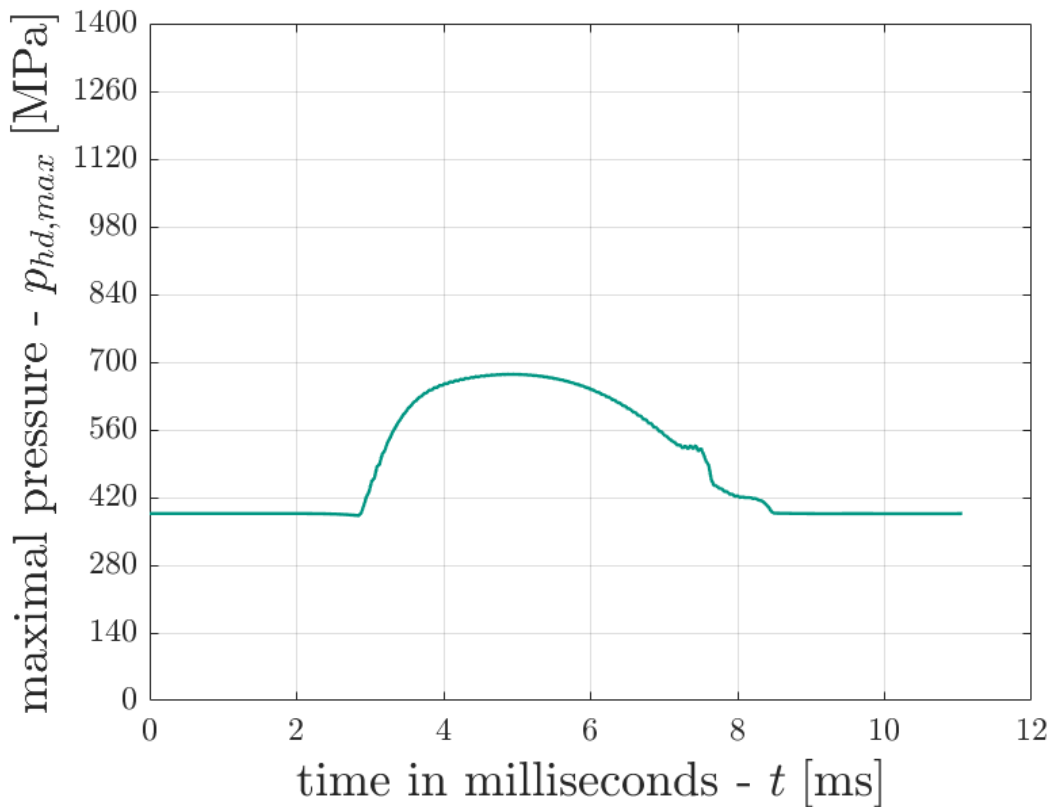


Figure 4.6.: The pressure distribution across the contact, when $\bar{x}_1 = -9,5 \mu\text{m}$ for configuration 2. Result of simulation A.2.

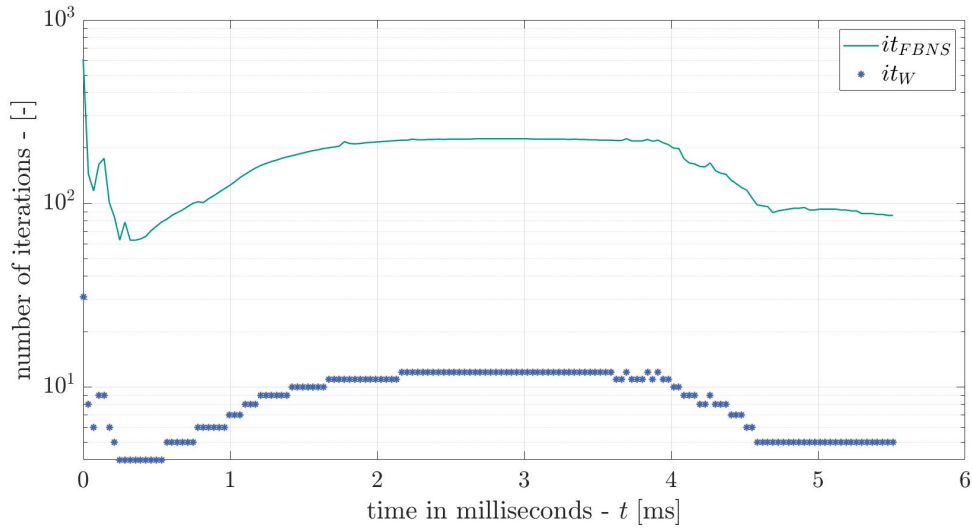


(a) For configuration 1 (SSR=0).

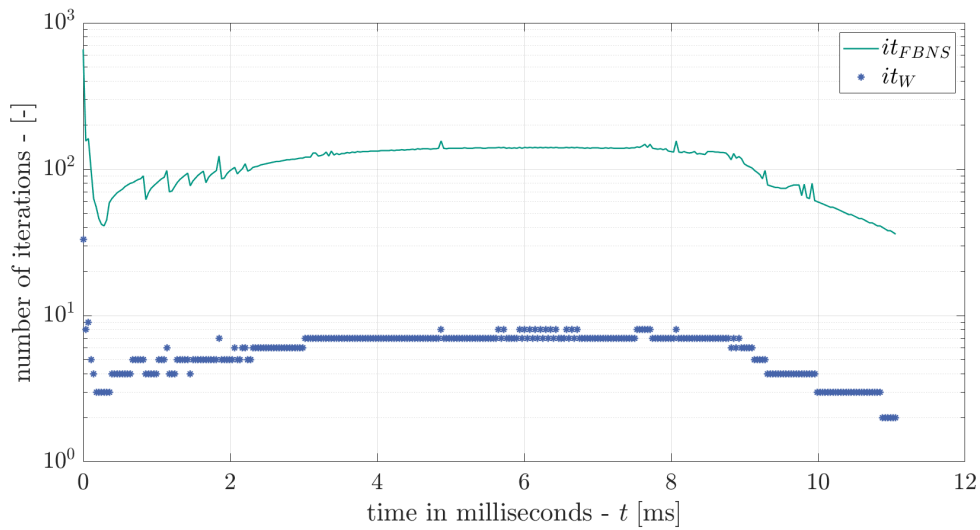


(b) For configuration 2 (SSR=-0.5).

Figure 4.7.: Calculated maximum pressure values across the whole contact area plotted against time for both configurations. Results of simulations A.1 and A.2.



(a) For configuration 1 (SSR=0)



(b) For configuration 2 (SSR=-0.5)

Figure 4.8.: FBNS ($it_{FBNS} = it_p$) and secant ($it_W = it_{sec}$) algorithm iterations required to satisfy the residual tolerances to move to the next time point plotted against time for both configurations. The vertical axis is in logarithmic scale and the horizontal axis is shown using a linear scale. The horizontal axis denotes the time within the simulation, not to be confused with the actual elapsed computational time in the physical world. Results of simulations A.1 and A.2.

4.3. Studies on the Model

In this section, the various studies outlined in section 4.1 are explained. The most relevant results are presented and briefly discussed.

4.3.1. Grid Size

For study B, three different grid sizes are chosen: 65×65 , 127×127 and 257×257 . A finer grid of 513×513 was also considered but it was found to be computationally infeasible. For both configurations and all three grid sizes the gap height distributions

and the hydrodynamic pressure profiles along a constant line of $x_2 = 0$ are presented. Additionally, maximum pressure and minimum gap height values are plotted against time for configuration 2.

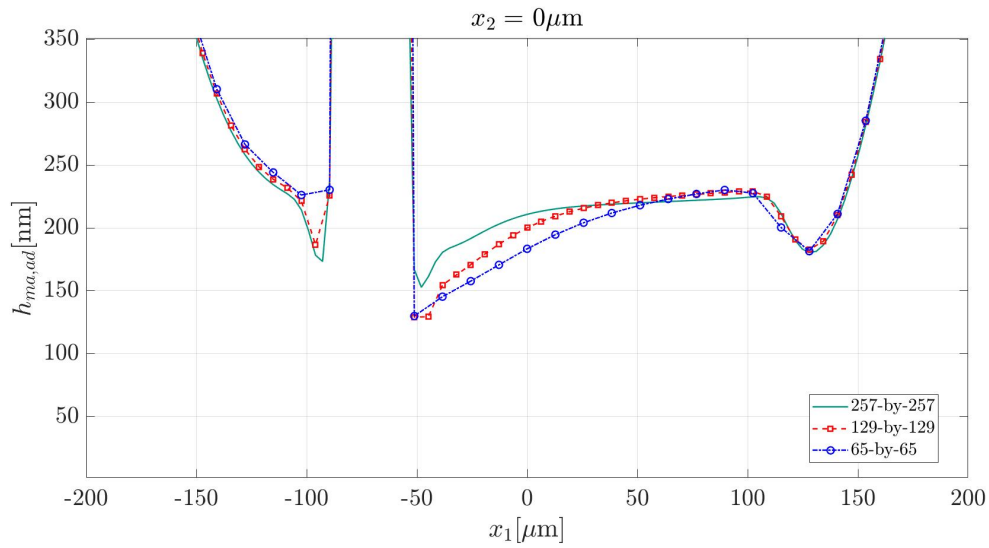
For configuration 1, the gap height and hydrodynamic pressure distributions are displayed in Fig.4.9 when the micro-texture center is at $x_1 = -70 \mu\text{m}$. The general trend that can be observed is that, as the grid gets finer, the decrease of gap height in front of the micro-texture and the decrease in the wake of it, become less pronounced. The pressure peaks around the texture decrease in magnitude as the grid gets coarser.

As for configuration 2, a better agreement between the three considered grid resolutions is observed. The predicted gap height is larger ahead of the micro-texture, at the location $x_1 \approx 50 \mu\text{m}$. In Fig.4.4 (b) it can be seen that the gap height is supposed to decrease in that region. Thus, coarse grids, as expected, represent the experiment with less accuracy. The pressure profiles do not differ drastically as the grid is refined.

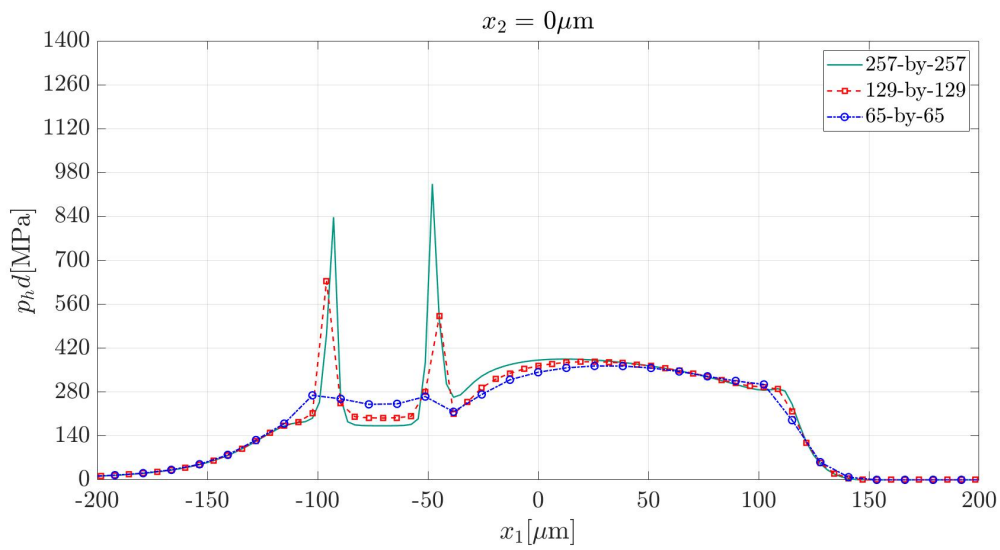
To investigate the behaviour of the simulations for all time points, the maximal pressure and minimal gap height across the whole contact is plotted for the three grid sizes, under the operating conditions of configuration 2 in Fig.4.11. It can be observed that the coarser grids show oscillations in the maximum pressure and the coarsest grid exhibits a large decrease in the minimum gap height after 8 ms. On the other hand, the 257×257 grid shows no significant oscillations in maximum pressure and no decrease for the minimum gap height. The minimum gap heights in non-textured EHL contacts are usually observed in the sides of the domain, in the case considered here: the south and the north domain boundaries, as the micro-texture moves from the west to the east boundary. It is apparent that for coarser grids, the passing of the micro-texture causes the minimum gap height within the contact to fall below the values at the contact edges, while for finer grids this is not the case. This reduction of the minimum gap height in the coarser grids can be caused by the sudden pressure drop right before the 8ms mark, compare Fig.4.11 (a) and (b). Cavitation occurs only at the outlet of the contact and it is hypothesized that it has a significant effect on the pressure and that the predicted cavity fraction is much less accurate for the coarse grids, causing non-physical decreases in the pressure and the minimum gap height.

As the spatial grid gets finer, the total time required to carry out the simulations drastically increases as illustrated in Table 4.5. Both the average computational time spent per time step and the total computation time increase. Simulations corresponding to configuration 2 take longer to compute because the micro-texture moves slower. The slower velocity of the micro-texture improves t_{avg} as the relative change from one time point to the other caused by the movement of the micro-texture gets smaller. An unexpected result is observed for simulation B.1 (the coarsest grid for configuration 1). For B.1 the maximal elapsed computational time for a single time point, t_{max} , is considerably higher than the t_{max} for the 129×129 grid. This is because of observed instabilities for the coarsest grid. For B.1, the time point that takes the longest to compute is not actually the first one but a time point when the micro-texture is about to leave the contact. The algorithm showed tendencies to be unstable and did not converge until the maximum number of secant algorithm iterations were reached, thereby causing the computational time to be unexpectedly large for this one time point. No further instabilities were observed during the analysis.

These considerations are interpreted to mean that a relatively fine grid size of 257×257 is feasible to have appropriate results from simulations. However, if a grid of 129×129 is used, a significant reduction in computational effort, as indicated in Table 4.5, can be achieved with some loss in accuracy. Thus, a compromise must be made depending on the priorities one might have when carrying out the simulations.

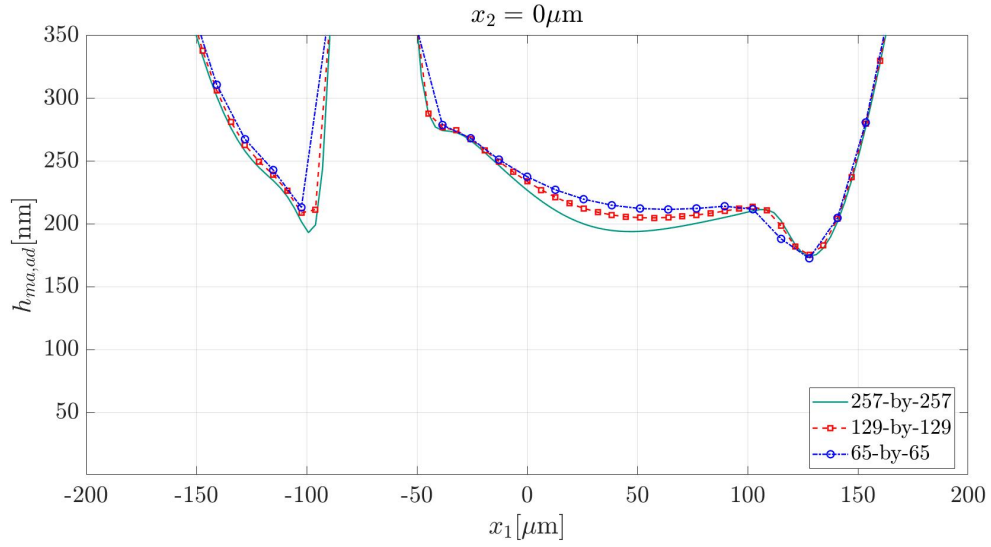


(a) Gap height.

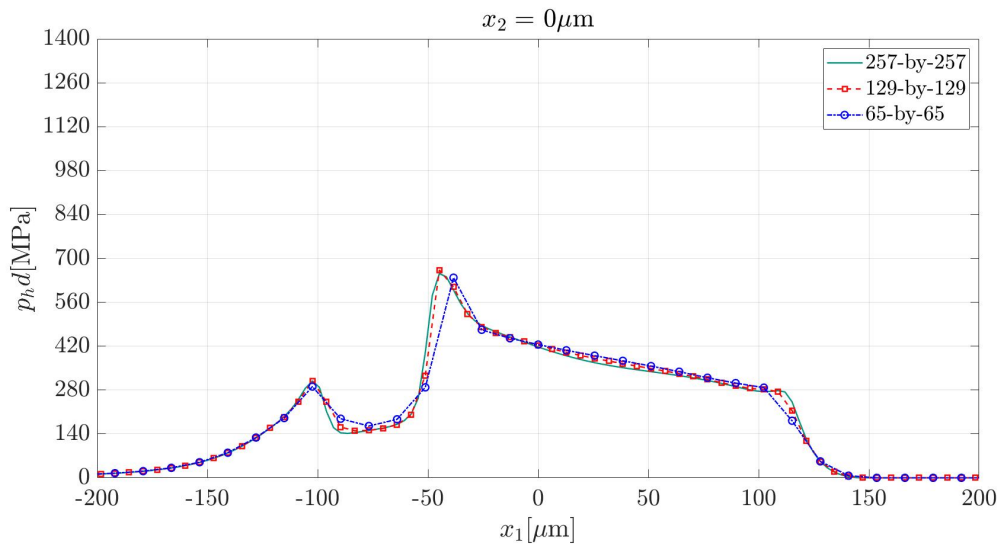


(b) Hydrodynamic pressure.

Figure 4.9.: Gap height and hydrodynamic pressure along a line of $x_2 = 0$ for configuration 1 for three different resolutions, with $\Delta T = \Delta X$. Micro-texture center located at $\bar{x}_1 = -70 \mu\text{m}$. Results of simulations B.1, B.2 and B.3.

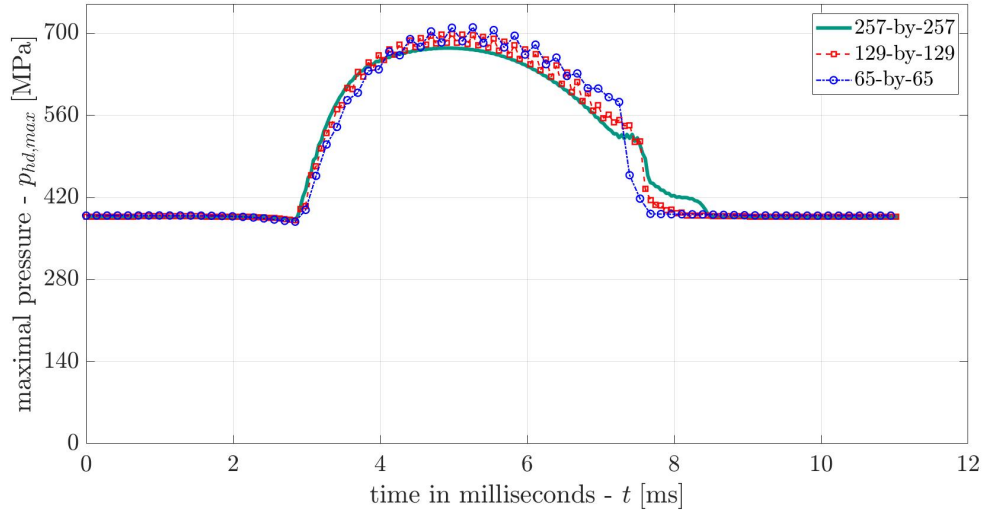


(a) Gap height.

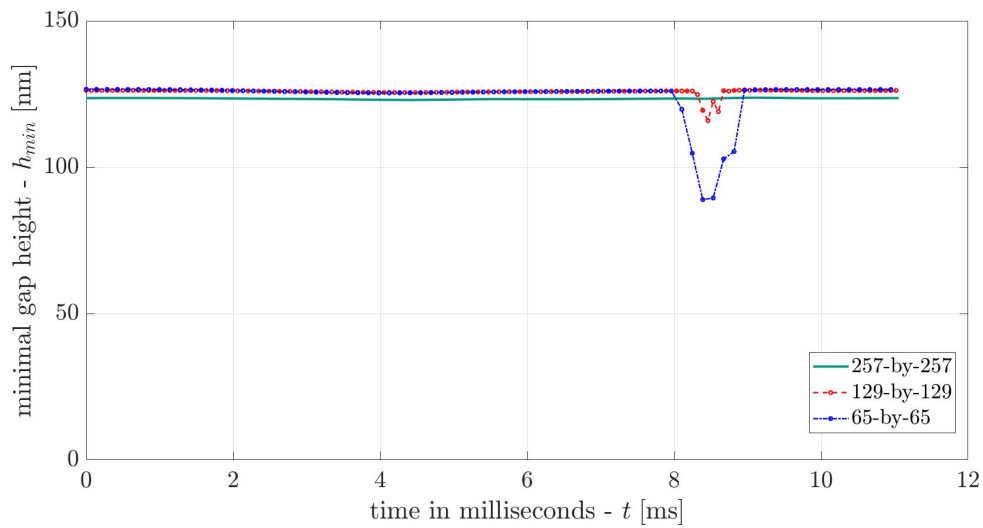


(b) Hydrodynamic pressure.

Figure 4.10.: Gap height and hydrodynamic pressure along a line of $x_2 = 0$ for configuration 2 for three different resolutions, with $\Delta T = \Delta X$. Micro-texture center located at $\bar{x}_1 = -70 \mu\text{m}$. Results of simulations B.4, B.5 and B.6.



(a) Maximum hydrodynamic pressure across the contact.



(b) Minimum gap height across the contact.

Figure 4.11.: Temporal behaviour of the theoretical predictions for configuration 2 for three grid resolutions as shown in the corresponding legends. Results of simulations B.4, B.5 and B.6.

4.3.2. Temporal Resolution

The results of study C is presented in this section. The ratio of the dimensionless time step size to the dimensionless grid size is varied. The gap height distributions for one time point, when the micro-texture center is at $x_1 = -70 \mu\text{m}$, are compared and all time resolutions. Then, the temporal evolution of the maximum pressure across the contact is discussed.

Fig.4.12 (a) shows that the maximum pressure still shows oscillations as observed in Fig.4.11 (a) even at the finest studied time resolution(C.1). Fig.4.12 (b) shows a zoomed in view with all the results included⁴. It can be seen that the larger the time step size gets, the more the predicted maximum pressure increases. The oscillation of the maximum

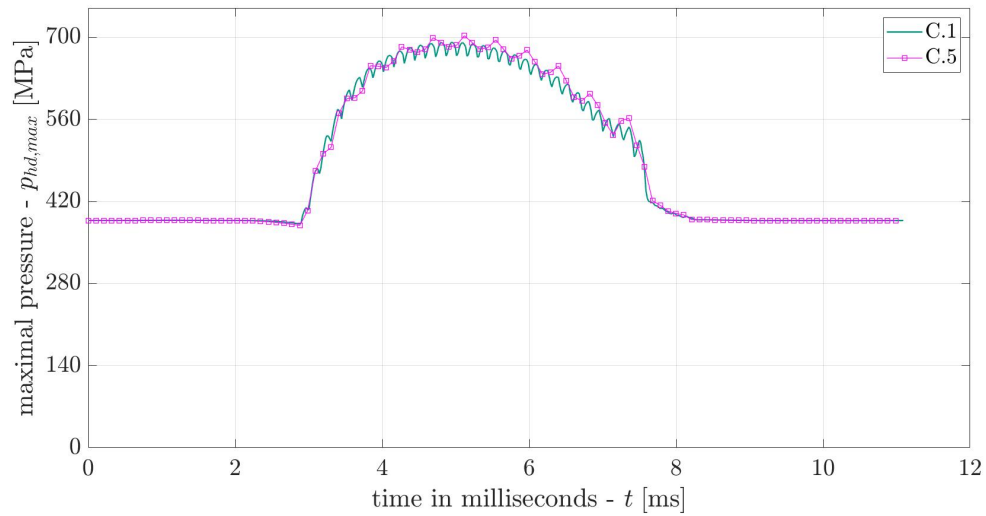
⁴Fig.4.12 (a) shows only two simulation results because the curves are almost overlapping and very hard to distinguish in the zoomed out view.

predicted pressure seem to decrease in frequency as well, but this could be because of the simulations with larger time step sizes having less time points overall, *i.e.* less points are plotted in the graph. This leads to the conclusion that the spatial grid spacing is the main influencing factor on the the observed oscillations.

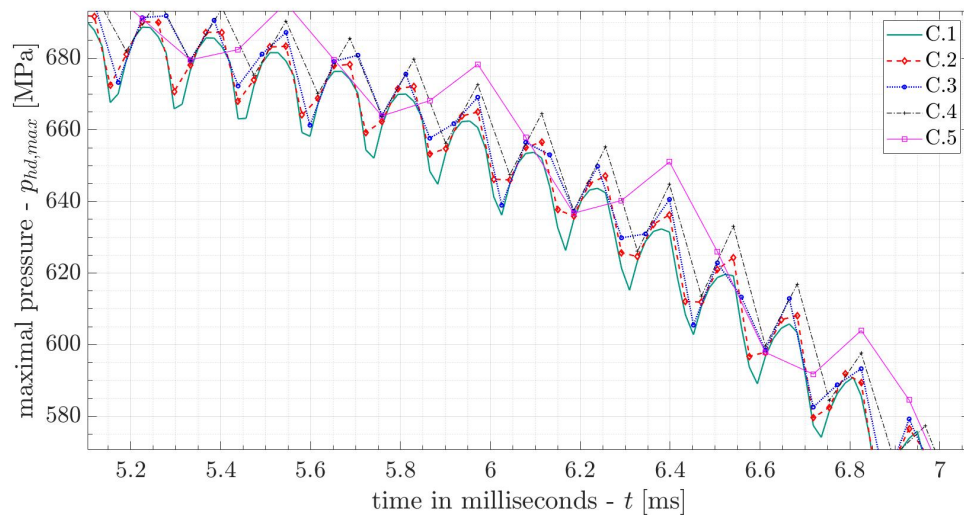
Fig.4.13 illustrates the gap height distribution for the various time step sizes. Comparison to the experimental results displayed in Fig.4.4, shows that the film thickness decrease further in front of the micro-texture is the expected result. As the time resolution gets finer, this is precisely what is observed in Fig.4.12 (b). Simulations C.1 and C.2 result in sufficiently close approximations of the film thickness in that region, leading to to the conclusion that the time step size used in C.2 is accurate enough.

The general trend in the computational times, as it can be seen from Table 4.5 is that as the time resolution gets finer, *i.e.* the ratio $\Delta T/\Delta X$ decreases, the total computational time, t_{tot} , increases while the average computation time spent per time point decreases. This can be explained because the smaller the considered time steps are, the smaller the change that is induced by the movement of the micro-texture. However, this decrease cannot compensate for the increase in the total elapsed time. As expected, t_{max} does not vary as the spatial grid is kept constant and the temporal resolution is refined. It corresponds to the solution of the steady state in the first time point, thus only depends on spatial resolution.

All of the relevant figures for the time step size analysis can be found in the following pages. Thus, the behaviour of the developed algorithm based on the previously described models have been outlined depending on the space and time discretization for the given operating conditions.

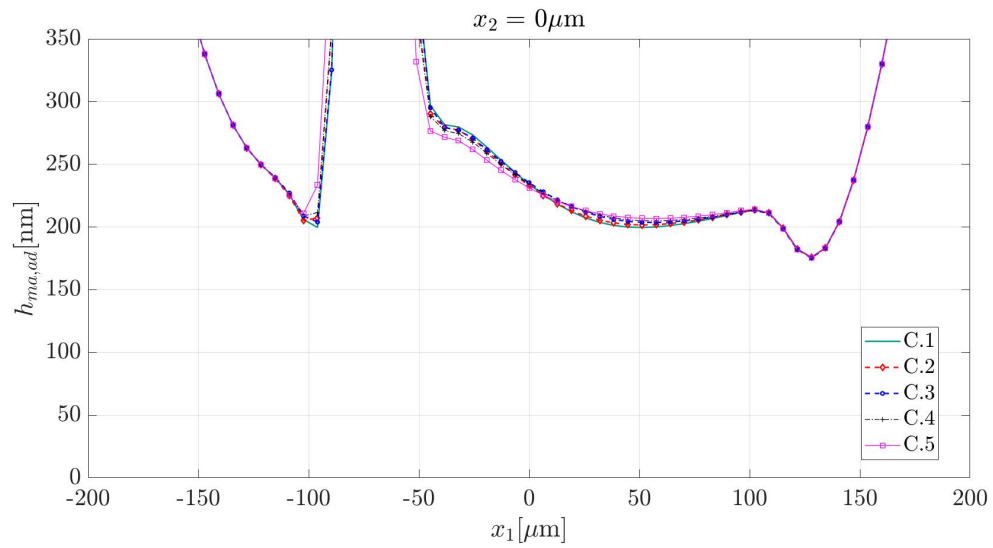


(a) The maximum pressure with the smallest (C.1) and the largest (C.5) time step.

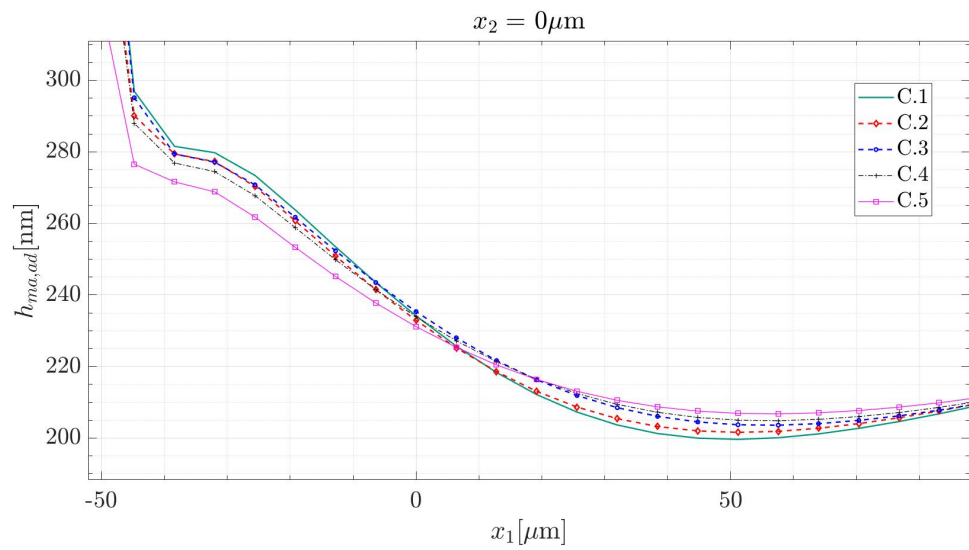


(b) Zoomed in view with all simulations.

Figure 4.12.: The maximum hydrodynamic pressure across the contact plotted against time. Simulations have varying time step sizes, the smallest time step size is used for C.1 and the largest is used for C.5. Results of simulations C.1 to C.5, details in Table 4.5.

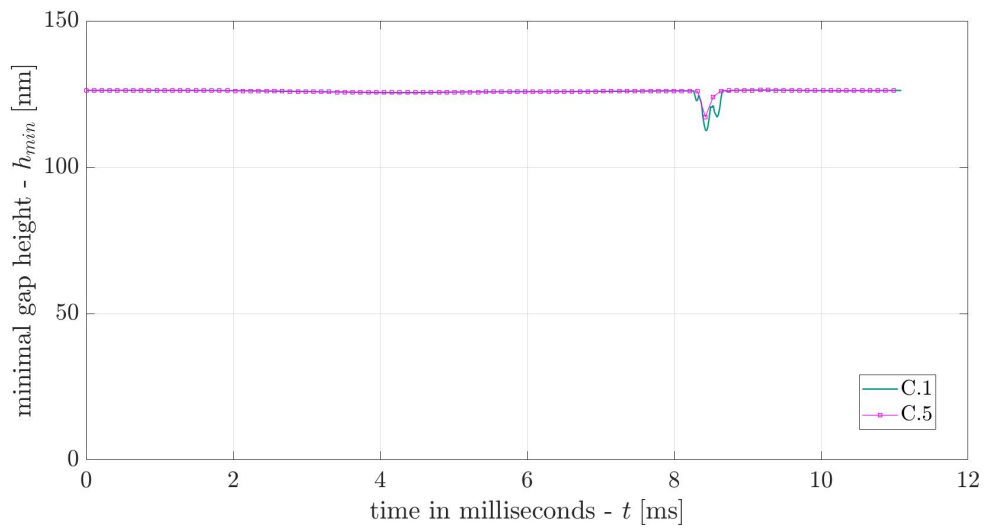


(a) Zoomed out view.

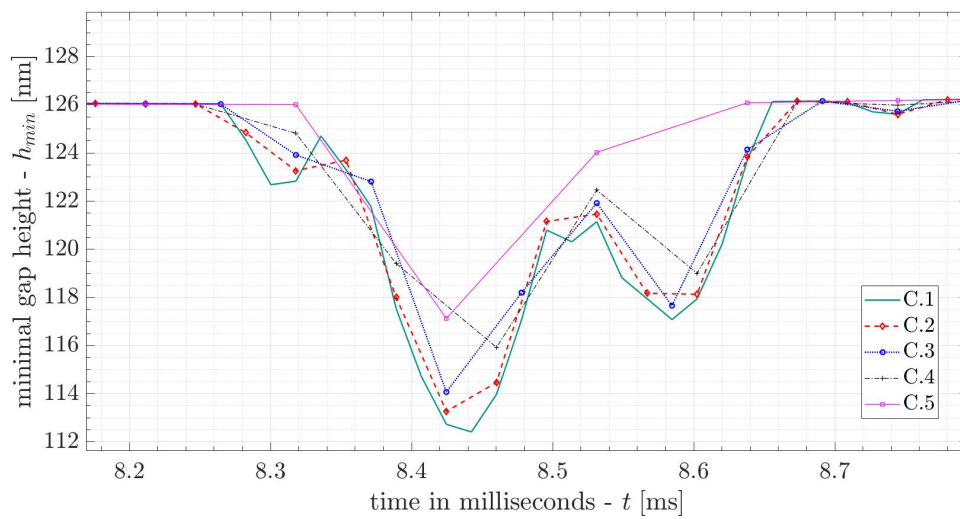


(b) Zoomed in view.

Figure 4.13.: The gap height distribution when $\bar{x}_1 = -70 \mu\text{m}$ with varying time step size. Results of simulations C.1 to C.5, details in Table 4.5.



(a) The minimum gap height with the smallest (C.1) and the largest (C.5) time step.



(b) Zoomed in view with all simulations.

Figure 4.14.: Minimum gap height across the contact for varying step sizes. Results of C.1 to C.5

5. Conclusion

All four goals of this thesis mentioned in the beginning have been reached. To be able to extend the supplied steady EHL solver by Erik Hansen to include transient configurations, the required fundamentals of tribology and the necessary theory to derive the governing equations of the three critical phenomena in EHL: fluid flow, elastic deformation and the pressure-dependency of the lubricant properties (constitutive equations) were explained. The used mass-conserving cavitation model is introduced into the Reynolds equation. The discretization and interpolation methods utilized in the steady solver have been expanded to include the time derivative term in the Reynolds equation, alternatively called the combined expansion and squeeze term. The existing algorithm was modified to include a time loop for marching through time and to include a single micro-texture of adjustable profile. Then, the developed algorithm was validated by comparing the predicted gap height distributions to the experimental results of Mourier *et al.* [21]. A good agreement between them was found, and thus, the predicted pressure distributions were considered to be accurate and be validated as the gap height is directly influenced by pressure. The dependency of the numerical model on the spatial and temporal discretization resolution were also investigated. A grid size of 257×257 was found to be sufficiently accurate to replicate experimental setups and it was proposed to use a coarser grid if low computational effort is of high priority. Except for the coarsest grid size, 65×65 , the solver showed no tendencies to be unstable, which is a benefit of using the Euler implicit method for time discretization. An overall characterization of the algorithm based on the quality of the space and time discretization was presented. This concludes the work of this thesis. What remains now is to discuss open questions and the outlook for further research following this work.

The developed algorithm can be further built upon by introducing the possibility to include multiple micro-textures, which would be more realistic for industry applications of surface texturing. Some challenges in accomplishing this could be to create a periodic expression for the micro-textures. Finding experimental data to validate the numerical predictions with, would pose another challenge. As the focus of this thesis was to develop and validate the unsteady solver, further work could be done on optimizing the parameters for the algorithm and an in depth analysis of its dependency on various parameters and operating conditions would be very valuable. One limitation that could be faced is the simplicity, therefore the limited validity, of the used constitutive relations. Further development could be made by the introduction of more complex but accurate models for the pressure and shear dependency of lubricant parameters. This would require special attention to avoid

any instabilities or any increases of computational effort that might arise. During the literature survey for this thesis, it was also realized that multi-grid methods are used very often in the field of EHL simulations. It would be worthwhile to compare the performance of the approach presented in this thesis to multi-grid solvers. The author of this thesis sincerely hopes that in the future, with contributions from others, the developed algorithm can be used by many researchers in the field and be helpful to others seeking to reduce friction and improve the efficiency of their systems.

Symbols and Abbreviations

Latin Symbols

Symbol	Unit	Description
a	[m]	Hertzian contact radius
A_{time}, A_h	$\left[\frac{\text{kg}}{\text{Pa}\cdot\text{s}}\right]$	Additional coefficients that are introduced to the Jacobian when the p dependence of h is introduced to the Reynolds equation
A_p	$\left[\frac{\text{kg}}{\text{Pa}\cdot\text{s}}\right]$	The coefficients of the pressure terms in the expression for \vec{G} and a part of the Jacobian matrix
B	[kg/s]	The coefficients of the cavity fraction terms in the expression for \vec{G} and the cavity fraction coefficients for the Jacobian
C_f	[-]	Friction coefficient
E	[Pa]	Young's modulus
E'	[Pa]	Equivalent Young's modulus
e_{ij}	[1/s]	Rate of deformation tensor
F_f	[N]	Friction force
$F_N = F_3$	[N]	Normal force
G	[Pa]	Shear modulus (same as $\tilde{\mu}$)
\vec{G}	[kg/s]	The system of equations that describes the discretized Reynolds equation with the cavitation model. Corresponds to the residual
\mathcal{H}	[-]	Hersey number
h	[m]	Gap height
h_δ	[m]	Adjustment amount to first and second guesses if the maximum or minimum rigid body displacements are reached in the secant algorithm
$h_{0,max}, h_{0,min}$	[m]	Maximum and minimum allowed values for the rigid body displacement in the secant algorithm. The algorithm is reset if these values are reached
$h_{0,n-1}$	[m]	Second guess of the rigid body displacement in the secant algorithm
$h_{0,n-2}$	[m]	First guess of the rigid body displacement in the secant algorithm
h_0	[m]	Rigid body displacement term in the film thickness equation
h_1, h_2	[m]	Non-deformed initial shape of body 1 and 2
h_{min}	[m]	Minimum allowed gap height
$h_{ref,con}$	[m]	Reference length used for the dry contact pressure algorithm
h_u	[m]	Non-deformed gap height

$i_{con,max}$	[-]	Maximum allowed dry contact pressure algorithm iterations
$i_{p,max}$	[-]	Maximum allowed FBNS algorithm iterations before exiting the loop
$i_{sec,max}$	[-]	Maximum allowed secant algorithm iterations before exiting the loop
\mathbf{J} , $\mathbf{J}_{G,p}$, $\mathbf{J}_{F,p}$, $\mathbf{J}_{G,\theta}$, $\mathbf{J}_{F,\theta}$	[matrix]	The Jacobian and its corresponding submatrices for the FBNS algorithm formulation
$K^{ijj'j'}$	[m/Pa]	General form of kernel entries
K_{NW} , K_C , etc.	[m/Pa]	Kernel entries that correspond to the cells indicated in the subscript in relation to the center cell
k_i	[m/s ²]	Mass body force in i -direction
l_0	[m]	Characteristic length for Reynolds number
n_t	[-]	Number of required time points for the microtexture to travel from $x_1 = -250 \mu\text{m}$ to $x_1 = 250 \mu\text{m}$ for the given configuration
p	[Pa]	pressure
\bar{p}	[Pa]	Relative pressure $\bar{p} = p - p_{cav}$
p_{cav}	[Pa]	Cavitation pressure of the lubricant
$p_{ref,p}$	[Pa]	Reference pressure for calculating relative pressure residual in the FBNS algorithm
p_0	[Pa]	Ambient pressure
\tilde{p}_0	[Pa]	Pressure coefficient for the Roelands relation
q'_{x_1} , q'_{x_2}	[m ² /s]	Volume flow rate per unit width in x_1 - and x_2 -directions
r	[m]	Euclidean distance between point of action of the concentrated force (the origin) on the elastic half-space and the point where the elastic deformation is calculated at
R	[m]	Equivalent radius of curvature for the ball surface $\left(\frac{1}{R} = \frac{1}{R_1} + \frac{1}{R_2}\right)$
R_{1,x_1} , R_{1,x_2}	[m]	Principal radii of curvature of body 1 (lower) in x_1 - and x_2 -directions
R_{2,x_1} , R_{2,x_2}	[m]	Principal radii of curvature of body 2 (upper) in x_1 - and x_2 -directions
Re	[-]	Reynolds number
S	[m]	Effect of surface textures on gap height
s'	[m]	Euclidean distance of the micro-texture center to given x_1 - and x_2 -coordinates
t	[s]	Time
\mathbf{T}	[Pa]	Stress tensor
t_{avg}	[s]	Average elapsed computational time per time point in a given simulation In seconds
t_{max}	[s]	Maximum elapsed computational time for any time point in a given simulation in seconds
t_{tot}	[h]	Total computational time elapsed for the simulation in hours
u_0	[m/s]	Characteristic velocity for Reynolds number
U_1 , U_2	[m/s]	Mean surface velocities of the solid bodies in x_1 - and x_2 -directions

$u_{i,b}, u_{i,a}$	[m/s]	Surface velocity in i -direction of body b (upper) and a (lower)
u_i	[m/s]	Fluid velocity in i -direction
u_r	[m/s]	Relative velocity between solid bodies ($u_r = u_b - u_a$)
W	[Pa]	Average applied load
x_1, x_2, x_3	[m]	Cartesian coordinates used to describe the geometry of the contact
\bar{x}_1, \bar{x}_2	[m]	Micro-texture center coordinates
X_1, X_2, X'_1, X'_2	[m]	Shorthand notation for x_1 - and x_2 -coordinates for the discretized formulation of the linear elasticity equations

Greek Symbols

Symbol	Unit	Description
α	[1/Pa]	Pressure-viscosity index
$\tilde{\alpha}$	[-]	Under-relaxation factor for FBNS algorithm
$\dot{\gamma}$	[1/s]	Shear rate
δ	[m]	Elastic deformation of the solid bodies. Defined positive pointing inwards to the elastic half-space
δ_{ij}	[-]	Kronecker delta
$\delta\vec{p}$	[Pa]	Pressure update for the relative pressure terms in the FBNS algorithm
$\delta\vec{\theta}$	[-]	Cavity fraction update in the FBNS algorithm
ΔX	[-]	Dimensionless grid spacing ($\Delta X = \Delta x_1/a = \Delta x_2/a$)
ΔT	[-]	Dimensionless time step size ($\Delta T = \frac{\Delta t \cdot U_1}{a}$)
$\Delta x_1, \Delta x_2$	[m]	Finite volume grid spacings in x_1 - and x_2 -directions
Δt	[s]	Time step size
Δ_{gen}	[-]	General relative error tolerance for the various algorithms
Δ_p	[-]	Relative residual tolerance of the relative pressure in the FBNS algorithm
θ	[-]	Cavity fraction
$\tilde{\lambda}$	[Pa]	First Lamé parameter
λ^*	[Pa·s]	Second viscosity coefficient
λ_e	[-]	Linear interpolation factor for the central differencing scheme on the east boundary
μ	[Pa·s]	Dynamic viscosity
$\bar{\mu}_0$	[Pa·s]	Characteristic dynamic viscosity for the Reynolds number
$\tilde{\mu}$	[Pa]	Second Lamé constant
μ_l	[Pa·s]	Dynamic viscosity of the lubricant at a given pressure ($\mu = \mu_l$)
μ_0	[Pa·s]	Dynamic viscosity of the lubricant at ambient pressure
ν	[-]	Poisson's ratio
ξ_p	[kg/(Pa·s)]	Poiseuille coefficient in discretized Reynolds equation ($\xi_p = \frac{h^3 \rho_l}{12\mu}$)
ξ_u	[kg/(m·s)]	Coefficient for the Couette terms and the cavity fraction term in the discretized Reynolds equation ($\xi_u = U_1 \rho_l h$)
ξ_t	[kg/m ²]	Coefficient for the combined squeeze and expansion term in the discretized Reynolds equation ($\xi_t = \rho_l h$)
$\xi_{u,h}$	[kg/(m ² ·s)]	First coefficient of the pressure terms that arises from substituting the p dependence of h into the expression for the Jacobian, ($\xi_{u,h} = U_1 \rho_l$)

$\xi_{t,h}$	[kg/m ³]	Second coefficient of the pressure terms that arises from substituting the p dependence of h into the expression for the Jacobian, ($\xi_{t,h} = \rho_l$)
ρ	[kg/m ³]	Lubricant density
$\bar{\rho}_0$	[kg/m ³]	Characteristic density for the Reynolds number
ρ_l	[kg/m ³]	Density of the non-cavitated, liquid lubricant
ρ_0	[kg/m ³]	Density of the lubricant at ambient pressure
σ_{ji}	[Pa]	Stress tensor in index notation
Σ	[-]	Slide-to-roll ratio ($\Sigma = \frac{u_a - u_b}{u_a + u_b}$)
τ_{ji}	[Pa]	Friction stress tensor in index notation
τ_{avg}	[Pa]	Average Couette shear stress
τ_{max}	[Pa]	Set maximal value of the average Couette stress for the shear-thinning model
ϕ	[-]	Generalized variable for explaining interpolation methods
Ω	[1/s]	Rotations per second of the disc, used to explain friction coefficient
∇	[-]	2 dimensional nabla operator ($\nabla = \left(\frac{\partial}{\partial x_1}, \frac{\partial}{\partial x_2} \right)$)

Abbreviations

Abbreviation	Description
EHL	Elastohydrodynamic lubrication
CDS	Central differencing scheme
CV	Control volume
EA	Elrod-Adams
FBNS	Fischer-Burmeister-Newton-Schur
FFT	Fast Fourier transform
FFT ⁻¹	Inverse fast fourier transform
FV	Finite volume
HL	Hydrodynamic lubrication
JFO model	Jakobsson, Floberg and Olson model
LST	Laser surface texturing
rps	Rotations per second
SSR	Slide-to-roll ratio
UDS	Upwind differencing scheme

List of Figures

2.1.	Illustration of surfaces in conformal and non-conformal contacts. Taken from Habchi, 2018 [4].	6
2.2.	A plot of the Stribeck curve showing the various lubrication regimes. Taken from Codrignani [24] who adapted the figure from Hamrock <i>et al.</i> [6].	8
2.3.	The approximated EHL point contact geometry as two elliptic paraboloids. Adapted from Habchi [4] to include the coordinate notation used in this thesis.	9
2.4.	An elastic half-plane loaded by an external concentrated force F . Adapted from Habchi [4] to include the coordinate axes notation.	11
2.5.	The superposition of the two velocity fields that result in the EHL velocity field, taken from Habchi [4].	17
2.6.	A figure illustrating how the gap height changes as the non-flat upper body (body b) moves from the dashed position to the one drawn as a full line in either direction x_1 or x_2 . Adapted from Hamrock <i>et al.</i> to have consistent notation [6].	19
2.7.	Shear stress against shear rate of different types of fluids: (a) Newtonian (b) Shear-thinning (c) Assumed behaviour in this thesis. Inspired by Durst [25].	25
3.1.	An illustration of the used 2D grid in the algorithm where the dashed red square (also bold) is the $(i, j)^{th}$ control volume of interest. The symbols \vec{n} correspond to outward-pointing normal vectors of the surfaces. For the developed algorithm $N_{x_1} = N_{x_2}$ holds. Design inspired by Ferziger [36].	29
3.2.	The illustration of <i>explicit</i> (left) and <i>implicit</i> (right) Euler methods to approximate the time integral in Eq.(3.7). Taken from Ferziger [36]	31
3.3.	Discretized elastic half-space with constant distributed load within each discrete element. x , y , h_x and h_y are equivalent to x_1 , x_2 , Δx_1 and Δx_2 respectively. Taken from Pohrt and Li [29].	32
3.4.	Simplified flow chart of the developed solver, the loops are denoted via Roman numerals.	39
3.5.	An illustration for calculating h_W , the central kernel entry, K_C , is aligned with the west cell of the FV grid. The kernel is mirrored due to the convolution. The relative pressures at C and directly neighbouring cells in the FV grid are of interest.	42
4.1.	The EHL tribometer used by Mourier <i>et al.</i> with their measurement setup. Taken from [21].	46
4.2.	The micro-texture influence on the gap height for the given parametrization for configuration 1, shown as a profile on a line along constant $x_2 = 0$ and along the whole plane, both when $(\bar{x}_1, \bar{x}_2) = (0, 0)$	47

4.3.	The theoretical pressure (top) and gap height (middle) distributions with the experimental measurements (bottom) for five time points in configuration 1 (SSR=0). Micro-texture center locations approximately corresponding to (a) $\bar{x}_1 = -176 \mu\text{m}$, (b) $\bar{x}_1 = -99 \mu\text{m}$, (c) $\bar{x}_1 = -41 \mu\text{m}$, (d) $\bar{x}_1 = 21.8 \mu\text{m}$, (e) $\bar{x}_1 = 112 \mu\text{m}$. Experimental results provided by Mourier <i>et al.</i> [21]. Results of simulation A.1.	54
4.4.	The theoretical pressure (top) and gap height (middle) distributions with the experimental measurements (bottom) for five time points in configuration 2 (SSR=-0.5). Micro-texture center locations approximately corresponding to (a) $\bar{x}_1 = -127 \mu\text{m}$, (b) $\bar{x}_1 = -70.1 \mu\text{m}$, (c) $\bar{x}_1 = -41 \mu\text{m}$, (d) $\bar{x}_1 = -9.5 \mu\text{m}$, (e) $\bar{x}_1 = 77 \mu\text{m}$. Experimental results provided by Mourier <i>et al.</i> [21]. Results of simulation A.2.	55
4.5.	The pressure distribution across the contact as a surface plot, when $\bar{x}_1 = 21.8 \mu\text{m}$ for configuration 1. Result of simulation A.1.	57
4.6.	The pressure distribution across the contact, when $\bar{x}_1 = -9,5 \mu\text{m}$ for configuration 2. Result of simulation A.2.	57
4.7.	Calculated maximum pressure values across the whole contact area plotted against time for both configurations. Results of simulations A.1 and A.2.	58
4.8.	FBNS ($it_{FBNS} = it_p$) and secant ($it_W = it_{sec}$) algorithm iterations required to satisfy the residual tolerances to move to the next time point plotted against time for both configurations. The vertical axis is in logarithmic scale and the horizontal axis is shown using a linear scale. The horizontal axis denotes the time within the simulation, not to be confused with the actual elapsed computational time in the physical world. Results of simulations A.1 and A.2.	59
4.9.	Gap height and hydrodynamic pressure along a line of $x_2 = 0$ for configuration 1 for three different resolutions, with $\Delta T = \Delta X$. Micro-texture center located at $\bar{x}_1 = -70 \mu\text{m}$. Results of simulations B.1, B.2 and B.3.	61
4.10.	Gap height and hydrodynamic pressure along a line of $x_2 = 0$ for configuration 2 for three different resolutions, with $\Delta T = \Delta X$. Micro-texture center located at $\bar{x}_1 = -70 \mu\text{m}$. Results of simulations B.4, B.5 and B.6.	62
4.11.	Temporal behaviour of the theoretical predictions for configuration 2 for three grid resolutions as shown in the corresponding legends. Results of simulations B.4, B.5 and B.6.	63
4.12.	The maximum hydrodynamic pressure across the contact plotted against time. Simulations have varying time step sizes, the smallest time step size is used for C.1 and the largest is used for C.5. Results of simulations C.1 to C.5, details in Table 4.5.	65
4.13.	The gap height distribution when $\bar{x}_1 = -70 \mu\text{m}$ with varying time step size. Results of simulations C.1 to C.5, details in Table 4.5.	66
4.14.	Minimum gap height across the contact for varying step sizes. Results of C.1 to C.5	67
A.1.	Detailed flowchart of the main algorithm.	84
A.2.	Detailed flowchart of the secant algorithm.	85
A.3.	Detailed flowchart of the FBNS algorithm.	86

List of Tables

4.1.	Overview of configuration 1 and 2 as given by Mourier <i>et al.</i> The geometry parameter d is the micro-texture depth and r is the corresponding micro-texture radius. The lower and upper bodies velocities, respectively u_a and u_b , are calculated from the SSR and U_1 [21].	48
4.2.	Table of geometry parameters, solid and lubricant properties and operating conditions as given by Mourier <i>et al.</i> [21].	48
4.3.	Summary of required parameters for the various algorithms and the values used. See text for explanations.	50
4.4.	Specifications of the computer used to run all simulations.	51
4.5.	Overview of all carried out simulations and elapsed times for each simulation. “Sim.” stands for simulation and indicates the study the simulations belong to and their number. “ID” denotes the internally used identification number when simulations were being carried out. ΔT and ΔX are the dimensionless time step size and grid spacing respectively. “Con.” is the number of the configuration, corresponding to 1 for SSR=0 and 2 for SSR=-0.5. $\tilde{\alpha}$ is the under-relaxation factor used in the FBNS algorithm, n_t is the number of computed time points, t_{tot} is the total elapsed time for the simulation in hours, t_{max} is the elapsed time for the time point that took longest to compute in seconds, t_{avg} is the average computational time per time point in seconds. ct_{max} is the number of maximum computational threads allowed for the simulation.	51
4.6.	Dimensionless grid spacings, ΔX , for different spatial resolutions.	52

Bibliography

- [1] Michael M. Khonsari and E. Richard Booser, *Applied Tribology : Bearing Design and Lubrication*, vol. Third edition of *Tribology in Practice Series*. Hoboken, NJ: Wiley, 2017.
- [2] K. Holmberg and A. Erdemir, “Influence of tribology on global energy consumption, costs and emissions,” *Friction*, vol. 5, no. 3, pp. 263–284, 2017.
- [3] K. Holmberg, P. Andersson, and A. Erdemir, “Global energy consumption due to friction in passenger cars,” *Tribology International*, vol. 47, pp. 221–234, 2012.
- [4] W. Habchi, *Finite element modeling of elastohydrodynamic lubrication problems*. Hoboken NJ: John Wiley & Sons, 2018.
- [5] D. Gropper, L. Wang, and T. J. Harvey, “Hydrodynamic lubrication of textured surfaces: A review of modeling techniques and key findings,” *Tribology International*, vol. 94, pp. 509–529, 2016.
- [6] Hamrock, Bernard J., Steven R. Schmid, and Bo O. Jacobson, *Fundamentals of Fluid Film Lubrication Second Edition*. MARCEL DEKKER, INC., 2004.
- [7] H. A. Spikes, “Sixty years of ehl,” *Lubrication Science*, vol. 18, no. 4, pp. 265–291, 2006.
- [8] A. Cameron, “Righting a 40-year-old wrong: Am ertel—the true author of ‘grubin ehl’solution,”” *Tribology International*, vol. 18, no. 2, p. 92, 1985.
- [9] D. B. Hamilton, J. A. Walowit, and C. M. Allen, “A theory of lubrication by microirregularities,” *Journal of Basic Engineering*, vol. 88, no. 1, pp. 177–185, 1966.
- [10] I. Etsion and L. Burstein, “A model for mechanical seals with regular microsurface structure,” *Tribology Transactions*, vol. 39, no. 3, pp. 677–683, 1996.
- [11] I. Etsion, “State of the art in laser surface texturing,” *Journal of Tribology*, vol. 127, no. 1, pp. 248–253, 2005.
- [12] H. G. Elrod and M. L. Adams, “A computer program for cavitation and starvation problems: in proceeding of the first leeds-lyon symposium,” *Cavitation and related phenomena in lubrication*, vol. 37, 1974.
- [13] B. Jakobsson and L. Floberg, “The finite journal bearing, considering vaporization,” *Transactions of Chalmers University of Technology*, vol. 190, 1957.
- [14] K.-O. Olsson, “Cavitation in dynamically loaded bearings,” *Transactions of Chalmers University of Technology*, vol. 308, 1965.
- [15] M. Giacomini, M. T. Fowell, D. Dini, and A. Strozzi, “A mass-conserving complementarity formulation to study lubricant films in the presence of cavitation,” *Journal of Tribology*, vol. 132, no. 4, 2010.

- [16] L. Bertocchi, D. Dini, M. Giacomini, M. T. Fowell, and A. Baldini, “Fluid film lubrication in the presence of cavitation: a mass-conserving two-dimensional formulation for compressible, piezoviscous and non-newtonian fluids,” *Tribology International*, vol. 67, pp. 61–71, 2013.
- [17] R. Ausas, P. Ragot, J. Leiva, M. Jai, G. Bayada, and G. C. Buscaglia, “The impact of the cavitation model in the analysis of microtextured lubricated journal bearings,” *Journal of Tribology*, vol. 129, no. 4, pp. 868–875, 2007.
- [18] T. Woloszynski, P. Podsiadlo, and G. W. Stachowiak, “Efficient solution to the cavitation problem in hydrodynamic lubrication,” *Tribology Letters*, vol. 58, no. 1, 2015.
- [19] Erik Arne Hansen, “Modelling of mixed elasto-hydrodynamic lubrication,” 2020.
- [20] E. Hansen, B. Frohnapfel, and A. Codrignani, “Sensitivity of the stribeck curve to the pin geometry of a pin-on-disc tribometer,” *Tribology International*, vol. 151, p. 106488, 2020.
- [21] L. Mourier, D. Mazuyer, A. A. Lubrecht, and C. Donnet, “Transient increase of film thickness in micro-textured ehl contacts,” *Tribology International*, vol. 39, no. 12, pp. 1745–1756, 2006.
- [22] R. Stribeck, “Die wesentlichen eigenschaften der gleit-und rollenlager—the key qualities of sliding and roller bearings,” *Zeitschrift des Vereines deutscher Ingenieure*, vol. 46, no. 38, pp. 1342–1348, 1902.
- [23] B. Jacobson, “The stribeck memorial lecture,” *Tribology International*, vol. 36, no. 11, pp. 781–789, 2003.
- [24] Andrea Roberto Codrignani, *Numerical representation of a pin-on-disc tribometer for the investigation of textured surfaces*. Phd, KIT, 2019.
- [25] F. Durst, *Fluid Mechanics: An Introduction to the Theory of Fluid Flows*. Berlin, Heidelberg: Springer Berlin Heidelberg, 2010.
- [26] J. H. Spurk and N. Aksel, *Fluid Mechanics*. Cham: Springer International Publishing, 2020.
- [27] C. D. Coman, *Continuum Mechanics and Linear Elasticity*, vol. 238. Dordrecht: Springer Netherlands, 2020.
- [28] Landau and Lifshitz, *Theory of Elasticity: Course of Theoretical Physics, Volume 7*. Pergamon Press, 1970.
- [29] R. Pohrt and Q. Li, “Complete boundary element formulation for normal and tangential contact problems,” *Physical Mesomechanics*, vol. 17, no. 4, pp. 334–340, 2014.
- [30] C. H. Venner and A. A. Lubrecht, *Multilevel methods in lubrication*, vol. 37 of *Tribology series*. Amsterdam: Elsevier, 1st ed. ed., 2000.
- [31] Bettina Frohnapfel, Davide Gatti, Kay Schäfer, Erik Hansen, and Alina Kuhn, *Mathematische Methoden der Strömungslehre Sommersemester 2020: Lecture script*. KIT, 2020.
- [32] Erik Arne Hansen, *Numerical modelling of the mixed lubrication regime in a pin-on-disc tribometer*. Master’s thesis, KIT, 2019.
- [33] C. H. Venner and J. Bos, “Effects of lubricant compressibility on the film thickness in ehl line and circular contacts,” *Wear*, vol. 173, no. 1-2, pp. 151–165, 1994.
- [34] D. Dowson and G. R. Higginson, *Elasto-hydrodynamic Lubrication, The Fundamentals of Roller and Gear Lubrication*. Oxford, UK: Pergamon Press, 1966.

-
- [35] C. Roelands, *Correlational aspects of the viscosity-temperature-pressure relationship of lubricating oils*. Doctoral thesis, 1966.
- [36] J. H. Ferziger, M. Perić, and R. L. Street, *Computational Methods for Fluid Dynamics*. Cham: Springer International Publishing, 2020.
- [37] Y.-J. Cho, Y.-P. Koo, and T.-W. Kim, “A new fft technique for the analysis of contact pressure and subsurface stress in a semi-infinite solid,” *KSME International Journal*, vol. 14, no. 3, pp. 331–337, 2000.
- [38] G. B. Thomas, *Thomas’ calculus*. Harlow: Addison-Wesley, 12th ed., united states ed. ed., 2009.
- [39] Robert W. Hornbeck, *Numerical Methods*. Quantum Publishers, INC, 1975.
- [40] J. E. Bringas, *Handbook of comparative world steel standards*. West Conshohocken PA: ASTM International, 5th edition ed., 2016.
- [41] J. Ståhl and B. O. Jacobson, “Compressibility of lubricants at high pressures,” *Tribology Transactions*, vol. 46, no. 4, pp. 592–599, 2003.

Appendix

A. Detailed Flowcharts of the Algorithm

This section in the Appendix provides detailed flowcharts explaining the processes followed in the script. Some processes are simplified as black boxes and shown with a filled black rectangle with white text. The processes shown with a thicker outline mean that the process is detailed in another following flowchart. Naturally, some simplifications have been done to have understandable visualizations of the involved processes. The MATLAB script developed by Erik Hansen and then extended by the author (Altay Kacan) contains extensive comments that detail the working principles of the algorithms. These flowcharts are intended to be supporting material for the MATLAB script and are meant to help visualize how the various algorithms are interconnected. The interested reader is therefore referred to the code for more information.

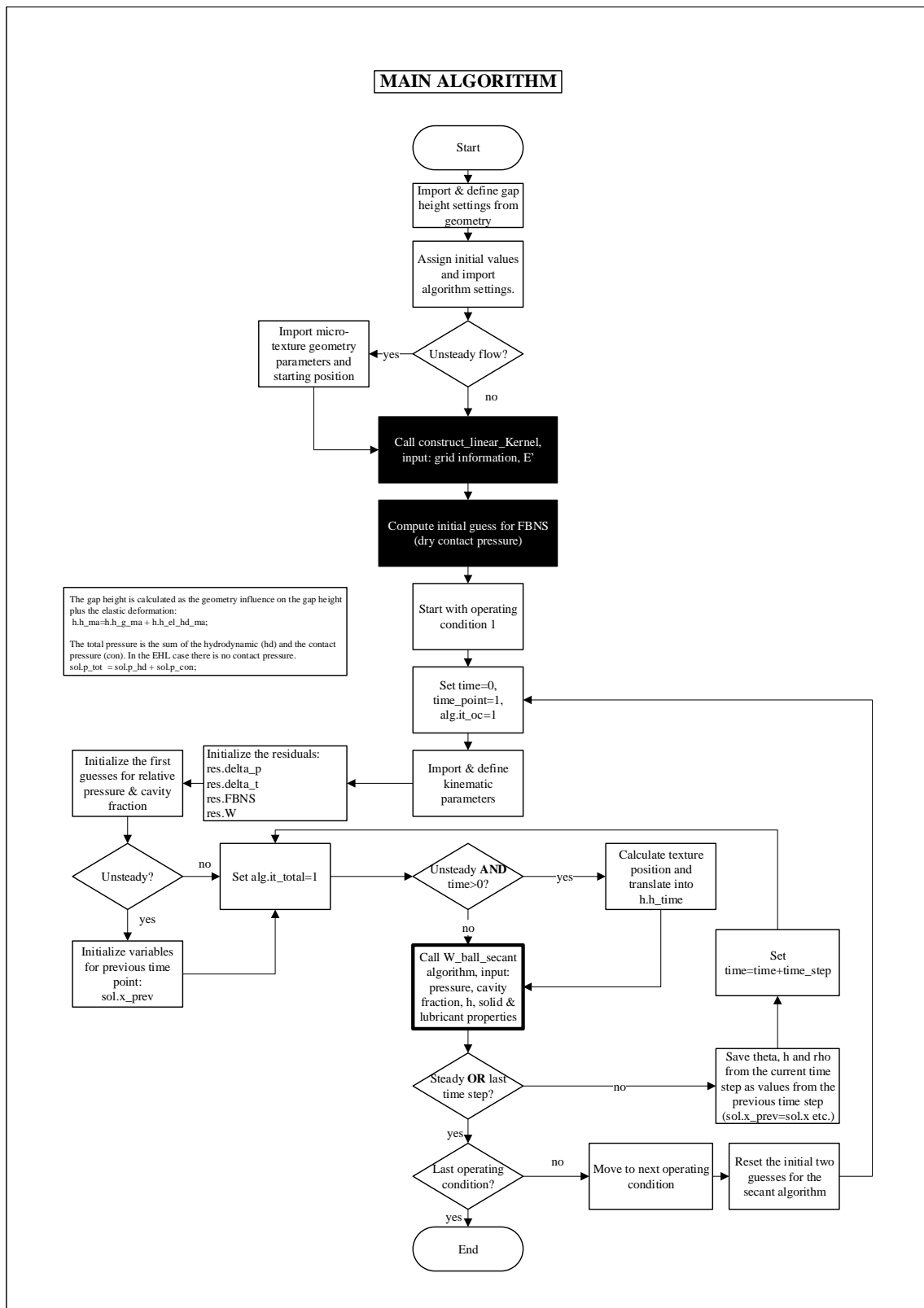


Figure A.1.: Detailed flowchart of the main algorithm.

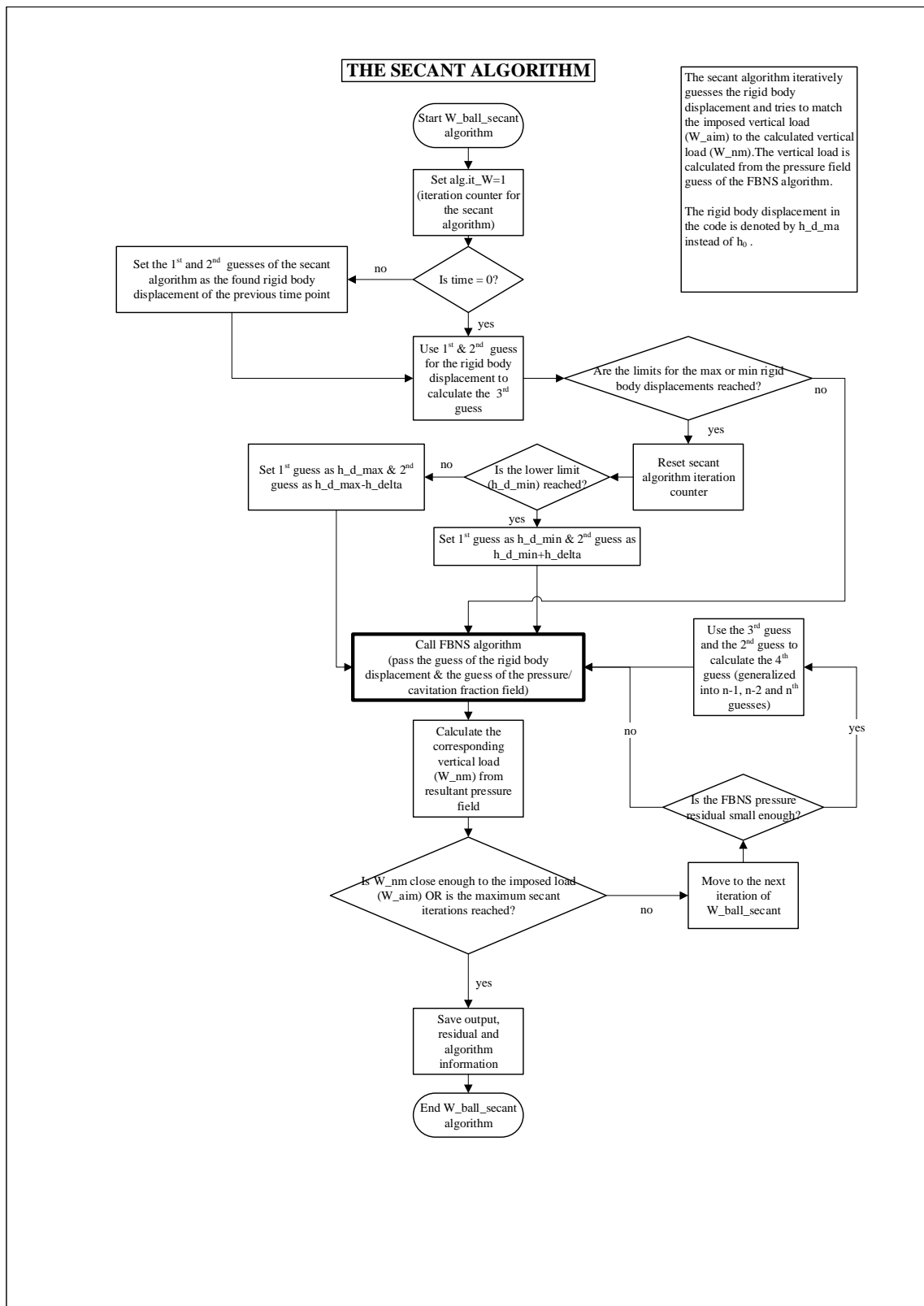


Figure A.2.: Detailed flowchart of the secant algorithm.

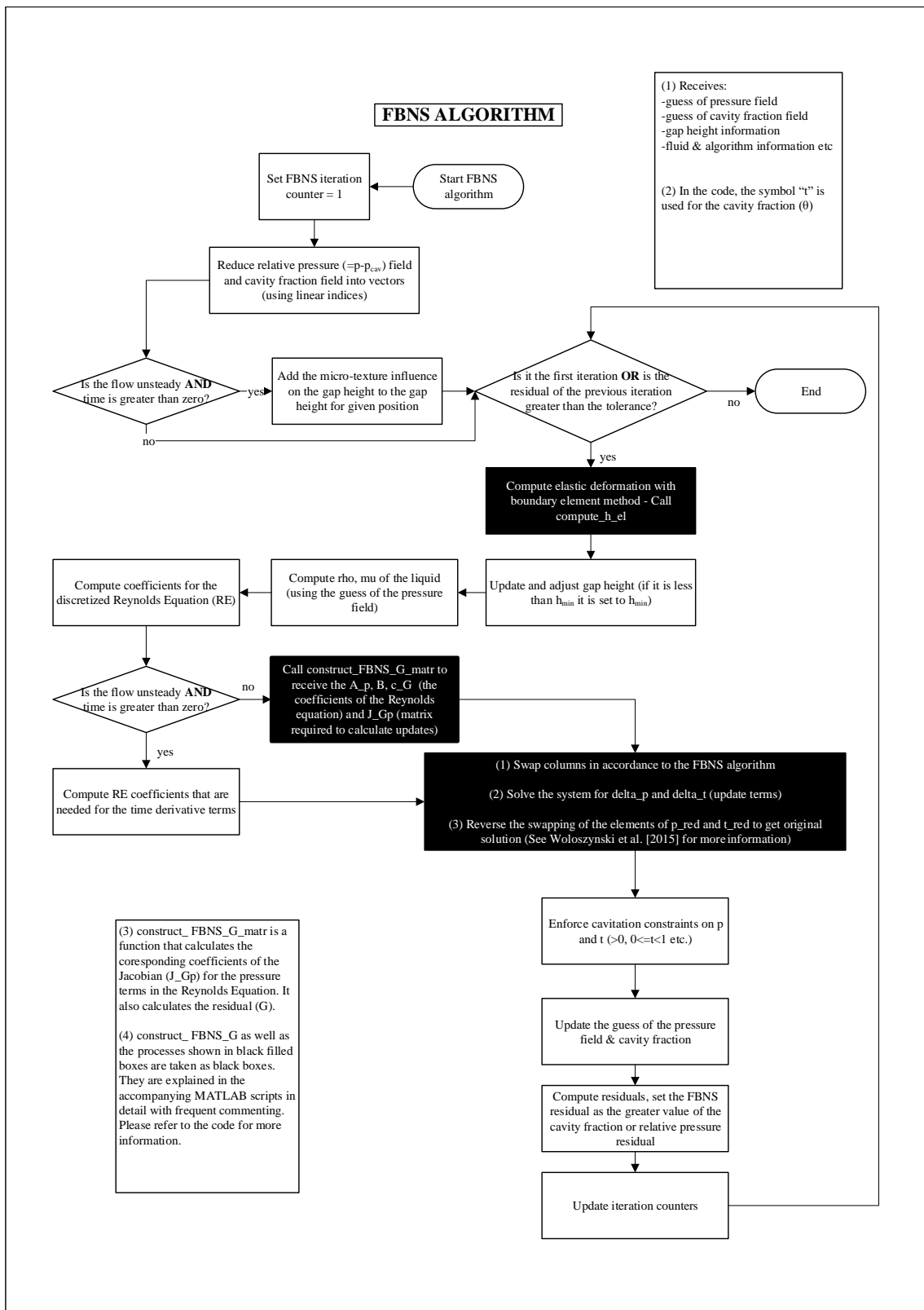


Figure A.3.: Detailed flowchart of the FBNS algorithm.